

THE INFLUENCE OF ANISOTROPIC SLIP AND SHEAR TRANSFORMATION ON  
HETEROGENEOUS DEFORMATION BASED UPON NANOINDENTATION, CRYSTAL  
PLASTICITY MODELING, AND ARTIFICIAL NEURAL NETWORKS

By

Zhuowen Zhao

A DISSERTATION

Submitted to  
Michigan State University  
in partial fulfillment of the requirements  
for the degree of

Materials Science and Engineering – Doctor of Philosophy

2021

## ABSTRACT

### THE INFLUENCE OF ANISOTROPIC SLIP AND SHEAR TRANSFORMATION ON HETEROGENEOUS DEFORMATION BASED UPON NANOINDENTATION, CRYSTAL PLASTICITY MODELING, AND ARTIFICIAL NEURAL NETWORKS

By

Zhuowen Zhao

Most technological relevant structural materials are polycrystals that contain many (millions) so-called grains. Plastic deformation in polycrystalline metallic materials is not homogeneous at the microscale, but sometimes strongly heterogeneous among grains and varies spatially within an individual grain. The ability to predict the magnitude and spatial distribution of plastic inhomogeneity, particularly near grain boundaries (GBs), is crucial as it often results in a stress concentration that could lead to nucleation of damage sites, which largely affect the lifetime of stressed components. Accurate modeling of such inhomogeneity depends on the reliable description of *basic* plastic micro-mechanisms, *e. g.*, dislocation slip, and *fine* details such as interactions between slip and GBs. This study aims to facilitate the above need by 1) establishing consistent critical resolved shear stress (CRSS) values that form the basis of a phenomenological description of plasticity, 2) enhancing effective metric selection for slip transfer across GBs, and 3) improving the understanding of the kinematics of the phase transformation—an important thermo-mechanical treatment that strongly influences the microstructure for many hexagonal engineering alloys such as Ti and Zr alloys.

The first part of the present work is to quantify the uncertainty of *initial* CRSS values determined from Inverse indentation analysis (IIA). This approach optimizes the adjustable parameters in a chosen constitutive description of crystal plasticity until the load–depth response and the residual surface topography match between real and simulated nanoindentation(s) into a particular grain. IIA was evaluated for hexagonal pure Ti (CP-Ti) and two Ti alloys (Ti-3Al-2.5V and Ti-6Al-4V) at different temperatures (ambient and 523 K) and is found to produce consistent CRSS values when the combined relative error is no more than 20 %.

A novel approach to evaluate the effectiveness of slip transfer metrics (individually) and their

combinations using a double-layer artificial neural network (ANN) is presented as the second part of the thesis. The considered metrics include the misorientation angle between two grains,  $m'_{\alpha\beta}$ ,  $SF_{\alpha} + SF_{\beta}$ ,  $\Delta b_{\alpha\beta}$ , and some of their compounds. The accuracy of binary (slip transfer or not) classification reaches around 90 % based on data collected from pure Al oligocrystals deformed in tension, and it is around 80 % for tensile deformed polycrystalline Ti-5Al-2.5Sn samples. This approach extends the one- or two-dimensional projections formerly applied to analyze slip transfer and can be implemented into crystal plasticity model as an “intelligent” decision-maker for each individual slip–boundary interaction.

Lastly, a method to calculate orientation and deformation gradient variants resulting from phase transformation between hexagonal  $\alpha$  and body-centered cubic  $\beta$  phase is proposed based on a series of frame rotations and transformations. Furthermore, a cluster-based approach is presented to automate point-wise reconstruction of  $\beta$  orientations from  $\alpha$  orientations in a large indexed area. This work will assist in analyzing research problems that often require historical information of the current microstructures, for instance, understanding variant selections during the  $\alpha \rightarrow \beta \rightarrow \alpha$  transformation. The proposed method will also facilitate the implementation of such transformation kinematics into continuum-based models as the deformation gradient that influences the transformation can be conveniently computed.

Copyright by  
ZHUOWEN ZHAO  
2021

## ACKNOWLEDGMENTS

I want to extend my deepest gratitude to my advisor, Dr. Philip Eisenlohr, for his guidance and continuous support for my PhD studies. Not only have I learned an enormous amount of knowledge and technical skill from him, but also how to do critical thinking and scientific research. He gave a lot of patience and space for me to grow as a young scientist. I am grateful that he always encouraged me to explore my own interests and career path and supported my decisions to take additional graduate courses in the last year of the PhD program.

I would also like to thank Dr. Thomas R. Bieler for his joint supervision on my projects and his mentorship on being a good graduate student. I also appreciate his friendship and hospitality at the annual Thanksgiving gatherings in his house and his assistance during my travels to Spain to perform high-temperature nanoindentation experiments.

Next, I would like to thank my committee members, Dr. Martin A. Crimp and Dr. Thomas J. Pence, for asking good questions and giving comments on the thesis. I also enjoyed auditing Dr. Crimp's TEM course and sitting in Dr. Pence's plasticity classes.

My sincere gratitude also goes out to my collaborators, Dr. Javier Llorca, Dr. Jon Molina-Aldareguía, Dr. Miguel Monclús, Mario Rueda Ruiz from IMDEA Materials Institute, Dr. Dipankar Banerjee from Indian Institute of Science, and Dr. Shanoob Balachandran and Jiawei Lu from Michigan State University.

Moreover, I would like to thank Dr. Carl J. Boehlert for his kindness in letting students from the metal group use his lab and providing me with accommodation during my first Spain travel. I will also be forever thankful for my colleagues from the metal group and people I met at Michigan State University and the local communities. They have offered me welcome, friendships, and good memories.

Last but not least, I would like to give special thanks to my dearest parents and brother for their everlasting unconditional love, support, and trust in me. They are my inspiration and the greatest power in this journey and new adventures to come!

## TABLE OF CONTENTS

LIST OF TABLES . . . . .	viii
LIST OF FIGURES . . . . .	ix
KEY TO ABBREVIATIONS . . . . .	xiii
CHAPTER 1 INTRODUCTION . . . . .	1
CHAPTER 2 PLASTIC DEFORMATION IN POLYCRYSTALLINE METALS . . . . .	5
2.1 Dislocation slip in face-centered cubic and hexagonal crystals . . . . .	5
2.2 Composition and temperature influence on dislocation slip activity . . . . .	8
2.3 Slip transfer in polycrystals . . . . .	9
2.4 Phase transformation between hexagonal and body-centered cubic crystals . . . . .	12
CHAPTER 3 RESEARCH BACKGROUND . . . . .	14
3.1 Disparate critical resolved shear stress (CRSS) values by different methods . . . . .	14
3.2 Establishing slip transfer parameters for crystal plasticity models . . . . .	17
3.2.1 Modeling plastic deformation in polycrystals . . . . .	17
3.2.2 Prior work on establishing effective slip transfer metrics . . . . .	20
3.3 Variant selections in transformation between hexagonal $\alpha$ and body-centered cubic $\beta$ phase . . . . .	27
CHAPTER 4 METHODOLOGY . . . . .	30
4.1 Inverse indentation analysis (IIA) . . . . .	30
4.1.1 Nanoindentation . . . . .	31
4.1.2 Crystal plasticity finite element simulation . . . . .	33
4.1.3 Non-convex optimization . . . . .	36
4.1.4 Surface topography upscaling . . . . .	39
4.1.5 Comparison between simulation and experiment . . . . .	40
4.1.6 Single orientation approach . . . . .	40
4.1.7 Relationship between the total indentation mismatch and CRSS uncertainty . . . . .	43
4.2 Evaluation of slip transfer metrics with artificial neural network (ANN) . . . . .	45
4.3 Transformation between hexagonal $\alpha$ and body-centered cubic $\beta$ crystals . . . . .	49
4.3.1 Orientation calculation . . . . .	50
4.3.2 Deformation gradient calculation . . . . .	51
4.3.3 Variants in hcp–bcc ( $\alpha$ – $\beta$ ) phase transformation . . . . .	52
CHAPTER 5 QUANTIFYING UNCERTAINTIES OF CRSS VALUES OF HEXAGONAL TI ALLOYS DERIVED FROM NANO-INDENTATION . . . . .	58
5.1 Introduction and motivation . . . . .	58
5.2 Materials and Methods . . . . .	58
5.3 Indentation measurements . . . . .	59

5.4	Simulation and optimization set-ups . . . . .	62
5.5	Quantification of errors . . . . .	65
5.6	CRSS values identified by inverse indentation analysis . . . . .	69
5.7	Summary . . . . .	72
CHAPTER 6 GRAIN BOUNDARY SLIP TRANSFER CLASSIFICATION AND MET- RIC SELECTION . . . . .		73
6.1	Introduction and motivation . . . . .	73
6.2	Slip transfer dataset . . . . .	74
6.2.1	Al oligocrystals dataset . . . . .	74
6.2.2	Polycrystalline Ti-5Al-2.5Sn dataset . . . . .	76
6.3	Double-layer ANN architecture . . . . .	76
6.4	Classifying slip transfer in Al oligocrystals . . . . .	78
6.4.1	Results . . . . .	78
6.4.2	Discussion . . . . .	81
6.4.3	Summary . . . . .	82
6.5	Classifying slip transfer in polycrystalline Ti-5Al-2.5Sn . . . . .	84
6.5.1	Results & discussion . . . . .	84
6.5.2	Summary . . . . .	86
CHAPTER 7 AUTOMATED BODY-CENTERED CUBIC $\beta$ RECONSTRUCTION . . . . .		87
7.1	Introduction and motivation . . . . .	87
7.2	The unique determination rule . . . . .	89
7.3	Automated bcc reconstruction . . . . .	90
7.3.1	Determining the parent bcc orientation by a cluster-averaging algorithm . . . . .	91
7.3.2	Validation of bcc reconstruction based on synthetic data . . . . .	93
7.3.3	Validation of bcc reconstruction based on measured data . . . . .	94
7.4	Summary . . . . .	95
CHAPTER 8 CONCLUSIONS AND FUTURE WORK . . . . .		96
8.1	Conclusions . . . . .	96
8.2	Future work . . . . .	97
APPENDIX . . . . .		98
BIBLIOGRAPHY . . . . .		102

## LIST OF TABLES

Table 4.1:	Statistics of random distribution of variants (1152 explorations in total) from a common initial hcp lattice in the hcp-bcc-hcp transformation. . . . .	52
Table 4.2:	: List of 57 possible variants in hcp-bcc-hcp phase transformation. $b_i$ is the bcc symmetry operator in Table .2, and $h_i$ is the hexagonal symmetry operator in Table .1. “+” and “-” denote clockwise and counterclockwise rotation, respectively. The cubes in the rightmost column show the transformed cubic volume (the original shape is the same as the first cube). . . . .	53
Table 4.3:	Misorientation angle between two $\beta$ variants from the same parent alpha grain. . . . .	57
Table 5.1:	Constitutive parameters of the phenomenological power-law (see [106] for details) used in the indentation simulations as adopted from [136]. Sole values in a row reflect published data of CP-Ti but are used for all three materials, as differences are assumed to be trivial. . . . .	64
Table 6.1:	$F$ -scores of metric value distributions shown in Fig. 6.1. . . . .	81
Table .1:	List of 12 hexagonal lattice symmetry operators used in the thesis ( $a = \frac{\sqrt{3}}{2}$ ) . . .	100
Table .2:	List of 24 cubic lattice symmetry operators used in the thesis. . . . .	101



## LIST OF FIGURES

Figure 1.1: Hierarchical modeling (source: Dr. Dierk Raabe) . . . . .	1
Figure 2.1: Schematic illustrations [58] of (a) shear resolved along the slip direction on the slip plane under a longitudinal loading $F$ , and (b) plastic deformation by edge (top row) and screw (bottom row) dislocation slip under the stress pointed by the arrows. . . . .	5
Figure 2.2: Slip system types in hexagonal crystal structure. . . . .	7
Figure 2.3: Temperature dependence of CRSS values of basal, prism, and pyramidal $\langle c + a \rangle$ in single crystals of Ti-6.6Al [83]. . . . .	8
Figure 2.4: Dislocation interactions with grain boundaries [6]. . . . .	10
Figure 2.5: Schematic illustration of the crystallographic relationship between $\alpha$ plates and $\beta$ stripes in $\alpha$ colonies (eventually will result in a <i>typical</i> “basket weave” microstructure) [83]. . . . .	13
Figure 3.1: Disparate CRSS values of CP-Ti reported in the literature [21]. . . . .	17
Figure 3.2: Geometrical relationship between slip in the incoming grain (blue) and receiving grain (orange) transmitting across the grain boundary. $\kappa$ is the angle between incoming and outgoing slip directions, $\psi$ is the angle between plane norms, and $\theta$ is the angle between the plane traces on the boundary [52]. . . . .	20
Figure 3.3: Continuity and discontinuity of slip transfer surface traces [6]. . . . .	21
Figure 3.4: Some slip transfer and blocking cases in tensioned oligo pure Al sample [9]. . . . .	22
Figure 3.5: Separating slip transfer and no transfer cases by line drawing in 2D plotting [2]. . . . .	26
Figure 4.1: Schematic of establishing constitutive parameters from inverse indentation optimization. . . . .	31
Figure 4.2: Leftmost: nanoTest Alpha, Micro Materials Ltd. Right two: SEM images of the diamond indenter tip with 1 $\mu\text{m}$ radius and 90° cone angle before and after 90° rotation. . . . .	32
Figure 4.3: Orientation informed nanoindentation in polycrystalline CP-Ti. . . . .	33

Figure 4.4:	Finite element discretization of a cylindrical single crystal with 4 $\mu\text{m}$ radius and 3 $\mu\text{m}$ thickness used in the indentation simulations (only half of the total of 1008 C3D8 elements is shown). Conospherical indenter is modelled as a rigid analytical surface with 90° cone angle. Top-down views after 200 nm (left) and 50 nm (right) deep indentation illustrate examples of resulting simulated surface topography for two distinct crystal orientations. . . . .	34
Figure 4.5:	Top row: Himmelblau’s function has 4 identical local minima shown in contour plots. Bottom row: schematics of finding one of the local minima of Himmelblau’s function (top right one in contour plots, see red square in bottom figures which is the global best solution) using Particle Swarm Optimization in 25 iterations ( $N_{\text{particle}} = 20$ , $N_{\text{iteration}} = 0, 10, 25$ from left to right, bounds are [-10,10] for both dimensions). . . . .	38
Figure 4.6:	Optimal scaling factors (middle) to upscale simulated indentation surface topography in Z displacement and radial direction (left). Relative deviations (errors) between simulated upscaled topography and the (simulated) topography at the target depth (right). . . . .	39
Figure 4.7:	Average sensitivity of CRSS value of basal, prism, and pyramidal $\langle c + a \rangle$ system at different crystallographic orientations [21]. . . . .	41
Figure 4.8:	Reproducibility evaluation of IIA [21] based on two sets of synthetic CRSS values (left column). Right column presents the determined CRSS values using the synthetic indentation responses at 5 sensitive orientations (dark) and 1 insensitive orientation (light) . . . . .	42
Figure 4.9:	Short-range sensitivity (in a cubic parameter domain consists 27 parameter sets, the x, y, and z-axis indicate the CRSS ranges for basal, prism, and pyramidal $\langle c + a \rangle$ respectively) of load-displacement in left column and surface topography in right column for orientation 8 (highlighted in red circle) in the IPF triangle. . . . .	44
Figure 4.10:	Architecture of the artificial neural network used for binary classification (green, red) with $N_{\text{input}}$ nodes in the input layer and $N_{\text{hidden}}$ nodes in each of the two hidden layers. . . . .	45
Figure 4.11:	Left: gradient descent optimization for $L_2$ -norm as loss function. Right: rectified linear unit (ReLU) and hyperbolic tangent (tanh) are two commonly used activation functions in ANN. . . . .	45
Figure 4.12:	Schematics of hcp lattice (Euler angles $\phi_1 = 0^\circ, \Phi = 0^\circ, \phi_2 = 0^\circ$ ) transforming to bcc lattice (one scenario, $\theta = \pm 5.26^\circ$ ). . . . .	49

Figure 5.1:	Surface topographies resulting from indentations at ambient temperature (left) and elevated temperature (right) for the three investigated Ti alloys (rows). Location of each topography on the inverse pole figure indicates the crystallographic indentation direction; in-plane rotation follows the convention of Zambaldi and Raabe [135]. For each material–temperature combination, all indents labeled in black were individually subjected to inverse indentation analysis to establish CRSS values of basal, prismatic, and pyramidal $\langle c + a \rangle$ slip families. . . . .	60
Figure 5.2:	Increase of indenter force with depth up to maximum load (4, 6, or 10 mN) for all crystallographic indentation directions shown in Fig. 5.1. . . . .	61
Figure 5.3:	Exemplary deviations between the measured topographies (top left) and load–depth responses (bottom left) of two nominally identical indentations. Distributions of $\epsilon_{\text{topo}}$ (top right) and $\epsilon_{\text{LD}}$ (bottom right) resulting between indentation experiments with either nominally identical (solid) or closely agreeing (dashed) crystallographic indentation directions for the different (color-coded) material–temperature combinations. . . . .	65
Figure 5.4:	Example of (typically minor) deviations between simulated load–depth responses (bottom left) for two identical indentation directions that only differ by an in-plane rotation (of $7.50^\circ$ ); black curves in rightmost diagrams (top and bottom) show the associated distributions of $\epsilon_{\text{topo}}$ and $\epsilon_{\text{LD}}$ expected from differing FE mesh alignments. Optimal factors to upscale simulated topographies in vertical and radial direction ( $f_z$ and $f_r$ ) closely follow a power-law with respect to the indentation depth ratio (target/simulated depth, top left). Topography deviations due to such upscaling increase systematically with increasing depth ratio (top center) and result in the color-coded $\epsilon_{\text{topo}}$ distributions (top right). Similarly, the scatter in $\epsilon_{\text{LD}}$ ratios increases with decreasing depth fraction (evaluated/experimental target depth, bottom center); each group of ratios observed within one (color-coded) range of indentation depths applicable to that material–temperature combination is used to scale the mesh rotation-induced $\epsilon_{\text{LD}}$ distribution (black, bottom right) to estimate the uncertainty (color-coded, bottom right) associated with simulating only up to a limited indentation depth. Indentation depth fraction in bottom center is arranged in a reversed order to have the same colored bands as indentation depth ratio in top center. . . . .	66
Figure 5.5:	Distributions of expected overall uncertainty (Eq. (4.11)) caused by measurement and simulation limitations for each of the five material–temperature combinations. . . . .	69

Figure 5.6:	CRSS values for basal, prism, and pyramidal $\langle c+a \rangle$ slip identified by inverse indentation analysis based on the crystallographic indentation directions highlighted in Fig. 5.1. Darker shading within each material–temperature combination corresponds to better, <i>i.e.</i> lower, fitness indicated by open circles on the right axis. Dashed lines in the bottom left show the outcomes of three independent optimization runs for the same indentation. Vertical lines represent the range of expected uncertainty as shown in Fig. 5.5. . . . . .	70
Figure 6.1:	Distributions of metric values classified as either definite, likely, or no slip transfer (green, gray, red) based upon oligo Al data. The underlying population of near-cube texture, rotated-cube texture, and their union are indicated by light, intermediate, and dark color shade, respectively. . . . .	75
Figure 6.2:	Distributions of metric values classified as either definite (green) or no slip transfer (red) based on Ti-5Al-2.5Sn data (tensile deformed at 728 K). . . . .	77
Figure 6.3:	Classification accuracy as function of hidden layer node count $N_{\text{hidden}}$ for different $N_{\text{input}}$ of compounded slip transfer metrics with $N_{\text{training}} = 97$ . Both rows present the <i>same</i> data but use different ratios (and different scales) to measure accuracy. Color shading reflects relatively better accuracy from light to dark. Orange and brownish shading indicates that $SF_{\alpha} + SF_{\beta}$ are included in the input metric(s). The right-most column varies $N_{\text{training}}$ (shades of purple) for one case of $N_{\text{input}} = 3$ and contrasts the classification accuracy of testing data (lines) to that of just reclassifying the training data (circles). . . . .	80
Figure 6.4:	Average slip transfer classification accuracy of Ti-5Al-2.5Sn with double hidden layer ANN ( $N_{\text{hidden}} = 20$ ) based on different combinations of metrics. . . . .	84
Figure 7.1:	The “parent” beta orientation is uniquely determined when $N_{\text{combo}} \geq 4$ . . . . .	89
Figure 7.2:	Schematic of reconstructing “parent” beta grains by a window searching algorithm. . . . .	90
Figure 7.3:	The first step: dynamically adding $\beta$ orientations to the cluster by checking each $\beta$ orientation of the “seed” against the $\beta$ orientation of the other $\alpha$ orientations (columns). . . . .	91
Figure 7.4:	The second step excludes the members violating the unique determination rule. . . . .	92
Figure 7.5:	The third step finds the longest shared $\beta$ cluster (mageta). . . . .	93
Figure 7.6:	Correct $\beta$ reconstruction results based upon synthetic data. . . . .	93
Figure 7.7:	$\beta$ reconstruction (200 x 200) of lamella $\alpha$ phase in Ti-6Al-2Sn-4Zr-6Mo using window size of 71 ( $\alpha$ data provided by [3]). . . . .	94

## KEY TO ABBREVIATIONS

**ANN** Artificial neural network

**bcc** body-centered cubic

**BOR** Burgers orientation relationship

**CPFEM** Crystal plasticity finite element method

**CRSS** Critical resolved shear stress

**DD** Dislocation dynamics

**DIC** Digital image correlation

**ECCI** Electron channeling contrast imaging

**EVP** Elasto-viscoplastic

**EBSD** Electron backscatter diffraction

**ff-HEDM** Far field high energy X-ray diffraction microscopy

**FIB** Focused ion beam

**GB** Grain boundary

**GND** Geometrically necessary dislocation

**hcp** hexagonal close-packed

**HR-EBSD** high-resolution electron backscattering diffraction

**IIA** Inverse indentation analysis

**IIT** Instrumented indentation testing

**IPF** Inverse pole figure

**N-M** Nelder–Mead

**PSO** Particle swarm optimization

**ReLU** Rectified linear unit

**SEM** Scanning electron microscope

**SMMA** Summation of mutual misorientation angle

**TEM** Transmission electron microscope

**VPSC** Viscoplastic self-consistent

# CHAPTER 1

## INTRODUCTION

During plastic deformation, shear stresses are accommodated by activation and evolution of micro-mechanisms such as dislocation slip and twinning, leading to permanent shape change and eventually failure (when shear stresses are no longer accommodated). For polycrystalline materials that are usually used in engineering applications, plastic deformation is inhomogeneous among different grains and varies within each individual grain. This inhomogeneity often contributes to the formation of a stress concentration that could ultimately break material compatibility<sup>1</sup> and facilitate the nucleation of critical damage sites or crack. Hence, accurate modeling of inhomogeneous deformation is the first step to predicting failure behavior.

For engineering parts or components, models taking into account the mechanisms/physics and/or microstructures at mesoscale (see Fig. 1.1), such as dislocation dynamics (DD) and continuum-based models, are more meaningful (for predicting the macroscopic aggregate properties, *e.g.*, service performance) than very fine scale models, *e.g.*, ab initio methods. DD simulates the in-

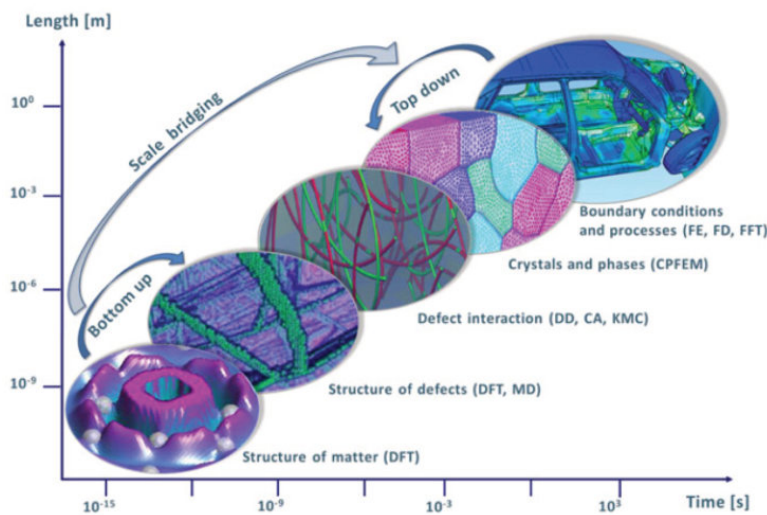


Figure 1.1: Hierarchical modeling (source: Dr. Dierk Raabe)

<sup>1</sup>Arbitrary shape change that requires a minimum of five independent deformation modes according to von Mises [122].

teractions and propagation of dislocation slip, which is the most important plasticity carrier in metallic materials at ambient temperature. However, DD still considers a relatively small volume compared to continuum models. Two types of continuum models, *i.e.*, yield surface models and crystal plasticity finite element models, have been used in the past decades [4, 8, 12, 16, 54, 57, 60, 66, 69, 92, 103] to simulate plastic deformation in polycrystals where the challenges mainly lie in how to homogenize the anisotropic responses from individual grains to get the aggregate responses. The early attempts used yield surface models based on rigid boundary constraints, *i.e.*, the Taylor–Bishop–Hill full constraints [12], assuming all grains deform in the same way. Later on, a less strict strategy that treats each grain as if it was embedded in a homogeneous matrix was adopted to enable capturing the anisotropic responses of each individual grain. Lebensohn and Tomé [69] first adopted this homogenization scheme into a crystal plasticity model based on a phenomenological description of dislocation slip, known as the viscoplastic self-consistent VPSC model. Other homogenization schemes and crystal plasticity models have been developed [4, 8, 87, 89, 103]. In the past decade, it was realized that capturing the plastic heterogeneity within the grain near the grain boundaries (GB) is crucial to predicting damage nucleation. Therefore, there is an increasing demand in modeling a finer scale plastic inhomogeneity in the community.

One important aspect of modeling heterogeneous deformation is establishing critical resolved shear stress (CRSS) values for individual slip systems as they describe the evolution of slip resistance to being activated in a phenomenological description of plasticity. Experimental quantification of individual CRSS values (for less active slip systems) by exclusive activation is challenging because the easiest slip mode usually carries plastic flow. A popular approach to determine CRSS ratios is through statistical analysis of surface traces. It relates the frequency of surface slip trace observations to their theoretical propensity [74]. However, this approach does not include slip activity beneath the surface, which could give rise to considerable estimation uncertainty [21]. An approach to overcome this downside is to find the best match between nanoindentation responses (surface topography/elevation and load–depth curves) and their simulation counterparts such that the optimal CRSS values are obtained through an iterative fitting, which is known as inverse in-



dentation analysis (IIA). In a reliability assessment based on synthetic data, Chakraborty et al. [21] found that IIA has better accuracy and precision than the statistical surface trace analysis. However, what is still missing is the evaluation of IIA against measured data because *real-world* data often have noise that cannot be ignored. With such motivation, Chapter 5 quantifies the error sources associate with IIA based on measured data of CP-Ti, Ti-3Al-2.5V, and Ti-5Al-2.5Sn at two temperatures.

Another critical aspect of modeling heterogeneous deformation is understanding the role of GBs and incorporating such fine-detailed physics into the existing models to improve the prediction performance. Efforts have been made to establish metrics for slip transfer events where dislocation shear is transferred to the receiving grain across a permeable boundary. These metrics include criteria that consider the geometrical alignment of incoming  $\alpha$  and outgoing  $\beta$  systems such as Luster-Morris  $m'_{\alpha\beta}$ ; those reflecting local stress preference, *e.g.*, Schmid factor sum  $SF_{\alpha} + SF_{\beta}$ ; and the residual Burgers vector  $\mathbf{b}_r = \mathbf{b}_{\beta} - \mathbf{b}_{\alpha}$  that needs to be accommodated by GB to maintain its continuity. In the existing analyses, data is plotted with respect to a single or two metrics, and the classification of slip transfer (or no transfer) is made through observations. This approach cannot efficiently examine combinations of more than two metrics. To address this limitation, in the second part of the present work (Chapter 6), an exhaustive evaluation of the effectiveness of these metrics (individually) and their combinations using a double-layer artificial neural network (ANN) is presented.

Other microstructure details and deformation mechanisms can also influence the development of microstructure that affects the evolution of heterogeneous deformation. For example, phase transformation kinematics affect the statistics of misorientations that influence slip transfer and the resulting properties. In the last part of the present work, the thesis focuses on a particular phase transformation between hexagonal  $\alpha$  and body-centered cubic  $\beta$  crystals as it is an essential thermo-mechanical treatment for many Ti and Zr alloys.<sup>2</sup> A major contribution regarding this part of the work is a consistent method (Chapter 4, Section 4.3.2) to calculate the deformation

---

<sup>2</sup>The desired microstructures can be obtained by controlling the process parameters (temperature, cooling rate, time length above the  $\beta$  transus *etc.*).

gradient that describes the transformation kinematics, enabling the implementation of such transformation in continuum models. Furthermore, many research problems regarding hex–bcc phase transformation, such as understanding the variant selection phenomena and slip transfer across the boundary between  $\alpha$  grains with a different history, require historical information of  $\alpha$  microstructures (low temperature). Hence, an approach to efficiently reconstruct  $\beta$  orientations is desired in the community. Therefore, another major contribution is an automated approach to do point-wise  $\beta$  reconstruction with a good balance of efficiency and accuracy, presented in Chapter 7.

To help navigate through the thesis, an outline is given below.

- Chapter 2 gives a basic introduction to the plastic micro-mechanisms that are covered in this thesis.
- Chapter 3 reviews the challenges that motivate the three works (respectively) presented in this thesis.
- Chapter 4 demonstrates the details of the approaches used in the present work.
- Chapter 5 presents the first project on error quantification and establishing uncertainty of CRSS values determined by inverse indentation analysis.
- Chapter 6 demonstrates the second project that evaluates the effectiveness of individual slip transfer metric and their combinations with artificial neural networks.
- Chapter 7 introduces the third project that proposes an approach to automate point-wise  $\beta$  reconstruction.
- Chapter 8 concludes the three projects and the future works.

## CHAPTER 2

### PLASTIC DEFORMATION IN POLYCRYSTALLINE METALS

In this chapter, a most common plastic deformation mechanism, *i.e.*, dislocation slip, is briefly reviewed for face-centered cubic (fcc) and hexagonal crystals, followed by an introduction to composition and temperature effect on dislocation slip activity, particularly for the hexagonal lattice. Then interactions between dislocation slip and interfaces (especially grain boundaries) are presented. Finally, the last section introduces a typical phase transformation that many hexagonal engineering alloys undergo during thermo-mechanical treatments.

#### 2.1 Dislocation slip in face-centered cubic and hexagonal crystals

When plastically deforming a material, shear stresses are accommodated by activation and evolution of micro-mechanism(s), eventually resulting in permanent shape change before fracture.

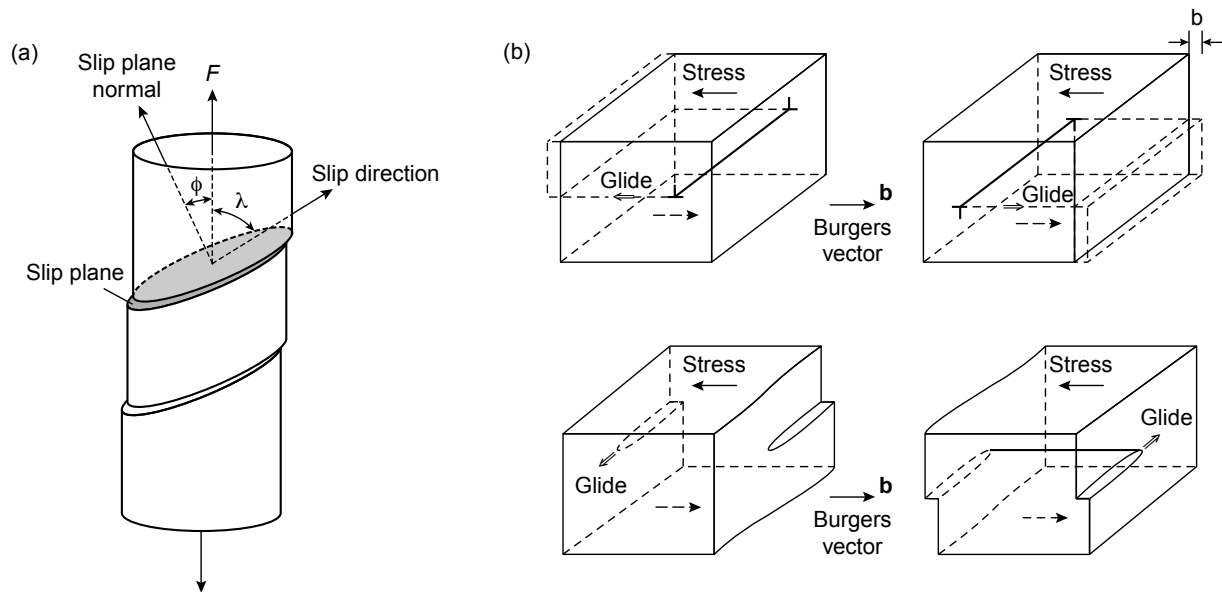


Figure 2.1: Schematic illustrations [58] of (a) shear resolved along the slip direction on the slip plane under a longitudinal loading  $F$ , and (b) plastic deformation by edge (top row) and screw (bottom row) dislocation slip under the stress pointed by the arrows.

The most common mechanism in metallic materials is dislocation motion. Dislocations are line defects due to atom displacement. They can glide inside the material as major carriers of plastic flow at ambient temperature.<sup>1</sup> Dislocation glide, or dislocation slip, is defined by the slip plane normal  $\mathbf{n}$  and the slip direction  $\mathbf{t}$ . The slip plane is usually the close-packed plane where the atom density is the highest, and slip direction is the direction on the slip plane that has the shortest lattice translation vector (highest atom density along a direction) A unique combination of the above two vectors identifies a slip system. The atom displacement caused by one full dislocation slip is called Burgers vector  $\mathbf{b}$ ,<sup>2</sup> as is shown in Fig. 2.1b.

The stress ( $\tau$ ) resolved in the dislocation slip direction on the slip plane can be calculated in Eq. (2.1), which is illustrated in Fig. 2.1a.

$$\tau = \frac{F}{A} \cos \phi \cos \lambda \quad (2.1)$$

Schmid factor  $m = \cos \phi \cos \lambda$  is used to map the global stress to individual slip systems. The threshold value, *i. e.*, critical resolved shear stress (CRSS) or slip resistance, is defined as the minimum shear stress required to activate an individual slip system.

**Dislocation slip in face-centered cubic crystals** Many common metals, such as aluminum, copper, and  $\gamma$ -Fe, have face-centered cubic (fcc) crystal structures. As is introduced above, dislocations tend to glide on the highest density plane and direction. In fcc crystal, the most-packed planes are  $\{111\}$  planes, and there are four of them. Each plane has three<sup>3</sup>  $\frac{1}{2}\langle 110 \rangle$  directions that are the shortest lattice vectors. Thus, there are 12 slip systems in fcc crystal structure. In reality, atoms on  $\{111\}$  planes are energetically favored to glide as two partial dislocations  $\mathbf{b}_2$ ,  $\mathbf{b}_3$  (both have the form  $\frac{1}{6}\langle 112 \rangle$ ) to accomplish one full Burgers vector  $\mathbf{b}_1$  due to the way atoms stack on this plane.

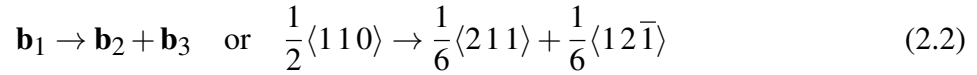
---

<sup>1</sup>At low temperatures where diffusion is difficult, and in the absence of a non-equilibrium concentration of point defects, the movement of dislocations is restricted almost entirely to glide. Non-conservative dislocation motions, *i. e.*, (edge) dislocation climb, become more prevalent as temperature increases.

<sup>2</sup>As a more accurate definition, Burgers vector is the vector required to complete the Burgers circuit.

<sup>3</sup>Positive and negative directions for the same vector are usually not specifically distinguished.

These dissociations are demonstrated in reaction,



**Dislocation slip in hexagonal crystals** Many engineering structural metals and their alloys, such as Ti, Zr, Mg alloys, have hexagonal crystal structures (with varying  $c/a$  ratios). In the close-packed hexagonal structure (with  $c/a$  ratio = 1.633), the  $\{0001\}$  basal plane is the closed-packed plane and the  $\frac{1}{3}\langle 11\bar{2}0 \rangle$   $a$ -direction is the shortest lattice vector (basal slip on  $\{0001\}$   $\langle 1\bar{2}10 \rangle$ ). However, since most hexagonal alloys have  $c/a$  ratios that deviate from the ideal value, other three types of slip systems, *i.e.*, prism slip on  $\{10\bar{1}0\}$   $\langle 1\bar{2}10 \rangle$ , pyramidal  $\langle a \rangle$  slip on  $\{10\bar{1}1\}$   $\langle 1\bar{2}10 \rangle$ , and pyramidal  $\langle c+a \rangle$  slip  $\{10\bar{1}1\}$   $\langle 2\bar{1}\bar{1}\bar{3} \rangle$ , are also observed [58] in hexagonal metals. Figure 2.2 demonstrates the four types of slip systems in hexagonal metals.

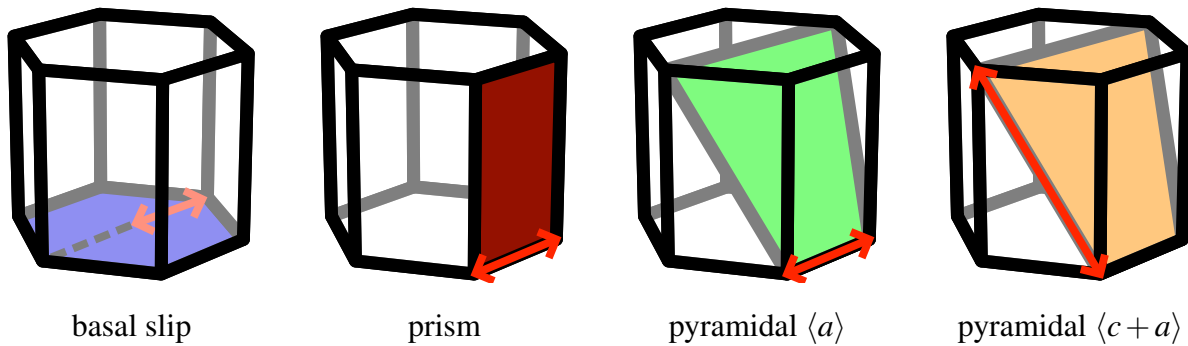


Figure 2.2: Slip system types in hexagonal crystal structure.

Basal, prism, and pyramidal  $\langle c+a \rangle$  are commonly observed whereas pyramidal  $\langle a \rangle$  is less reported in Ti alloys. For CP-Ti, prism slip is generally believed to be the most facile system, and pyramidal  $\langle c+a \rangle$  is the hardest system to be activated at ambient temperature. However, the CRSS ratios among these slip systems vary in the literature, discussed in greater details in Section 3.1. Furthermore, composition and temperature also affect the relative order of these slip systems and are given in Section 2.2.

## 2.2 Composition and temperature influence on dislocation slip activity

**Composition influence on slip activity** Alloying elements can affect slip activity by altering the  $c/a$  ratio. For instance, Li et al. [75] compared tensile deformed CP-Ti and Ti-5Al-2.5Sn and found basal slip activity was significantly enhanced in Ti-5Al-2.5Sn, which can be explained by the increased  $c/a$  ratio in Ti-5Al-2.5Sn. Also, dislocation core structures (energy) can be affected by the alloying elements, *e. g.*, Al may make dislocation cross slip more easily in some alloys [58].

**Temperature influence on slip activity** High temperature enables diffusion and thus, favors dislocation climb. Increasing temperature can accelerate the dislocation motion and may eventually affect the relative order of the easiness to activate individual slip systems. Figure 2.3 shows the slight difference in CRSS values of Ti-6.6Al at room temperature between the basal and prism slip, which becomes even smaller with increasing temperature [83]. A similar trend was observed in a statistical study of CRSS values [74] that the basal slip in CP-Ti becomes more facile when temperature increases from 298 K to 728 K, though it does not win over prism slip in the competition for activation.

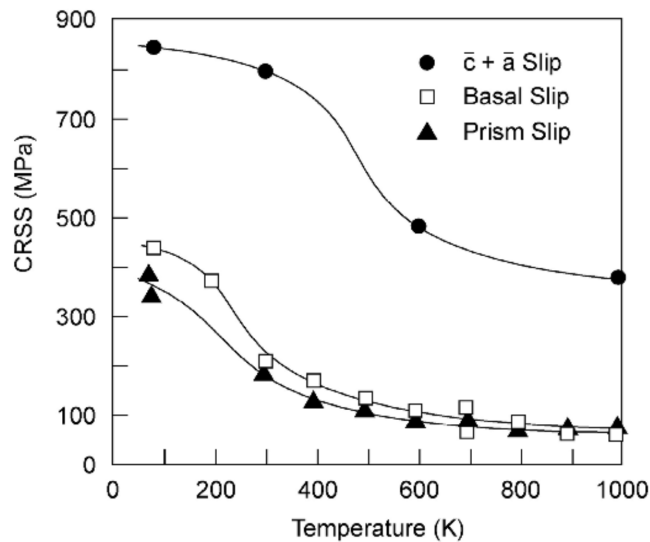


Figure 2.3: Temperature dependence of CRSS values of basal, prism, and pyramidal  $\langle c + a \rangle$  in single crystals of Ti-6.6Al [83].

## 2.3 Slip transfer in polycrystals

**Slip transfer across grain boundaries (GB)** Plastic deformation in polycrystalline aggregates is heterogeneous because it is influenced by the microstructure, *i.e.*, individual grains and their boundaries. At first, the Hall-Petch effect [50, 99] was discovered. It inversely correlates the yield strength of the bulk sample to the grain size, which has been recognized as one of the strengthening mechanisms for metallic materials. An explanation for such mechanism is that grain boundaries (GB) block plastic flow from transferring to other grains, and a smaller average grain size results in higher GB density, thus, leading to macroscopic strengthening of the material. Later, it was realized that there are many types of GB that exhibit varying penetrability to dislocation slip. For example, low angle or low  $\Sigma$  boundaries<sup>4</sup> typically have less energy and are less able to absorb dislocations compared to general boundaries. Studies [120, 121] have shown that low energy boundaries with special polyhedral structure units are particularly favorable for slip penetration. In contrast, one type of triple line where three boundaries intersect, *i.e.*, U line, is usually a high-energy hard boundary that terminates grain boundary dislocation [36]. Two nice reviews on GB characters and their relations to nucleation of damage are given by Bieler et al. [7] and Bayerschen et al. [6].

To summarize, there are three basic scenarios when dislocation slip encounters grain boundaries. 1) Some grain boundaries can serve as an impenetrable barrier that stops dislocations from leaving the parent grain, resulting in the formation of dislocation pileups and stress concentration [34] (see Fig. 2.4a). This leads to the accumulation of geometrically necessary dislocations (GNDs) and lattice curvature to maintain the boundary continuity [8]. 2) Some boundaries can completely absorb dislocations and never emit them again (typically accommodated by screw dislocation cross-slip, see Fig. 2.4c). 3) Other boundaries allow dislocations to be transferred to the receiving grain without leaving residual Burgers vector  $\mathbf{b}_r$  in the boundary (nearly transparent,

---

<sup>4</sup>Coincidence site lattice model demonstrates how well lattice points on the either side of boundary align.  $\Sigma$  is determined by the ratio of area (2-D) or volume (3-D) of the unit cell in coincidence site lattice to that of the unit cell in crystal lattice.  $\Sigma$  is always an odd number and  $\Sigma 1$  means boundary-free perfect crystal.

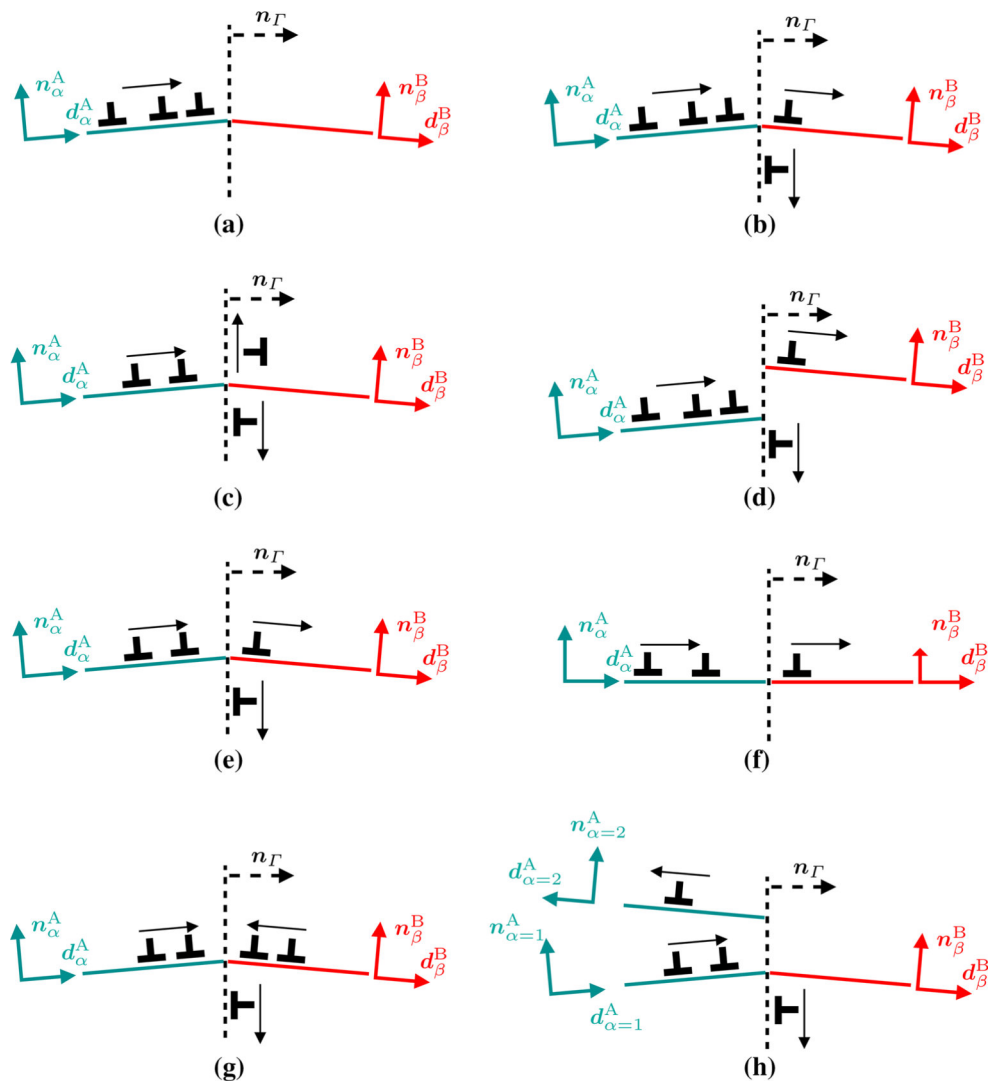


Figure 2.4: Dislocation interactions with grain boundaries [6].



Fig. 2.4f), partially transmitted to adjacent grain, and leaving  $\mathbf{b}_T$  in the boundary (Fig. 2.4b,e), or absorbed by the boundary at first and emitting new dislocation slip in the neighboring grain afterward (Fig. 2.4d). The three situations in category (c) are called slip *transfer* phenomena, while the first two cases (of the three) are also referred to as slip *transmission*. Since the differentiation between slip transfer and transmission in experimental characterizations is usually difficult, the term *slip transfer* is used throughout the thesis to describe all the situations where the evidence of incoming slip transferred to the receiving grain is observed. Moreover, special cases such as two slip systems from adjacent grains are absorbed by the boundary (Fig. 2.4g) and an incoming dislocation is reflected by the boundary (Fig. 2.4h) are also possible [6].

Investigations of conditions that enable the occurrences of slip transfer have been carried out since the 1960s [23, 72, 80, 112]. These factors include geometrical alignment of activated slip systems in either grain, dislocation types, and GB properties (inclination and structure). Among all these considerations, geometrical relationships seem the most dominant [6, 47] to predict slip transfer phenomena correctly. This is intuitive as better alignment would favor slip from either side of the boundary to interconnect. Nevertheless, combining other criteria (*e. g.*, maximizing resolved shear stress on the accommodating plane [6, 72] in the neighboring grain) with geometrical metrics seems to further improve slip transfer predictions, which indicates these additional criteria are also critical. Detailed introduction to the prior work on finding effective criteria for predicting slip transfer across GBs is given in Section 3.2.

**Slip transfer across phase boundaries** Slip transfer occurs not just between grains of the same phase but also between different phases. Although phase boundaries are considered stronger dislocation obstacles compared to GBs [128, 129], evidence of slip transfer across phase boundaries has been reported. For example, in a dual-phase brass alloy that exhibits face-centered (soft) and body-centered (hard) cubic phases, Werner and Prantl [128] discovered dislocation slip were initiated only in the soft phase and transferred to the hard one. Ti alloys are other common dual-phase alloys. Most Ti alloys have a presence of body-centered cubic  $\beta$  phase to some extent in addition

to hexagonal  $\alpha$  phase at ambient temperature. By examining surface slip traces, Seal et al. [110] found incidents of slip transfer at 15  $\alpha/\beta$  boundaries in Ti-5Al-2.5Sn. They also found these incidences correlate more with the high preference for slip activations, *i. e.*, high Schmid factor, than with good geometrical alignment of Burgers vectors in two phases. Moreover, they discovered  $\alpha/\beta$  boundaries between two phases that display Burgers orientation relationship (BOR) do not necessarily favor the occurrence of slip transfer.

## 2.4 Phase transformation between hexagonal and body-centered cubic crystals

For many hexagonal alloys such as Ti and Zr alloys, the transformation of body-centered cubic (bcc)  $\beta$  phase to hexagonal  $\alpha$  phase can happen martensitically or by nucleation and growth process controlled by diffusion. Large amounts of martensite usually occur in pure metals, dilute alloys, and alloys with high martensitic transformation temperatures [83]. Diffusion-based transformation usually takes place at the transitioning temperature or  $\beta$  transus temperature (1155 K for CP-Ti). It often results in a *typical* microstructure called “basket weave” structure or Widmanstätten structure (shown in Fig. 2.5) [83]. Alloying elements, such as Al, B, and Ga that increases the transitioning temperature are called  $\alpha$  stabilizer while others (lower  $\beta$  transus temperature), *e. g.*, Fe, Si, and Se, are referred to as  $\beta$  stabilizers.

During such phase transformation,  $\alpha$  and  $\beta$  phases maintain a particular crystallographic orientation relationship (Eq. (2.3)). This relationship is named the Burgers orientation relationship (BOR) as it was first proposed by Burgers [17] in a study of Zr.

$$\beta\{110\} \parallel \alpha\{0001\} \quad \text{and} \quad \beta\langle 111 \rangle \parallel \alpha\langle 2\bar{1}\bar{1}0 \rangle \quad (2.3)$$

This BOR was later confirmed for Ti [83] as well. According to this relationship, a bcc crystal can transform into twelve hexagonal variants, having different orientations with respect to the same parent  $\beta$  crystal. The BOR is closely obeyed for both the martensite and diffusion-based transformation.

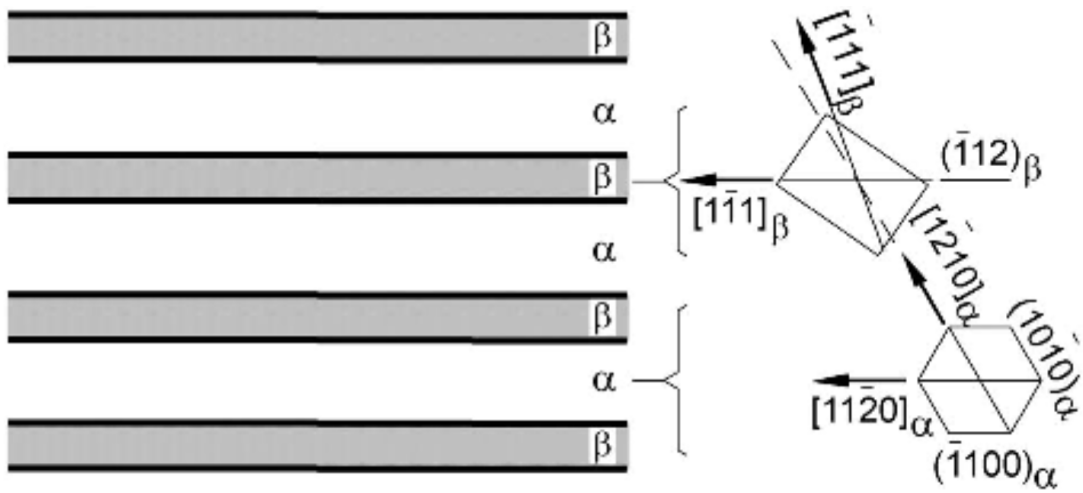


Figure 2.5: Schematic illustration of the crystallographic relationship between  $\alpha$  plates and  $\beta$  stripes in  $\alpha$  colonies (eventually will result in a *typical* “basket weave” microstructure) [83].

## CHAPTER 3

### RESEARCH BACKGROUND

In this chapter, background of the three projects are given in the following order. Section 3.1 introduces the existing common approaches to establish critical resolved shear stress (CRSS) values and primarily discusses the disparity of the reported CRSS values or ratios for hexagonal CP-Ti. Section 3.2 first outlines the mesoscale modelings of heterogeneous plastic deformation in polycrystalline aggregates and the challenges to include finer scale details of slip activity near grain boundaries in Section 3.2.1. Then this section is followed by an introduction to the prior work on establishing reliable slip transfer metrics that are intended to be implemented in crystal plasticity models to facilitate the prediction of heterogeneity near grain boundaries in Section 3.2.2. Section 3.3 talks about the current understanding of variant selections in phase transformation for some hexagonal alloys such as Ti and Zr alloys.

### 3.1 Disparate critical resolved shear stress (CRSS) values by different methods

The reliable determination of adjustable parameters in the constitutive description of crystal plasticity is still an unsettled issue, in particular for hexagonal metals for which multiple dislocation slip families carry the plastic deformation. Strategies that have been proposed in the past to identify critical resolved shear stress (CRSS) values of individual slip families<sup>1</sup> yield disparate results [124, 21] and can be summarized into the following four categories.

**Surface slip trace statistics** The relative ease of activation of individual slip systems can be deduced from the frequency of slip trace observations on the surface of plastically deformed polycrystals, which was firstly proposed by Li et al. [74]. The inherent assumption of globally homogeneous stress was later tested by Hémery et al. [61], who simulated the development of grain-level

---

<sup>1</sup>basal slip on  $\{0001\} \langle 1\bar{2}10 \rangle$ , prism slip on  $\{10\bar{1}0\} \langle 1\bar{2}10 \rangle$ , pyramidal  $\langle a \rangle$  slip on  $\{10\bar{1}1\} \langle 1\bar{2}10 \rangle$ , and pyramidal  $\langle c+a \rangle$  slip  $\{10\bar{1}1\} \langle 2\bar{1}\bar{1}3 \rangle$

stress heterogeneity based on a two-dimensional (columnar) representation of the grain structure and interpreted observed slip traces in light of the simulated resolved stresses. While the averaged CRSS values were not found to be substantially different than for the assumption of a homogeneous stress, a larger dispersion of CRSS values was observed, which may also be a consequence of the assumption of a columnar grain structure.

**Micro-pillar compression** By compressing specifically oriented micro-pillars, the CRSS values of individual slip systems can be determined from the elasto-plastic transition in the load–displacement response in connection with the occurrence of surface traces that identify the active slip system. The main disadvantages of this technique are that the machining of micro-pillars by focused ion beam milling is a time-consuming process, and that the results are typically affected by size effects and uncertainty in the actual local stress state due to the sample taper and contact alignment between the sample and the platen. Therefore, the bulk CRSS values can only be extracted by careful extrapolation using results from different micro-pillar sizes, as has been done, for instance, for the CRSS value of basal slip for different Mg alloys by Wang et al. [123].

**Grain tracking by far-field high energy X-ray diffraction microscopy (ff-HEDM)** The initiation of specific lattice reorientation characteristics expected for exclusive basal or prism slip can be interpreted as an indication of predominant activity of (basal or prism) slip in grains that exhibit such characteristic reorientation. The corresponding CRSS values can then be directly identified based on the grain-average lattice strain present when the reorientation starts. Wang et al. [124, 125] tracked the evolution of lattice orientation and grain-averaged stress of hundreds of grains in CP-Ti and a Mg-Y alloy with *in situ* ff-HEDM tension tests.

**Adaptive crystal plasticity simulations** In these approaches, optimal CRSS values are established by finding the best match between experimental measurements and their simulated counterparts. For example, Baudoin et al. [5] used the stress–strain response and grain-scale slip activity of a CP-Ti oligocrystal with columnar grains to evaluate the ratio of basal to prism CRSS. Gerday

et al. [39] used the load–depth curves of Berkovich indentations into single grains of a Ti-5Al-5Mo-5V-3Cr-0.5Fe (wt%) alloy as a basis for manually tweaking the CRSS values of basal, prism, and pyramidal  $\langle c + a \rangle$  slip systems. Similarly, Sánchez-Martín et al. [118] were able to establish initial and saturated CRSS values of all four slip families and the hardening slope ( $h_0$ ) for a Mg-1Mn-1Nd (wt%) alloy by matching the hardness values across a range of inclination angles between the indentation axis and the  $\langle c \rangle$  lattice direction. Approaches that involve a guided optimization strategy, in contrast to the manual searches utilized in above studies, have the potential to more robustly identify the optimal constitutive parameters. For instance, Hama et al. [51] used the stress–strain curve, the evolution of the Lankford ( $r$ ) value, and the texture evolution along multiple deformation paths of polycrystalline CP-Ti samples to optimize the initial and saturated CRSS values and hardening slope  $h_0$ . Gong et al. [44] optimized the initial CRSS values in a dislocation density-based model of CP-Ti by matching simulated load–displacement curves of micro-cantilever bending tests to measured ones. Zambaldi et al. [136] established initial and final CRSS values of all four slip families in CP-Ti through Nelder–Mead optimization of the simulated load–depth curves and surface topographies resulting from conospherical indentations into two separate grains.

As the CRSS values reported for CP-Ti differ among the above mentioned methods (Figure 3.1), the question about their intrinsic reliability arises. Based on synthetic reference data, Chakraborty et al. [21] comprehensively analyzed the accuracy and precision of three specific instances of the above listed methods, namely, (i) surface slip trace statistics, (ii) inverse indentation analysis (IIA), and (iii) grain tracking with ff-HEDM. While IIA was not as precise nor accurate as the lattice orientation method, the IIA method does not require the extensive analysis required for synchrotron X-ray data and is, hence, simpler and more practical. However, an evaluation of IIA based on measured data that is expected to have more noises is missing, which motivates the work in Chapter 5.

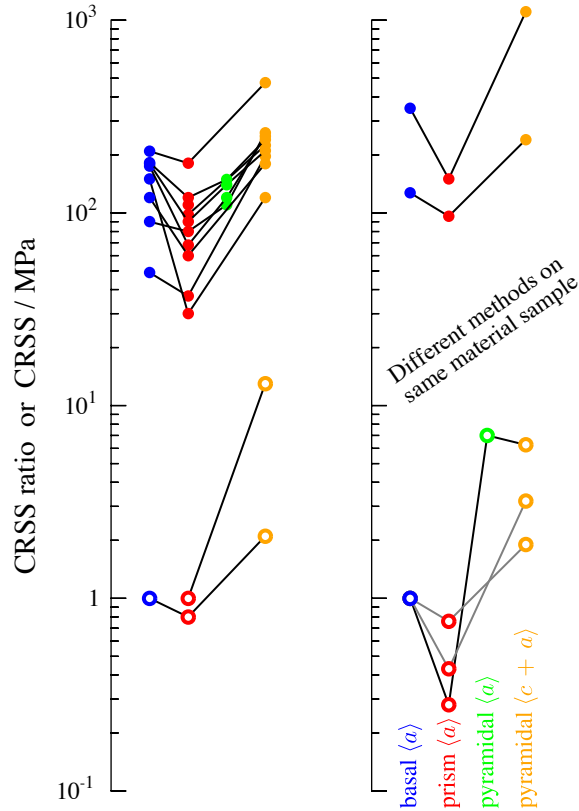


Figure 3.1: Disparate CRSS values of CP-Ti reported in the literature [21].

## 3.2 Establishing slip transfer parameters for crystal plasticity models

### 3.2.1 Modeling plastic deformation in polycrystals

Most engineering components made of metallic materials are polycrystals that consist of many (usually million) grains. Two approaches to computationally simulate plastic deformation in these aggregates are yield surface models and crystal plasticity models. The former approach relies on a stress plane yield function (Cauchy stress tensor formulation) to describe anisotropic deformation that satisfies yield surface evolution [4]. Clearly, this approach does not differentiate plastic micro-mechanism(s). It is limited to predicting macroscopic responses, for instance, texture evolution and stress-strain behavior. On the other hand, crystal plasticity models consider cumulative contributions of active micro-mechanisms, such as dislocation slip activity and twinning, and allow other fine details to be included.

Using both approaches in a continuum framework requires inter-grain compatibility and global equilibrium states, which also ensures local compatibility and equilibrium conditions at individual material points. To meet the former (global) requirements, homogenization schemes at different levels are used to tackle grain interactions with its surroundings. The most simple homogenization is to assume all grains deform uniformly, called Taylor–Bishop–Hill full constraints [12]. While this assumption conveniently guarantees compatibility at all scales, it averages anisotropic responses of individual grains such that any local heterogeneity is diminished. A less strict strategy, *i. e.*, self-consistent method, is to treat each grain as if it was embedded in a homogeneous “effective” matrix with the average properties of such an arrangement. The condition that the average of state variables (*e. g.*, stress and strain rate) over all grains has to be consistent with the magnitude of the corresponding macroscopic quantities [69] renders self-consistent solutions throughout the matrix. Models adopting this homogenization scheme are called self-consistent models. For instance, Kröner [66] and Budiansky and Wu [16] proposed the first models of this kind that reach plastic compatibility by fully elastic accommodation. However, when plastic deformation largely exceeds the elasticity, the matrix can be seen as a rigid body, which is essentially the same as the full constraints condition [69]. Another approach to accommodate plastic mismatch by an elasto-plastic decomposition was reported by Hill [57]. It was later implemented by Hutchinson [60] to simulate the stress-strain behavior of face-centered polycrystals. To solve large-strain deformation, Nemat-Nasser and Obata [92], Harren [54] developed a rate-dependent elasto-plastic model (elasto-viscoplastic, EVP) based on the Hutchinson [60] approach. In contrast to the above implementations that used yield surface models, Lebensohn and Tomé [69] proposed a viscoplastic self-consistent (VPSC) crystal plasticity model that neglects the elastic effect and only considers viscoplastic formulations [98] for stress calculations. Meanwhile, other homogenization schemes such as Mori–Tanaka [89], Mercier and Molinari [87], and mean-field homogenization (MFH) [30] have been developed to handle different material configurations, *e. g.*, composite materials with different phases.

With the help of characterization tools such as electron backscatter microscope (EBSD) and



3D synchrotron X-ray diffraction, large orientation gradients are often observed inside grains. This leads to the realization that plastic inhomogeneity not only happens between grains but also within each grain. To capture intragranular plastic inhomogeneity in crystal plasticity models, the homogenization scheme should be brought down to smaller scales than the average grain size (in other words, as fine-scale as it needs.). A different strategy is to calculate local Taylor factors based on the local kinematics [8, 103]. Local Taylor factors have also been used to explain pore nucleation: pores are more likely to happen at locations between hard and soft orientations where compatible shape change is difficult to maintain under stress [10].

Following these strategies, existing crystal plasticity models can capture intragranular plastic inhomogeneity to some extent. However, the most significant deviations between simulation and experimental characterization are often found in the vicinity of grain boundaries [9, 76, 77, 78], which are also locations where nucleation of damage sites or critical crack spots are usually observed. One possible reason is that these models do not use the actual grain (or boundary) geometries. Since each grain deforms differently according to the plastic strain within itself and the neighborhood grains, the deformation process is also dynamically evolving with the actual complex boundary conditions. A study by Zhang et al. [138] suggests that input geometry of grains and boundary conditions have a bigger impact than fine-tuning the constitutive parameters on simulating plastic inhomogeneity in polycrystals. They compared crystal plasticity modeling results of columnar grain geometry determined from surface EBSD and a more realistic 3D geometry with additional information from non-destructive differential aperture X-ray microscopy (DAXM). They found that a phenomenological model with the latter conditions could capture a fair amount of heterogeneity below the grain level. Another missing aspect in these models is the fine-scaled GB physics, for example, slip interactions with GBs. As introduced in Section 2.3, slip-GB interactions are complicated and primarily associated with stress concentration and size effects. Since there are no explicit boundary properties (layers) included in the current finite element models, the “boundaries” among grains are intrinsically transparent to all slip activity. Haouala et al. [53] compared simulated bi-crystals deformed in tension with fully transparent, partially transparent,

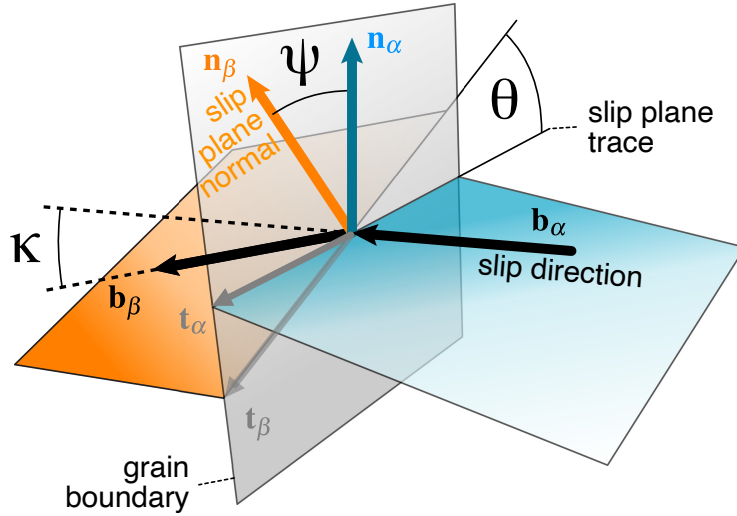


Figure 3.2: Geometrical relationship between slip in the incoming grain (blue) and receiving grain (orange) transmitting across the grain boundary.  $\kappa$  is the angle between incoming and outgoing slip directions,  $\psi$  is the angle between plane norms, and  $\theta$  is the angle between the plane traces on the boundary [52].

and opaque boundaries to test how boundary transparency affects the modeling results. Increasing stress concentration was found to correlate with decreasing boundary transparency. A comparison between simulation and experiments that also suggests the mismatch is caused by lacking slip–GBs physics in the models was in bi-crystal nanoindentations[116]. In that work, CPFEM simulation was found to consistently overestimate the elevations in the receiving grain. Therefore, introducing these slip–GBs features to the existing modes is necessary to further improve the prediction of inhomogeneous deformation—especially spatially near GBs—in polycrystalline metals.

### 3.2.2 Prior work on establishing effective slip transfer metrics

**Characterization by surface trace analysis** Most of the slip transfer mechanisms described in Section 2.3 were studied/confirmed by transmission electron microscopy (TEM) or high-resolution TEM [72, 73, 80, 82, 93, 114] images that reflect the nature of dislocation via contrast analysis. However, TEM is limited to a small volume and is *typically* destructive to the sample (also difficult sample preparation). An alternate approach is electron channeling contrast imaging (ECCI) that is also based on the diffraction contrast analysis [24, 86, 90, 113, 133]. It is basically non-destructive

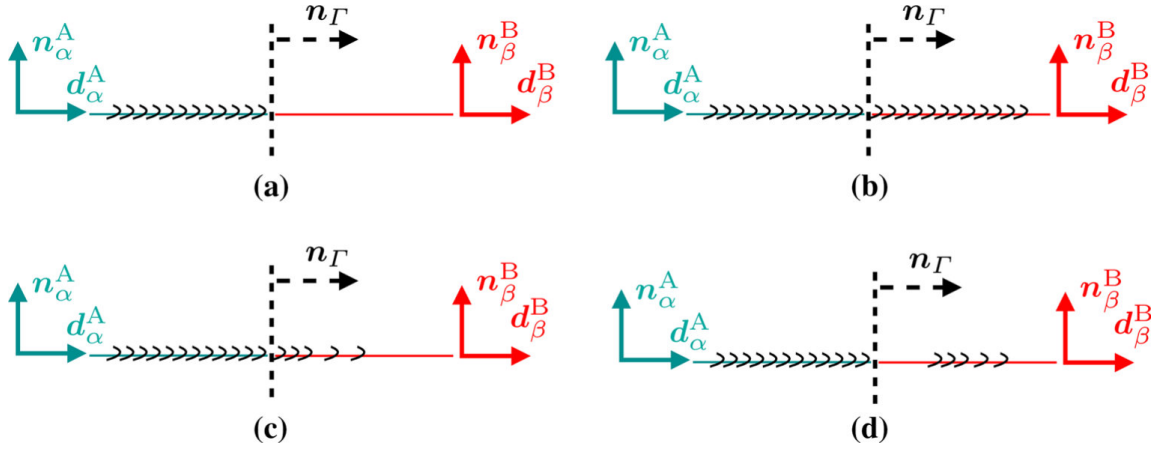


Figure 3.3: Continuity and discontinuity of slip transfer surface traces [6].

and can scan over a large volume that allows the dislocation nature to be determined. Nevertheless, it still requires meticulous surface preparation and good channeling conditions to get high-quality images.

Some other experimental techniques have been developed to characterize slip activities near GBs over the years [52, 72, 73, 79, 80, 82, 93, 114, 115, 116]. For instance, Su et al. [117] used atomic force microscopy (AFM) to measure surface traces on both sides of GBs that also contain Z-displacement components, which led to the quantification of  $\mathbf{b}_r$  magnitude in CP-Ti. The recent development of digital image correlation (DIC) [79, 115] enables high-resolution strain mapping (full-scale) of samples at different deforming stages (strain levels). With the help of DIC, Linne et al. [79] investigated relationships between slip transfer and grain boundary sliding (GBS) in high purity aluminum. Another emerging technique that can provide similar information is high resolution electron backscatter diffraction (HR-EBSD) or cross-correlation EBSD [47, 68]. Using this approach, Guo et al. [47] studied slip-GB activities and their correlation with stress concentration in CP-Ti deformed at low strain level.

A direct method for characterizing slip-GB interactions is by observing surface slip traces on

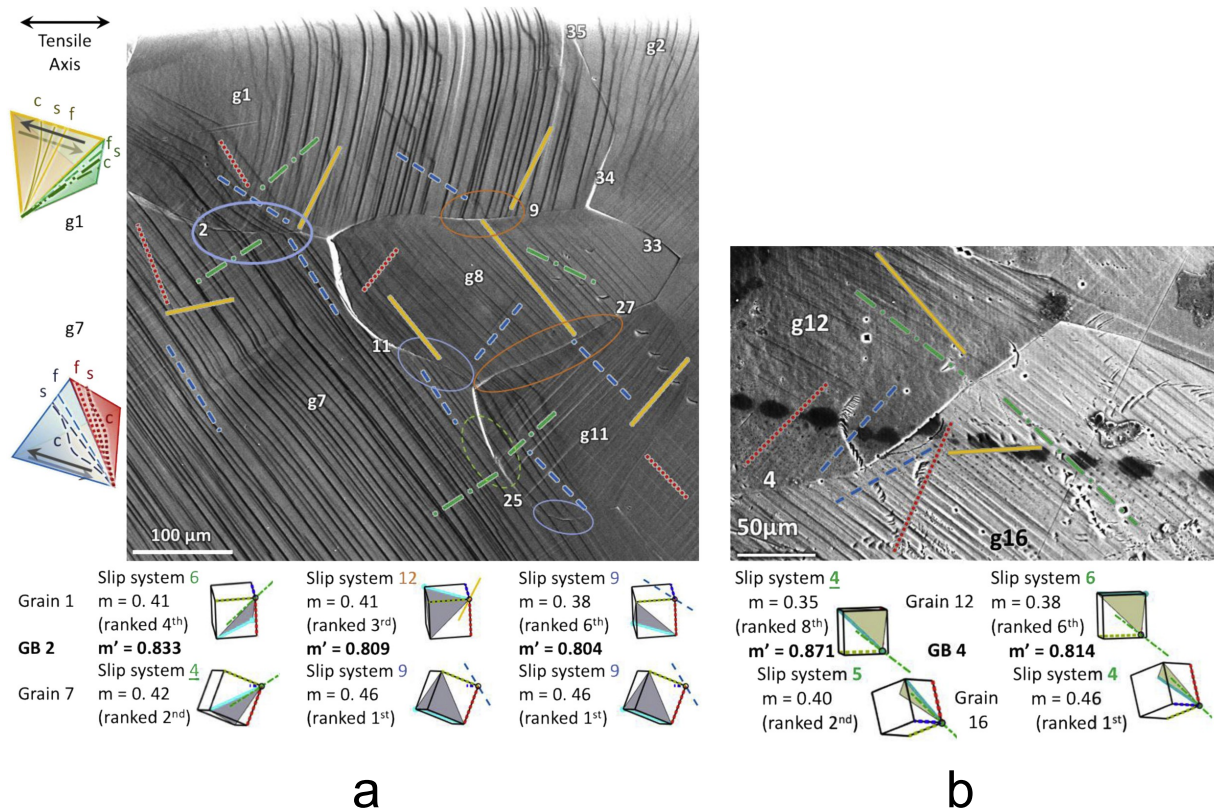


Figure 3.4: Some slip transfer and blocking cases in tensioned oligo pure Al sample [9].

both sides of grain boundaries by optical microscope or scanning electron microscopy (SEM) [67, 110, 130]. Incoming and outgoing slip traces across grain boundaries can appear in varying shapes and different degrees of continuity due to free surface effects and constraining characterization to a 2D plane. For instance, Fig. 3.3b and Figure 3.3c demonstrate the continuous slip transfer cases where the outgoing slip traces differ in length. In contrast, Fig. 3.3a shows a slip blocked case, and Fig. 3.3d shows a discontinuous case of slip transfer event where the trace of the outgoing slip starts a distance from the boundary. While clear slip trace continuity across GBs is strong evidence for slip transfer events (the boundary between grain 8 and 11 in Fig. 3.4a), it makes identification of slip blocking events dubious (discontinuous case) that require careful judgments. Some additional aspects of assisting identification of slip blocking are checking boundary topography and Schmid factor of potential slip systems in either grain. For example, slip lines parallel to slip system 6

(dashed green line in Fig. 3.4b, grain 12 and grain 16) are slip blocking cases because both traces fade away near the boundary, and system 6 has a low-rank Schmid factor in the system. Grain boundary 9 in Fig. 3.4a also shows slip blocking events as slip traces suddenly stop at the boundary where a ledge can also be clearly observed.

**Slip transfer parameters and conditions** As motivated by the aforementioned need discussed in Section 3.2.1, efforts have been made to understand slip transfer occurrences across grain boundaries. These works suggest slip transfer across GBs depend on factors including local stress states, geometric alignment of incoming and outgoing slip systems, their types (edge or screw), inclination of boundary, and boundary properties (type, energy, structure *etc.*) [6, 7, 8, 47, 72]. However, most widely investigated metrics are geometrical metrics that take into account grain boundary inclination and slip system orientations and these factors seem to be dominant [47] in slip transfer phenomena. Geometrical metrics are illustrated as follows:

**Criterion by Livingston and Chalmers** Livingston and Chalmers [80] were among the first to study slip transfer. Their metric ( $N$ ) only considers the geometrical alignment of the slip systems in the adjacent grains that is given by,

$$N = (\mathbf{n}_\alpha \cdot \mathbf{n}_\beta)(\mathbf{b}_\alpha \cdot \mathbf{b}_\beta) + (\mathbf{n}_\alpha \cdot \mathbf{b}_\beta)(\mathbf{b}_\alpha \cdot \mathbf{n}_\beta) \quad (3.1)$$

with  $\mathbf{b}_\alpha, \mathbf{b}_\beta$  the slip directions of incoming and outgoing slip system, respectively, and  $\mathbf{n}_\alpha, \mathbf{n}_\beta$  the slip plane normal, see Fig. 3.2. However, this metric does not account for boundary inclination.

**Lee–Robertson–Birnbaum (LRB)** Another metric ( $M$ ) proposed by Shen et al. [112], Lee et al. [72], Clark et al. [23] not only considers alignment of slip, but also accounts for grain boundary inclination,

$$M = (\mathbf{t}_\alpha \cdot \mathbf{t}_\beta)(\mathbf{b}_\alpha \cdot \mathbf{b}_\beta) \quad (3.2)$$

$$= \cos \theta \cos \kappa \quad (3.3)$$

where  $\mathbf{t}_\alpha, \mathbf{t}_\beta$  are slip plane intersections with the grain boundary plane, and  $\theta$  is the angle between them.  $\kappa$  is the angle between two slip directions. Information about the inclination of the grain boundary can be obtained by focused ion beams (destructive).

**Luster and Morris [82]** A similar effort metric  $m'$  (or  $m'_{\alpha\beta}$ ) was later proposed by Luster and Morris [82] and the formula to calculate it is as follows,

$$m' = (\mathbf{n}_\alpha \cdot \mathbf{n}_\beta)(\mathbf{b}_\alpha \cdot \mathbf{b}_\beta) \quad (3.4)$$

$$= \cos \psi \cos \kappa \quad (3.5)$$

where  $\psi$  is the angle between slip plane norm. Larger values of  $m'$  indicate the better geometrical alignment of the two systems on their slip planes in the adjacent grains, which is also a simplified version of Livingston–Chalmers N. As  $m'$  can be computed with surface orientation information (in contrast to LRB criterion), it has been widely adopted in the later slip transfer studies.

Although geometrical metrics are dominant factors, additional metrics reflecting resolved stress states and the difficulty of maintaining boundary continuity are also essential for slip transfer prediction. For example, Lee et al. [72] suggest that the resolved shear stress on the receiving side of grain should be maximized and that the magnitude of residual Burgers vector  $\Delta b_{\alpha\beta}$  has to be minimized. In the spirit of these suggestions, simultaneously considering or compounding multiple slip metrics that account for many possible aspects is a meaningful direction to explore. Bieler et al. [8] have given some pioneering work in this regard, and they are summarized as follows.

**Metric considering slip system activity and slip transparency** This metric ( $m'_{3m}$ ) accounts for both geometrical relationships and resolved stress. Based on the assumption that no more than three slip system pairs are likely to be dominant in a given grain and involved in slip transfer, it considers the average of top three  $m'$  values of the incoming and outgoing slip system pairs whose average Schmid factor values are also highest (all the considered slip systems should have Schmid factor values exceed a meaningful threshold, *e. g.*, 0.35). High geometrically necessary dislocation (GND) contents were found to correlate with lower  $m'_{3m}$  in a four-point bending test of tantalum

sample by Bieler et al. [8]. However, this method may have uncertainty arising from 1) local stress may deviate from the uniaxial stress tensor, and 2) orientations close to grain boundaries may deviate from the average grain orientation.

**Metrics considering weighted sum of geometric factors** Three formulations that combine the geometrical metrics ( $m'_{\alpha\beta}$ ,  $\text{LRB}_{\alpha\beta}$ , all three cosines  $S_{\alpha\beta}$ ) with accumulated shear and  $m'_{\alpha\beta}$  with weighted Schmid factor  $m$  are presented by Bieler et al. [8].

$$m'_\gamma = \frac{\sum_\alpha \sum_\beta m'_{\alpha\beta}(\gamma^\alpha \gamma^\beta)}{\sum_\alpha \sum_\beta (\gamma^\alpha \gamma^\beta)} = \frac{\sum_\alpha \sum_\beta \cos \kappa \cos \psi(\gamma^\alpha \gamma^\beta)}{\sum_\alpha \sum_\beta (\gamma^\alpha \gamma^\beta)}$$

$$\text{LRB}_\gamma = \frac{\sum_\alpha \sum_\beta \text{LRB}_{\alpha\beta}(\gamma^\alpha \gamma^\beta)}{\sum_\alpha \sum_\beta (\gamma^\alpha \gamma^\beta)} = \frac{\sum_\alpha \sum_\beta \cos \kappa \cos \theta(\gamma^\alpha \gamma^\beta)}{\sum_\alpha \sum_\beta (\gamma^\alpha \gamma^\beta)}$$

$$S_\gamma = \frac{\sum_\alpha \sum_\beta S_{\alpha\beta}(\gamma^\alpha \gamma^\beta)}{\sum_\alpha \sum_\beta (\gamma^\alpha \gamma^\beta)} = \frac{\sum_\alpha \sum_\beta \cos \kappa \cos \psi \cos \theta(\gamma^\alpha \gamma^\beta)}{\sum_\alpha \sum_\beta (\gamma^\alpha \gamma^\beta)}$$

$$m'_m = \frac{\sum_\alpha \sum_\beta m'_{\alpha\beta}(m^\alpha m^\beta)}{\sum_\alpha \sum_\beta (m^\alpha m^\beta)} = \frac{\sum_\alpha \sum_\beta \cos \kappa \cos \psi(m^\alpha m^\beta)}{\sum_\alpha \sum_\beta (m^\alpha m^\beta)}$$

However, assessing all four parameters based on the Ti-5Al-2.5Sn sample shows that they contain irrelevant information, which requires filtering this noisy information by some measures.

**Slip transfer metrics in Al oligocrystals** In recent works by [2, 9], four slip transfer metrics, *i. e.*, misorientation angle,  $m'_{\alpha\beta}$ ,  $\text{SF}_\alpha + \text{SF}_\beta$ ,  $\Delta b_{\alpha\beta}$ , and several of their combinations were investigated based on two pieces of tensioned oligo Al samples (cube and rotated-cube texture, respectively). A total of 222 boundaries were carefully assessed and labeled based on the observation of slip

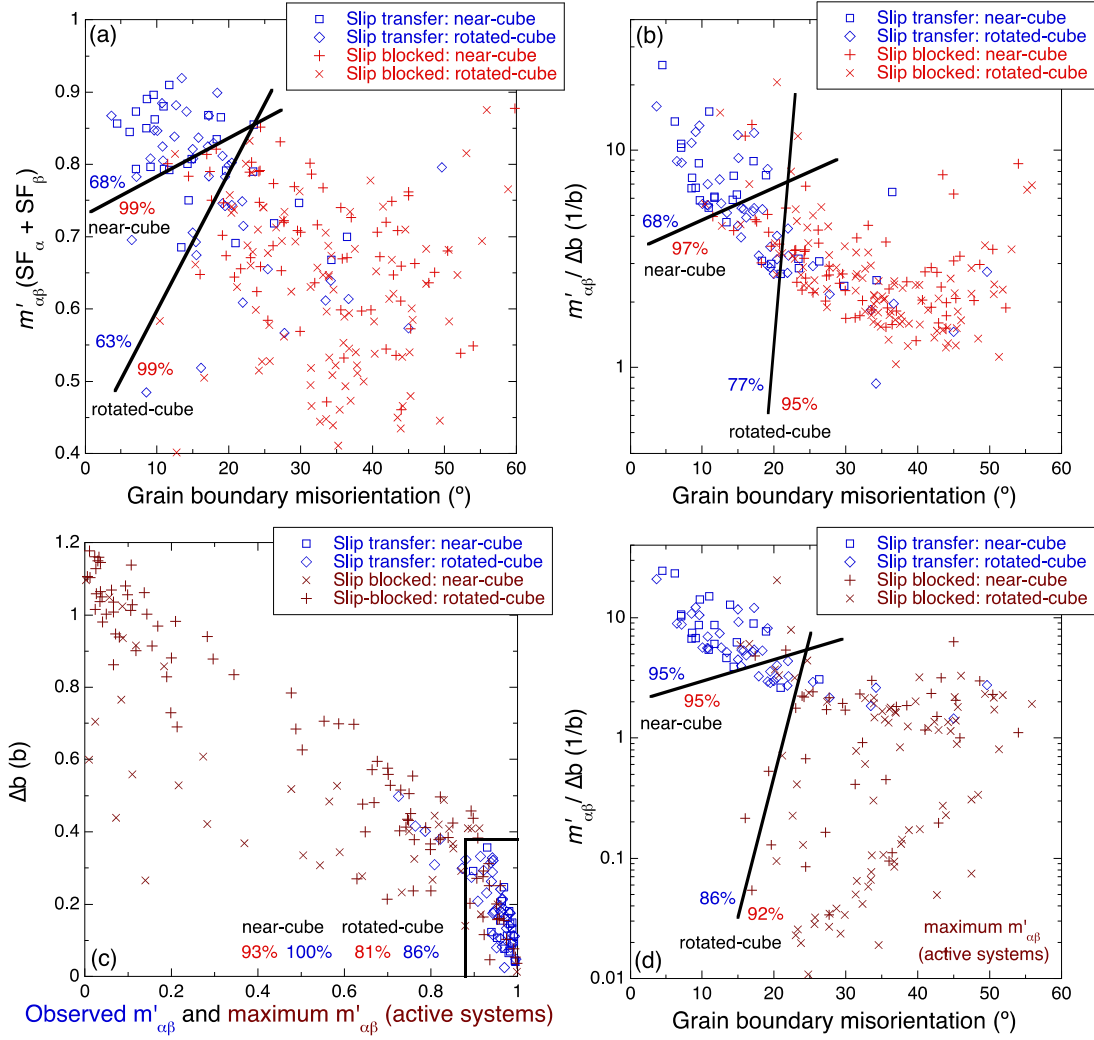


Figure 3.5: Separating slip transfer and no transfer cases by line drawing in 2D plotting [2].

transfer evidence (“transfer”, “no transfer”, or “not sure”). Slip transfer metrics were evaluated by manually classifying “transfer” data in a 2D plot<sup>2</sup>, as shown in Fig. 3.5.

With the help of manual approach, slip transfer was found to occur at low-angle GBs when  $m'_{\alpha\beta} > 0.97$  [9] or  $m'_{\alpha\beta} > 0.9$  [2] together with normalized residual Burgers vector magnitude

<sup>2</sup>Labeled data were plotted in a 2D figure with respect to a combination of two metrics (x and y axis respectively) and a line to separate the “transfer” and “no transfer” data were manually drawn.



$\Delta b_{\alpha\beta} < 0.35$ . Nevertheless, since this approach is limited to 2D plotting, it cannot be used to further investigate the inter-relationship between more than two metrics and whether a combination of three or more metrics can improve the separability (prediction) of slip transfer data. In addition, this approach may not reach the maximum accuracy because it relies on human observation, and the results vary with different analyzers. To overcome human limitations, a novel approach based on artificial neural networks (ANN) is adopted in this study to further assess the same dataset from a data-driven perspective, which is also able to extend the dimension to six. Details of this work are given in Section 4.2 and Chapter 6.

### 3.3 Variant selections in transformation between hexagonal $\alpha$ and body-centered cubic $\beta$ phase

The solid-state transformation between hexagonal ( $\alpha$  phase at low temperature) and body-centered cubic (bcc) phase ( $\beta$  phase at high temperature) is commonly observed in titanium, zirconium, and “shape memory” alloys such as Ni-Ti [40, 63, 100, 137]. It is an essential thermo-mechanical processing technique to enhance the mechanical properties by altering the texture or the second phase precipitate distribution of the alloys [40, 95, 139]. Due to crystal symmetry (both hexagonal and cubic) and lattice rotations associated with the transformation processes, the orientation relationship of the original and resulting hexagonal lattice (or two resulting hexagonal lattices) is not uniquely determined. Thus, investigating all the possible variants is vital to establish an understanding of such phase transformation mechanism.

In a study of  $\beta \rightarrow \alpha$  transformation in Zr, Burgers [17] proposed an orientation relationship from parent  $\beta$  to product  $\alpha$  as  $\beta\{110\} \parallel \alpha\{0001\}$  and  $\beta\langle 111 \rangle \parallel \alpha\langle 2\bar{1}\bar{1}0 \rangle$ , which is often referred to as the Burgers orientation relationship (BOR). Based on this BOR, a given  $\beta$  orientation is associated with 12 possible  $\alpha$  orientations (a summary of these variants can be found in Wang et al. [126]). However, only 6 possible  $\beta$  orientations correspond to a given  $\alpha$  orientation in the reversed transformation. The BOR obedience in  $\alpha \rightarrow \beta$  transformation was later confirmed in commercially pure Ti [111]. Furthermore, Glen and Pugh [43], Karthikeyan et al. [63] identified

57 distinct orientation relationships among  $\alpha$  variants (including the invariant/unchanged case) from  $\alpha \rightarrow \beta \rightarrow \alpha$  transformation by checking a total of 72 possible cases.

Many experimental works have reported the sharpening of product  $\alpha$  texture [26, 40, 81, 127, 139] or texture memory effects [95, 104, 127] (the original  $\alpha$  textures are maintained either perfectly or to some extent), which are believed to be indications of variant selection. There is a debate on which step in  $\alpha \rightarrow \beta \rightarrow \alpha$  has the most considerable influence on the variant selections. Romero et al. [104] reported no variant selection in the heating ( $\alpha \rightarrow \beta$ ) process but significant selection in the cooling ( $\beta \rightarrow \alpha$ ) process, while Daymond et al. [26] showed that there is much stronger variant selection in the  $\alpha \rightarrow \beta$  process than the  $\beta \rightarrow \alpha$  process. In fact, the majority of the papers on variant selection are focused on the  $\beta \rightarrow \alpha$  process [40, 81, 127, 95, 104, 127, 139]. For instance, precipitates showing three or four  $\alpha$  variants are often observed in Zr and Ni-Ti alloys after the completion of  $\beta \rightarrow \alpha$  transformation at low temperature [38, 40, 41, 88].

The mechanism(s) and factors contributing to the variant selections in this phase transformation are not fully established yet. One explanation is that variant selections are driven by the system trying to minimize the average shape strain during the transformation, known as self-accommodation [126]. This is supported by a work presented by Wang et al. [126], who were able to identify two clusters of three  $\alpha$  variants from  $\beta \rightarrow \alpha$  transformation with smallest average shape strain using lattice correspondence approach—calculation based on two sets of three non-coplanar axes in before- and after-transformed configurations respectively. Other aspects such as external deformation conditions [55, 127] and surface effects [127, 132] are also possible contributors to the variant selections.

Although in-situ observation of phases in the transformation can be realized by neutron diffraction [26, 81, 127], most papers discussing variant selections depend on the reconstructed  $\beta$  texture from product  $\alpha$  due to the limitation of the operating temperature and facility availability. Despite there being much discussion about the influence of  $\beta$  phase texture on product  $\alpha$  texture, no one has shown the influence of the initial  $\alpha$  texture on the product  $\alpha$  texture while considering the complete  $\alpha \rightarrow \beta \rightarrow \alpha$  process. For such studies, challenges are mainly due to a lack of historical

information at each transformation process step. Hence, an approach that enables the reconstruction of historical information at a particular step will be helpful to facilitate the studies on variant selections.

## CHAPTER 4

### METHODOLOGY

In this chapter, detailed explanations of 1) inverse indentation analysis (IIA) to establish consistent critical resolved shear stress (CRSS) values, particularly for hexagonal crystals, 2) a novel approach to evaluate slip transfer metrics by artificial neural network analysis of surface observations of slip transfer traces, and 3) a method to calculate kinematics of phase transformation between hexagonal  $\alpha$  and body-centered cubic  $\beta$  crystals, are presented in the following three sections in the respective order.

#### 4.1 Inverse indentation analysis (IIA)

The basis of the inverse IIA method is the comparison of simulated and actual crystal indentations in terms of the load–depth response and resulting (pile-up) surface topography, which was firstly introduced by Zambaldi and Raabe [135]. The optimal constitutive parameters are obtained by iteratively updating the parameters until minimum deviation (fitness) between the simulated and experimental responses (of one or multiple orientations) is achieved (shown in Fig. 4.1). Chakraborty and Eisenlohr [19] reported that optimization of *single* crystallography orientation indentation is sufficient based on synthetic cubic crystal data. They applied the same analysis to hexagonal crystal (synthetic data as well) and found that the conclusion also holds for the selected orientations having good sensitivity to all considered slip systems [21].

The work in this thesis adopts most of the machinery from the former papers to *actual* measured data with several improvements summarized in this section.

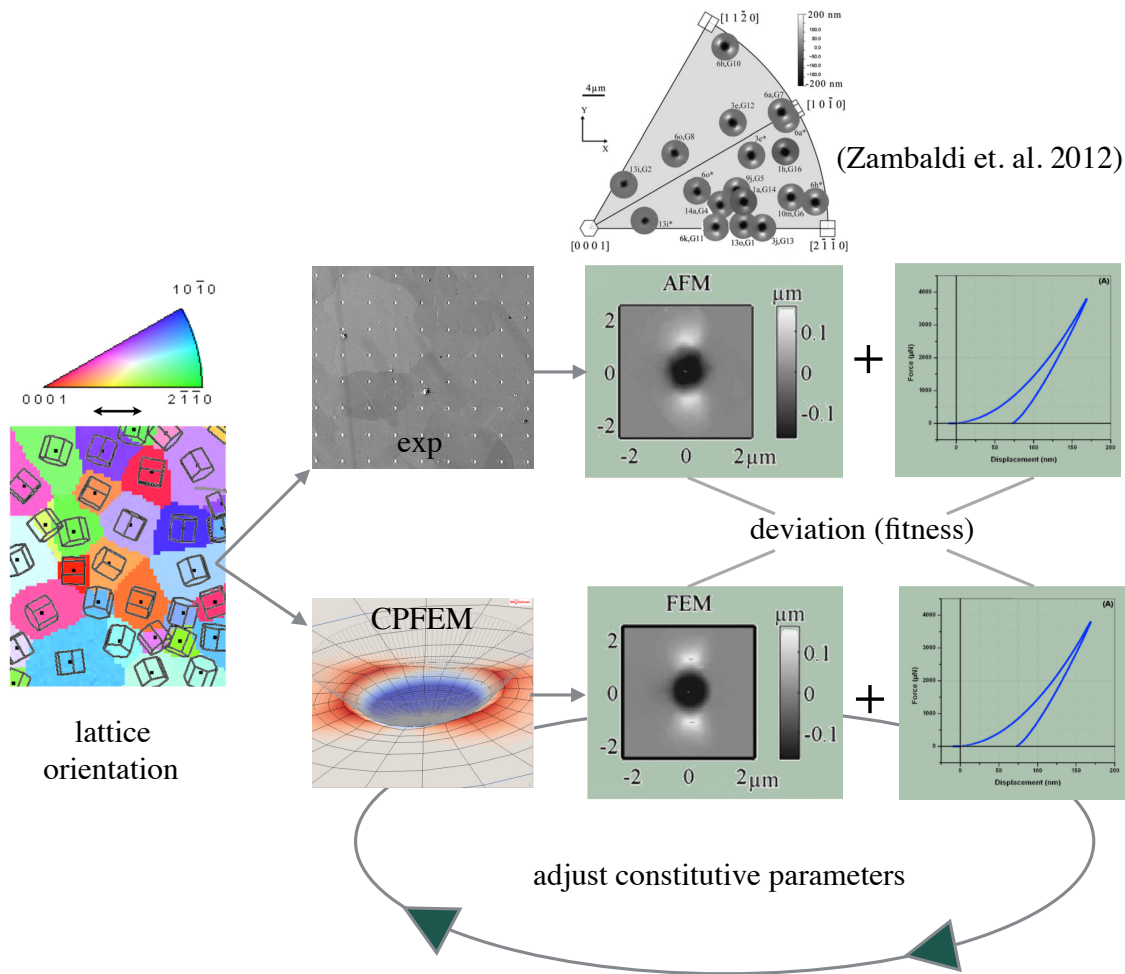


Figure 4.1: Schematic of establishing constitutive parameters from inverse indentation optimization.

#### 4.1.1 Nanoindentation

Indentation is an important mechanical test widely used for characterizing mechanical properties of materials due to its easy operation, less destructive nature (small deformation volume), and simple sample preparation. With the advancement in precise control systems, an indentation can be conducted at the nano- to micrometer scale, which is known as nanoindentation or instrumented indentation testing (IIT) [97]. This technique enables indentation(s) into a single grain (away from the boundary vicinity) such that the intrinsic single crystal properties can be studied conveniently. For example, hardness values and elastic moduli can be obtained by analyzing load-depth curves

based on the Oliver and Pharr [96] method.

**Orientation informed nanoindentation** A cono-spherical diamond tip (Fig. 4.2 right) with a radius of  $1\ \mu\text{m}$  and a cone angle of  $90^\circ$  inside the nanoTest Alpha (Fig. 4.2 leftmost) machine was used in this study. To extend its application to high temperatures, the machine employs horizontal direction as the indenting direction due to thermal noise is usually the smallest along this direction.

A grid of indents is performed into the flat surface of a well-polished polycrystalline sample. Then, an EBSD orientation map of the region is superimposed with the corresponding optical or SEM image that shows these indents. Figure 4.3 presents an example of such an overlay image. Indents with desired orientations are selected, and their surface topography is measured by atomic force microscopy (AFM).

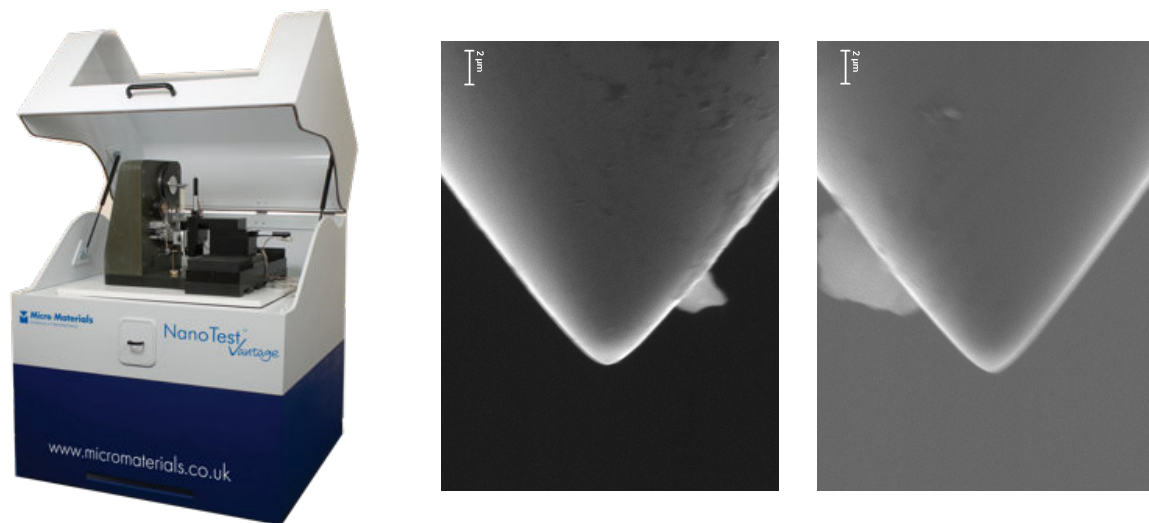


Figure 4.2: Leftmost: nanoTest Alpha, Micro Materials Ltd. Right two: SEM images of the diamond indenter tip with  $1\ \mu\text{m}$  radius and  $90^\circ$  cone angle before and after  $90^\circ$  rotation.

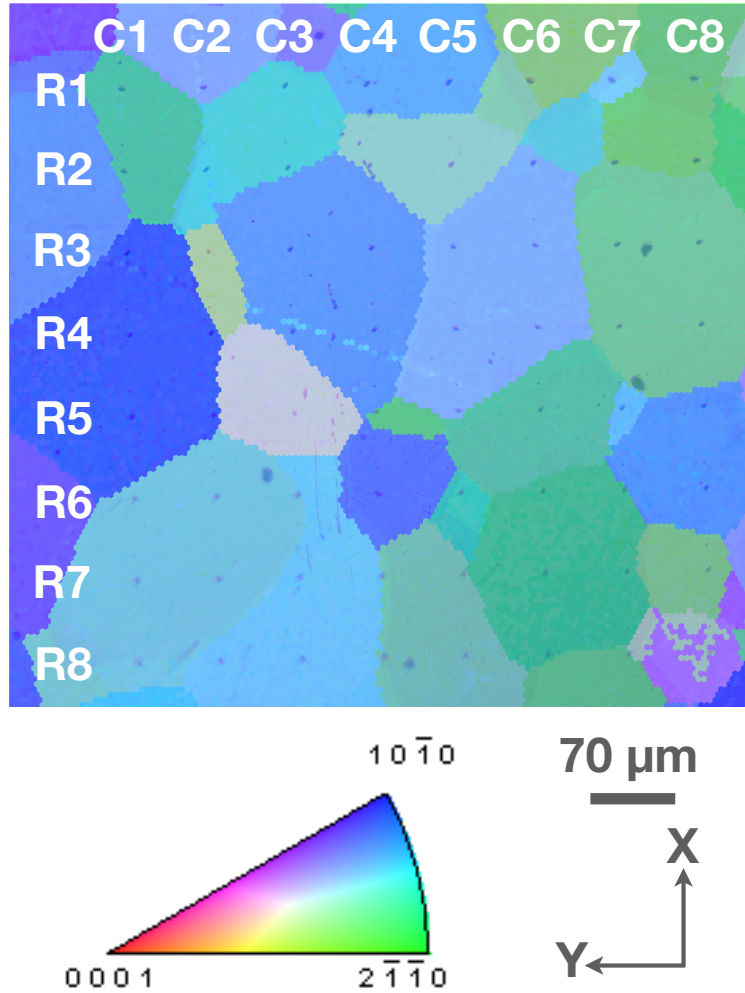


Figure 4.3: Orientation informed nanoindentation in polycrystalline CP-Ti.

#### 4.1.2 Crystal plasticity finite element simulation

**Indentation mesh discretization** Each indented grain was modeled as a cylindrical deformable body and discretized with a mesh (Fig. 4.4, C3D8 element) that transitions from square-shaped at the center to radially symmetric at the perimeter. The optimal height to width ratio of the elements beneath the center where initial contact takes place is found to be around 2. The displacements of all outside nodes were fixed except on the indented (top) surface. Coulomb friction with a coefficient of 0.1 was assumed between the rigid conospherical indenter and the indented single crystal. Similar to prior work [19], the phenomenological power-law [98] implemented in the Düsseldorf Advanced Material Simulation Kit (DAMASK) [106] was used as crystal plasticity constitutive

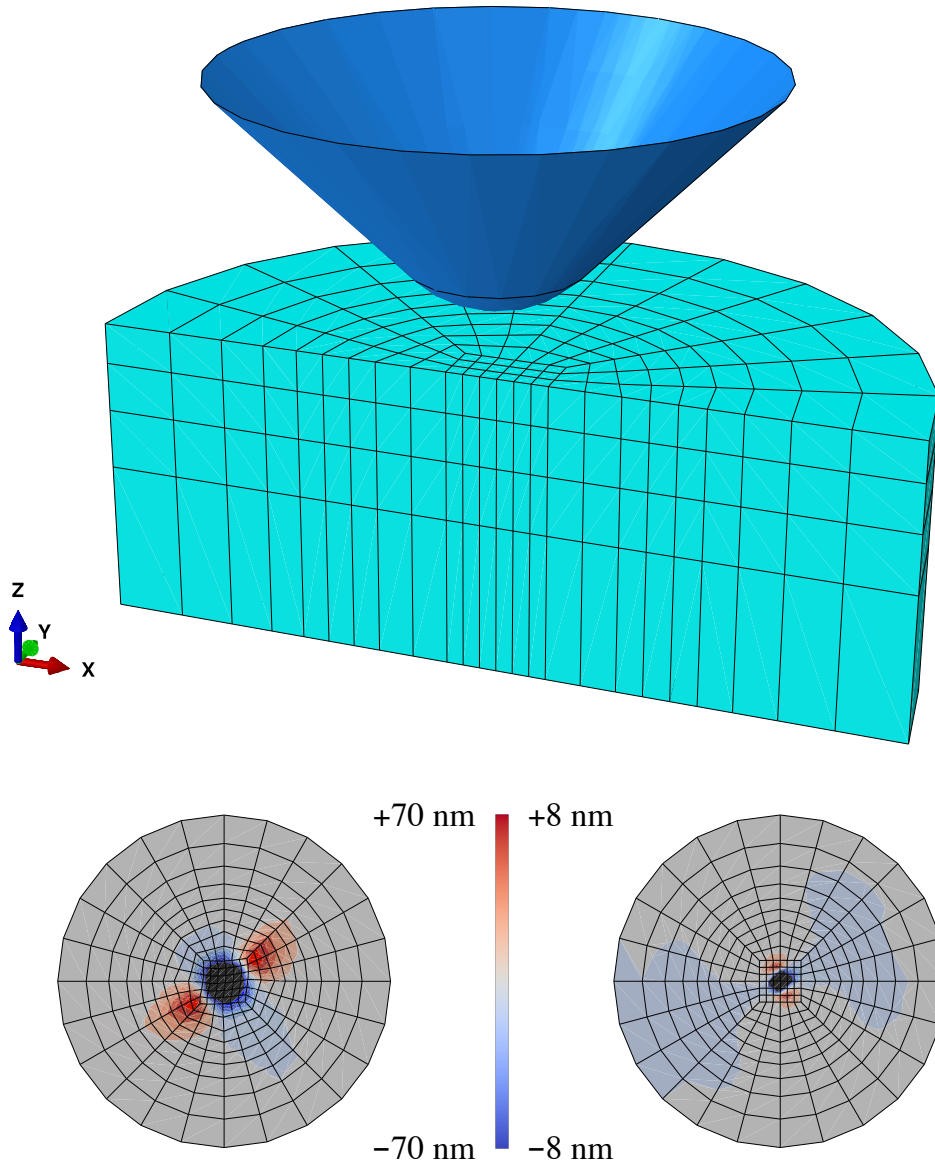


Figure 4.4: Finite element discretization of a cylindrical single crystal with  $4\ \mu\text{m}$  radius and  $3\ \mu\text{m}$  thickness used in the indentation simulations (only half of the total of 1008 C3D8 elements is shown). Conospherical indenter is modelled as a rigid analytical surface with  $90^\circ$  cone angle. Top-down views after 200 nm (left) and 50 nm (right) deep indentation illustrate examples of resulting simulated surface topography for two distinct crystal orientations.



description and installed as a user subroutine within the finite element software ABAQUS 2017. Simulations used adaptive time stepping and typically finished successful indentations in about 1000 to 4000 increments.

**Kinematic description** The current model is based on the multiplicative decomposition of the total deformation gradient  $\mathbf{F}$  into plastic and elastic components for describing the kinematics under a large strain framework [71, 107],

$$\mathbf{F} = \mathbf{F}_e \mathbf{F}_p \quad (4.1)$$

where  $\mathbf{F}_e$  is the elastic deformation gradient and  $\mathbf{F}_p$  is the plastic deformation gradient. The elastic part is resolved by Hooke's law and the plastic deformation  $\mathbf{F}_p$  is related to plastic velocity gradient  $\mathbf{L}_p$ ,

$$\dot{\mathbf{F}}_p = \mathbf{L}_p \mathbf{F}_p \quad (4.2)$$

The plastic velocity gradient is additively composed from slip rates on individual slip systems,

$$\mathbf{L}_p := \sum_{\alpha} \dot{\gamma}^{\alpha} \mathbf{s}^{\alpha} \otimes \mathbf{n}^{\alpha} \quad (4.3)$$

where the unit vectors  $\mathbf{s}^{\alpha}$  and  $\mathbf{n}^{\alpha}$  are the slip direction and slip plane normal for slip system  $\alpha = 1, 2, 3, \dots, k$ . The shear rate  $\dot{\gamma}^{\alpha}$  due to individual slip system is driven by the resolved shear stress,

$$\tau^{\alpha} = \mathbb{C}(\mathbf{F}_e^T \mathbf{F}_e - \mathbf{I})/2 : \mathbf{s}^{\alpha} \otimes \mathbf{n}^{\alpha} \quad (4.4)$$

**Phenomenological power-law description** Shear rate is governed by resolved shear stress  $\tau^{\alpha}$  and slip resistance  $\xi^{\alpha}$  of individual slip system  $\alpha$ .

$$\dot{\gamma}^{\alpha} = \dot{\gamma}_0 \left| \frac{\tau^{\alpha}}{\xi^{\alpha}} \right|^n \text{sgn}(\tau^{\alpha}) \quad (4.5)$$

The evolution of slip resistance is related to the sum of the shear on all other slip systems,

$$\dot{\xi}^{\alpha} = \sum_{\beta} h^{\beta} q^{\alpha\beta} \left| \dot{\gamma}^{\beta} \right|, \quad (4.6)$$

where  $q^{\alpha\beta}$  is the cross-hardening matrix,  $h^\beta$  is the hardening factor and is expressed as below.

$$h^\beta = h_0^\beta \left( 1 - \frac{\xi_0^\beta}{\xi_\infty^\beta} \right)^a \quad (4.7)$$

In this study, the initial slip resistance for basal  $\xi_0^{\text{basal}}$ , prism  $\xi_0^{\text{prism}}$ , and pyramidal  $\langle c+a \rangle$  slip  $\xi_0^{\text{pyr}\langle c+a \rangle}$  are of primary interest as they establish the initial yielding and their saturation levels are not necessarily achieved. Other parameters are fixed values that are shown in Table 5.1.

### 4.1.3 Non-convex optimization

As proposed by Chakraborty et al. [21], the optimal parameters are achieved by a two-step optimization process, *i. e.*, particle swarm optimization (PSO) followed by Nelder–Mead optimization, to render a most efficient performance. Since PSO supports simultaneous exploits within each iteration that can be realized by parallel execution, the first step ensures a fast and exhaustive exploration of the parameter space as the computational capacity allows. Then the particles with the best fitness values (parameter space dimension + 1) are used as the initial simplex for the Nelder–Mead optimization to get more deterministic results.

**Nelder–Mead (N–M) simplex optimization** The Nelder–Mead simplex algorithm was initially proposed by Nelder and Mead [91] in 1965. It has been one of the best-known algorithms to solve various unconstrained optimization problems due to its simplicity and ease of implementation. The standard N–M simplex algorithm constructs a simplex having N+1 vertices and iteratively relocates the worst vertex until the simplex has moved and shrunk to an optimum location in the N-dimensional parameter space. Given that the N–M simplex algorithm does not depend on gradient information, it can be applied to solve non-convex optimization problems. Implementation details for IIA can be found in Chakraborty and Eisenlohr [19].

**Particle swarm optimization (PSO)** The particle swarm optimizer was firstly introduced by [31, 64]. This optimizer mimics the unpredictable choreography of a bird flock and is further

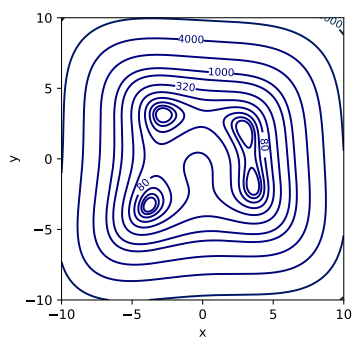
developed for multi-dimensional searches with acceleration by distance [32]. In this study, 20 particles (potential solutions) are used to explore a normalized parameter space with the dimension of three (the number of parameters). Particles are initialized at random locations and assigned random initial velocities. Each particle is attracted by two types of “attractors” that are at history global best ( $\mathbf{g}$ ) and self best locations ( $\mathbf{p}_i$ , with  $i$  the index for the particle), see Eq. (4.8). The maximum magnitude of velocity for each particle is limited to a cut-off value,  $v_{\max}$ . Each particle also has a random inertial factor ( $w_i$ ) that carries the momentum from the previous motion, and it will be updated to a new location after each generation. Figure 4.5 shows how PSO algorithm works in an example to find a minimum of Himmelblau’s function within 25 iterations.

$$\mathbf{v}_i = w_i \mathbf{v}_i + (c_1 \text{ rnd1}) \mathbf{p}_i + (c_2 \text{ rnd2}) \mathbf{g} \quad (4.8)$$

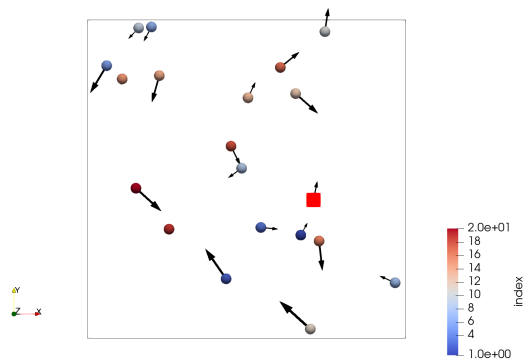
$$\mathbf{x}_i = \mathbf{x}_i + \mathbf{v}_i \quad (4.9)$$

The parameters for the PSO used are  $c_1 = c_2 = 1.5$ , suggested by Eberhart and Shi [32].  $\mathbf{p}_i$  and  $\mathbf{g}$  are all initialized with infinity at the beginning of the optimization. It is expected that indentation simulation cannot completely converge with some “bad” parameter sets. A simple modification to address such issues is proposed that the particle’s pbest attractor is no longer considered for the regions where no viable solution to the fitness function can be found.

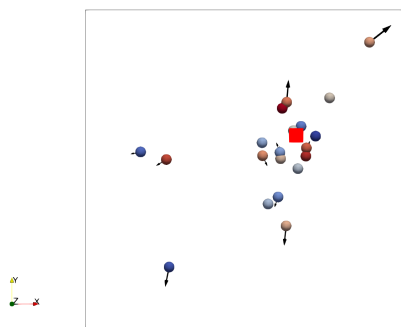
In contrast to N–M, PSO supports parallel execution for particles, which can significantly expedite the optimization process by the magnitude of the number ( $N_{\text{particle}}$ ) of particles ( $N_{\text{particle}} = 20$  in this study).



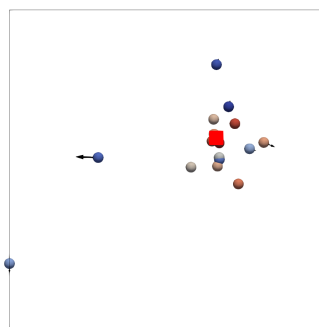
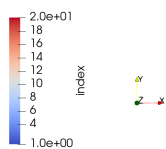
Himmelblau's function



iteration 1



iteration 10



iteration 25

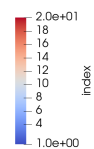


Figure 4.5: Top row: Himmelblau's function has 4 identical local minima shown in contour plots. Bottom row: schematics of finding one of the local minima of Himmelblau's function (top right one in contour plots, see red square in bottom figures which is the global best solution) using Particle Swarm Optimization in 25 iterations ( $N_{\text{particle}} = 20$ ,  $N_{\text{iteration}} = 0, 10, 25$  from left to right, bounds are  $[-10,10]$  for both dimensions).

#### 4.1.4 Surface topography upscaling

To minimize the influence of surface roughness on measured surface topography, the surface needs to be as clean as possible and an adequately deep indentation is preferred. However, the cost to run a single indentation simulation is high (usually 1000 to 4000 iterations in our simulations), let alone doing hundreds of them that are typically required for the parameter optimization problems. Given that the phenomenological description used in this study does not have size influence, a method to reduce the computational cost is to upscale the simulated surface topography from a small indentation depth (source depth) to the *actual* measured indentation depth (target depth) in two directions, *i. e.*, radial and Z displacement directions (Fig. 4.6 leftmost).

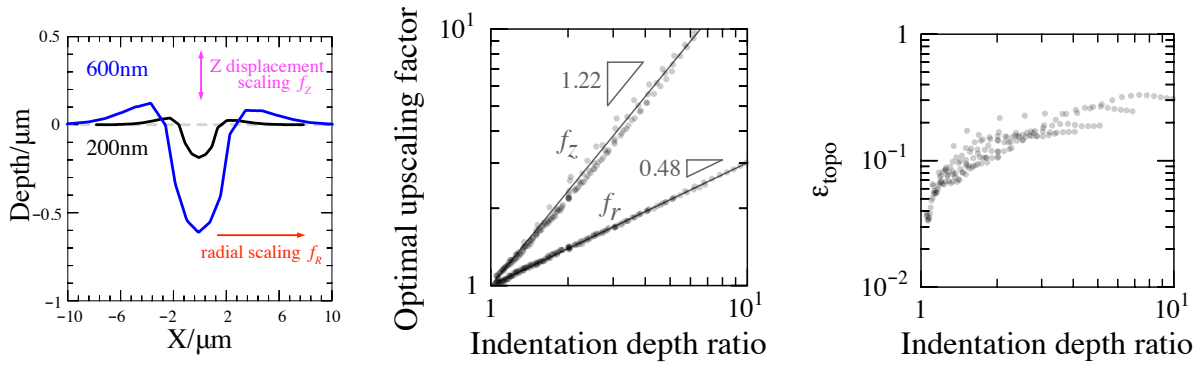


Figure 4.6: Optimal scaling factors (middle) to upscale simulated indentation surface topography in Z displacement and radial direction (left). Relative deviations (errors) between simulated upscaled topography and the (simulated) topography at the target depth (right).

The ratio of the target depth to source depth is called the indentation depth ratio, which means how many times the indentation will be upscaled later. For each indentation depth ratio in Fig. 4.6 middle plot, the optimal scaling factors ( $f_z, f_r$ ) for both directions are established by minimizing the deviations (errors) between simulated upscaled topography and the (simulated) topography at the target depth by Nelder–Mead optimization. The optimal scaling factors are found to closely follow a power-law relationship with respect to the indentation depth ratio for either direction. The minimum errors associated with the proposed surface topography extrapolation are shown in Fig. 4.6 rightmost plot, which are discussed in depth in Section 5.5. This upscaling strategy is essentially reducing the mesh resolution, thus, leading to more simulation uncertainty. The level

of such uncertainty and whether it will dominate the uncertainty of the determined parameters are some of the questions this study aims to investigate.

#### 4.1.5 Comparison between simulation and experiment

Quantification of the deviation between a measured and simulated indentation response follows the same strategy as outlined in Chakraborty and Eisenlohr [19], with a few adjustments. The topographic mismatch  $\epsilon_{\text{topo}}$  only considers areas that show pile-ups, *i. e.*, any negative elevation values are ignored. Moreover, two topography maps are radially shifted relative to each other until the global minimum of  $\epsilon_{\text{topo}}$  is identified. The errors between pairs of topographies and pairs (*A* and *B*) of load–depth (LD) curves,

$$\epsilon_{\text{topo}} = 2 \frac{\int |z_A - z_B| dA}{\int |z_A + z_B| dA} \quad \text{and} \quad \epsilon_{\text{LD}} = 2 \frac{\int |L_A - L_B| dD}{\int |L_A + L_B| dD}, \quad (4.10)$$

with  $z$  the surface elevation,  $L$  the indentation load, and  $D$  the indentation depth, are combined with equal weights, such that the total mismatch between two indentation responses results as

$$\epsilon = \frac{1}{2} \left( \epsilon_{\text{topo}} + \epsilon_{\text{LD}} \right). \quad (4.11)$$

#### 4.1.6 Single orientation approach

Zambaldi et al. [136] were among the first to consider both measured load–depth and surface topography to optimize constitutive parameters based upon distinct single-crystal indentations into *two* grains. In an assessment of CRSS sensitivity relying on synthetic data, Chakraborty and Eisenlohr [19] found that choosing *only one* indentation in any crystallography orientation is sufficient for IIA to determine CRSS values for cubic crystals. Since indentation simulation is generally costly, computational efforts can be reduced by considering only a single indentation in the optimization process. In a continuous effort to explore a complicated crystal lattice, Chakraborty et al. [21] demonstrated that the single approach also works for hexagonal (Ti) crystals when the selected indentation orientation is a “good” one that has a relatively high sensitivity to every slip

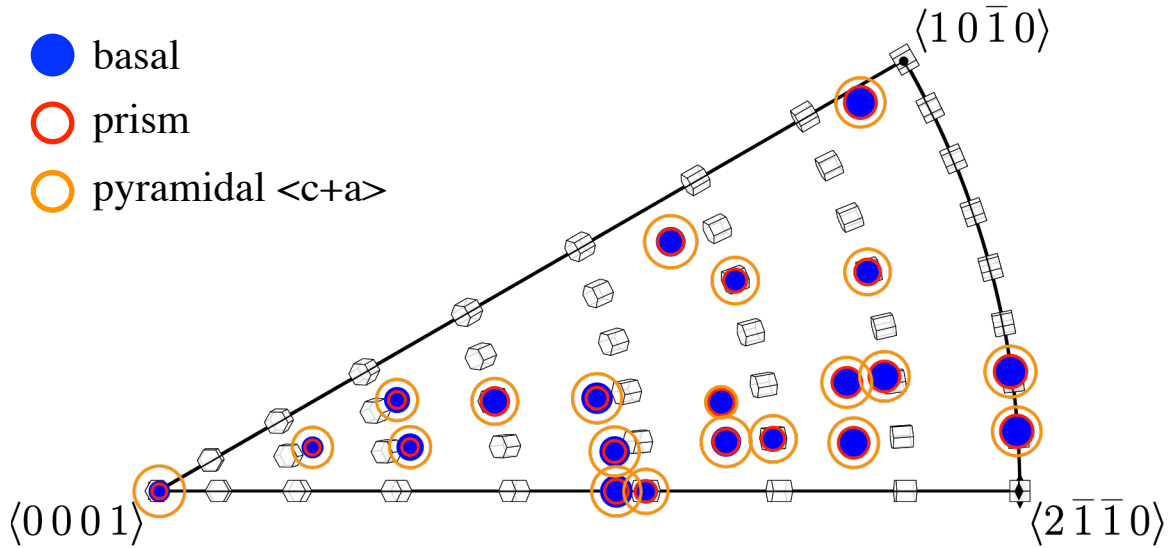


Figure 4.7: Average sensitivity of CRSS value of basal, prism, and pyramidal  $\langle c+a \rangle$  system at different crystallographic orientations [21].

system. Figure 4.7 shows the average sensitivity at different crystallographic orientations with respect to individual slip systems. Larger circles represent higher sensitivity. They proposed that the orientation should be chosen from regions where circles of all three colors are big (orientations away from  $\{0001\}$ ).

To test the single orientation approach for hexagonal crystals, Chakraborty et al. [21] used two sets of CRSS values (different ratios) of basal, prism, and pyramidal  $\langle c+a \rangle$  to create synthetic indentations for five sensitive orientations and one insensitive orientation. Figure 4.8 presents the optimal CRSS values based upon these synthetic data. The sensitive orientations produce correct CRSS values whereas the insensitive ones generate wrong results. Therefore, a way proposed by the authors to find credible CRSS values is to incrementally collect results from highly sensitive orientations until the median CRSS values stabilize.

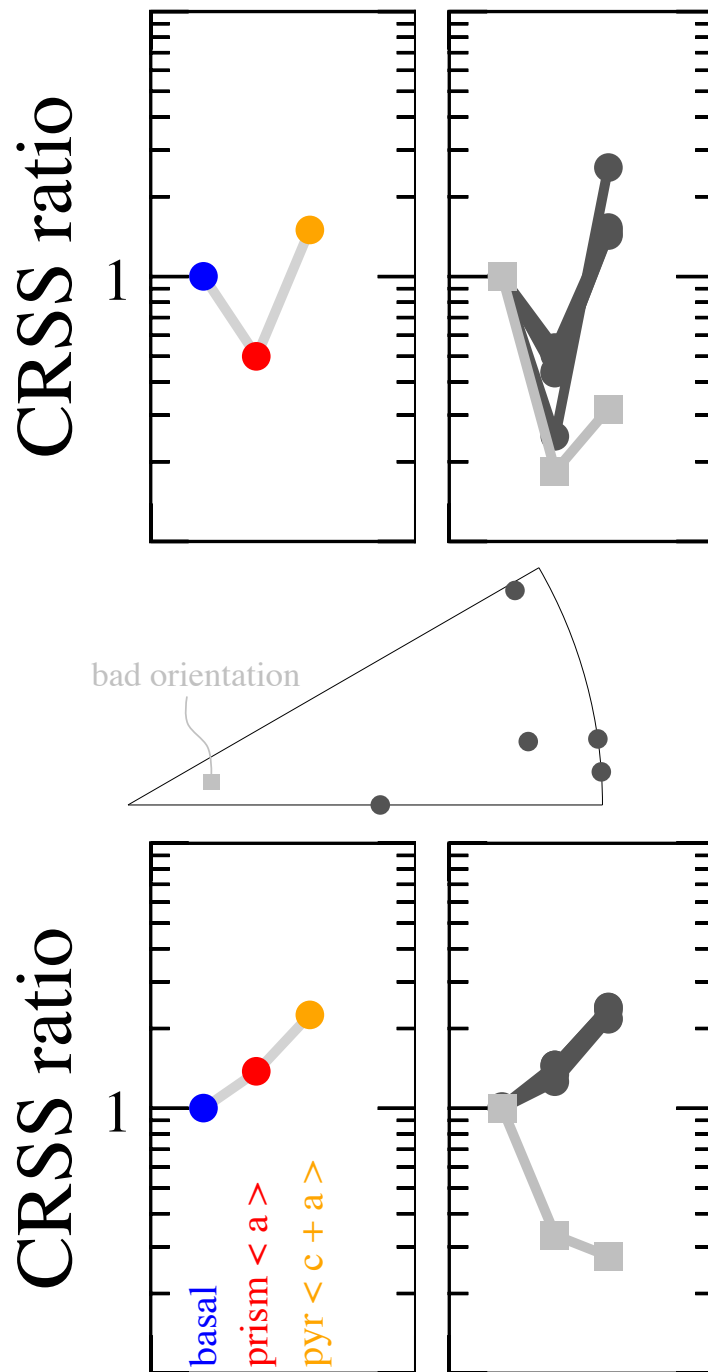


Figure 4.8: Reproducibility evaluation of IIA [21] based on two sets of synthetic CRSS values (left column). Right column presents the determined CRSS values using the synthetic indentation responses at 5 sensitive orientations (dark) and 1 insensitive orientation (light) .



#### 4.1.7 Relationship between the total indentation mismatch and CRSS uncertainty

Understanding the relationship between parameters and the total mismatch between load-depth curves (LD) and surface topography (topo) enables predicting the uncertainty of the determined parameters before performing the optimization, thus, guiding experiment preparation and simulation setups. This section aims at quantifying the change in simulated surface topography or load-depth curve response as a result of a change in each individual slip resistance/CRSS (simulation input). As local sensitivity can reflect subtle changes that are often observed in the last steps of CRSS optimization, a short-range sensitivity calculation is proposed below,

$$SST_{LD/topo} = \frac{\left| \varepsilon_{LD/topo}^+ \right| + \left| \varepsilon_{LD/topo}^- \right|}{\left| \ln \frac{CRSS_{neighbor}^+}{CRSS_{base}} \right| + \left| \ln \frac{CRSS_{neighbor}^-}{CRSS_{base}} \right|} \quad (4.12)$$

,where  $CRSS_{base}$  is the base slip resistance,  $CRSS_{neighbor}^+ = (1 + 0.1) CRSS_{base}$  and  $CRSS_{neighbor}^- = (1 - 0.1) CRSS_{base}$ .

27 combinations of basal, prism, and pyramidal  $\langle c + a \rangle$  slip resistances (basal = [30, 60, 120], prism = [20, 40, 80], pyrc+a = [90, 180, 360] MPa) were used as base parameters to form a 3-dimensional parameter domain. Figure 4.9 shows  $SST_{LD/topo}$  for basal, prism,  $\langle c + a \rangle$  systems for orientation 8 in the IPF triangle. The Larger ball represents a larger  $SST_{LD/topo}$  for the parameter set. Basal and prism slip have roughly the same magnitude of sensitivity (their balls are roughly the same sizes), and pyramidal  $\langle c + a \rangle$  slip show almost zero sensitivity (barely observable) for either load-displacement curve or surface topography. Pyramidal  $\langle c + a \rangle$  slip is considered the most difficult slip system in Ti alloys. It usually does not contribute to the deformation responses; thus, its sensitivity is poor. This study also shows the CRSS values have similar sensitivity between both responses (load-displacement curves or surface topography), which motivates the usage of equal weight for  $\varepsilon_{LD}$  and  $\varepsilon_{topo}$  to calculate the total mismatch between simulation and measurement by Eq. (4.11).

The average results from Fig. 4.9 establish  $\overline{SST_{LD/topo}} \approx 0.3$ .

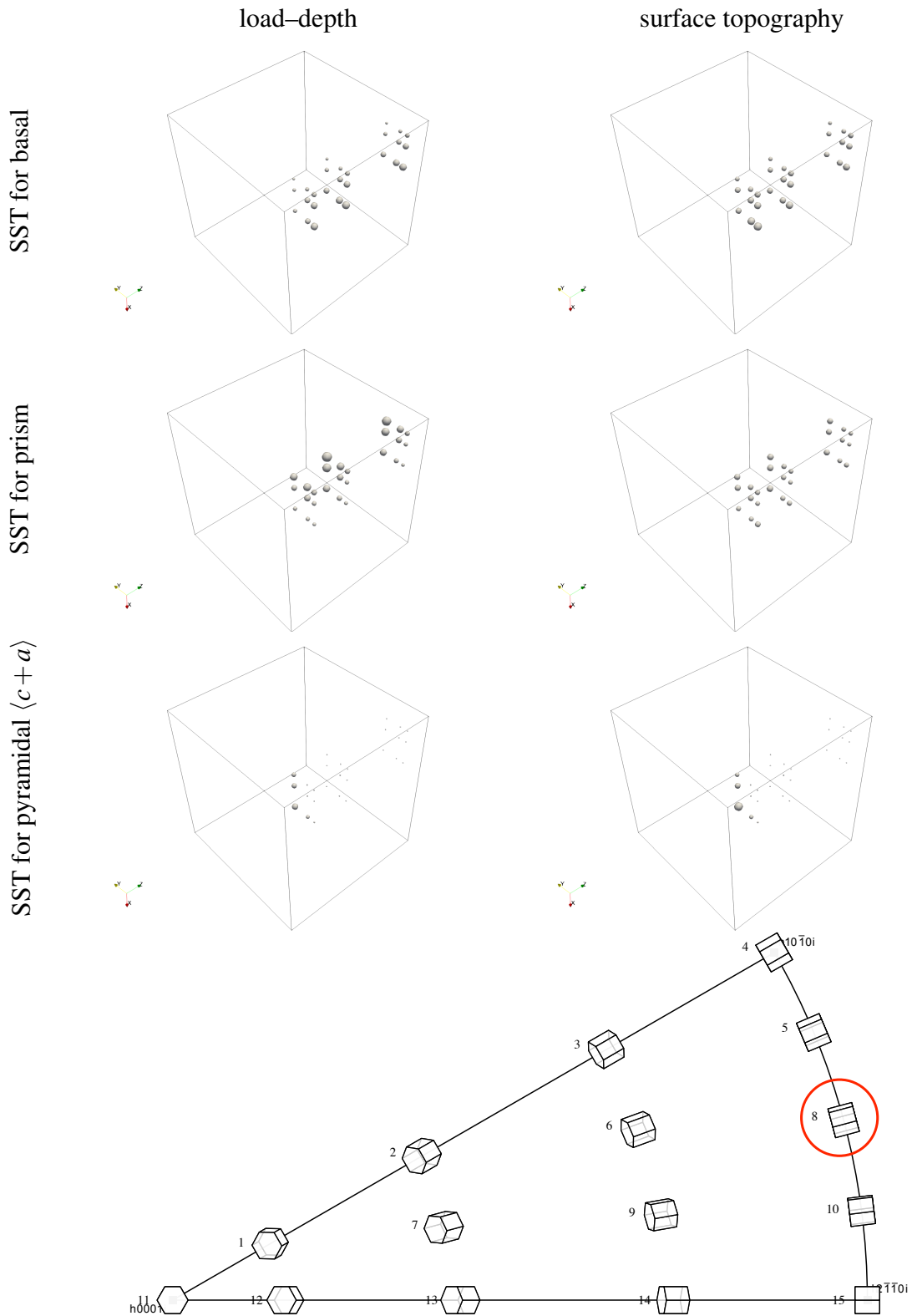


Figure 4.9: Short-range sensitivity (in a cubic parameter domain consists 27 parameter sets, the x, y, and z-axis indicate the CRSS ranges for basal, prism, and pyramidal  $\langle c+a \rangle$  respectively) of load-displacement in left column and surface topography in right column for orientation 8 (highlighted in red circle) in the IPF triangle.

## 4.2 Evaluation of slip transfer metrics with artificial neural network (ANN)

To extend the reported analysis of slip transfer data [9, 2] beyond the 2-D limitation, this study adopts a machine learning analysis, *i.e.*, artificial neural networks (ANN), that is good at solving hierarchical problems and dealing with data of high dimensions [109].

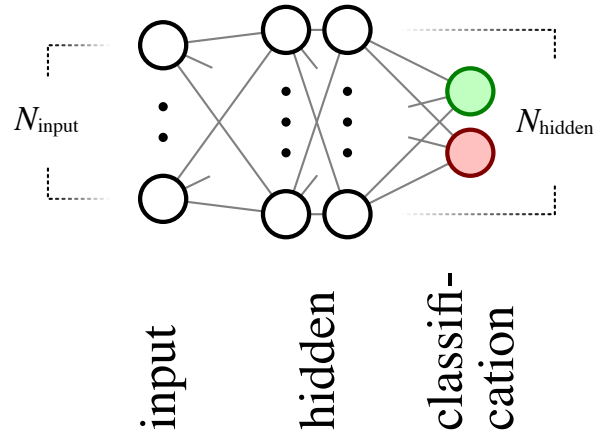


Figure 4.10: Architecture of the artificial neural network used for binary classification (green, red) with  $N_{\text{input}}$  nodes in the input layer and  $N_{\text{hidden}}$  nodes in each of the two hidden layers.

ANN is essentially a guided nonlinear mapping of input data to the output data through multiple layers of neurons (or nodes, see circles in Fig. 4.10), which mimics the structure of brains.

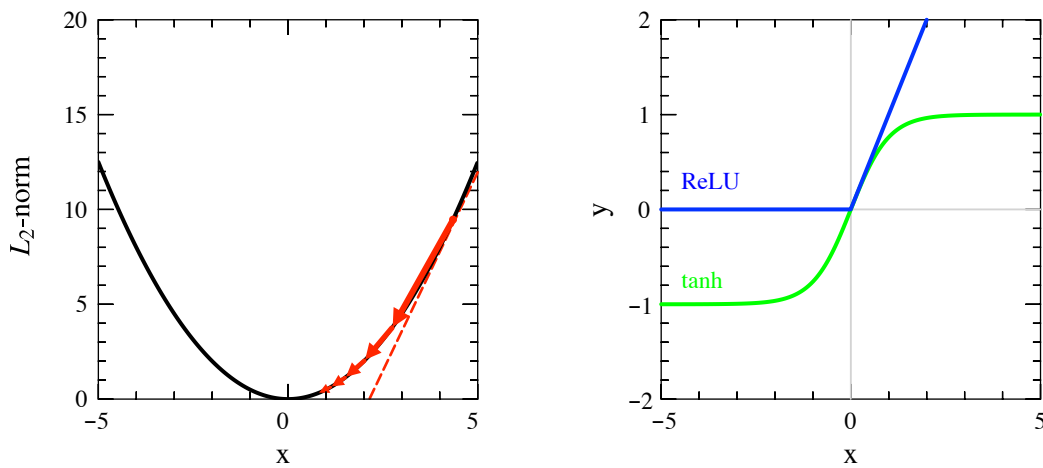


Figure 4.11: Left: gradient descent optimization for  $L_2$ -norm as loss function. Right: rectified linear unit (ReLU) and hyperbolic tangent (tanh) are two commonly used activation functions in ANN.

Classification is made based upon data in the output layer, *e.g.*, the probability of each class. Each node in ANN represents a linear operation followed by a nonlinear operation using an activation function. The two most commonly used activation functions are rectified linear unit (ReLU) and hyperbolic tangent (tanh) functions (Fig. 4.11). One approach to establishing meaningful parameters for individual linear operations (in each layer) is through an iterative optimization process based on informed data (also labeled or training data). This is called supervised learning. A popular optimization strategy is to find the minimum value of a convex loss function, *i.e.*, a formula ( $L_2$ -norm in this study) to calculate the total deviation between predictions and real values, by gradient descent (Fig. 4.11 left). For each iteration, the parameters are slowly (a small learning rate is usually adopted to avoid overshooting) updated by feedforward and backpropagation processes, which is explained in a simple (one hidden layer) ANN example below.

Assume the input layer has  $p$  features (dimension of input data or slip transfer metrics in this study),  $x_1, x_2, \dots, x_p$ , for binary classification (two output nodes). The feedforward process goes as follows.

- In the (first) hidden layer, linear operations are given by,

$$z_1 = xW_1 + b_1,$$

where  $W_1 \in \mathbb{R}^{p \times N_1}$  and  $b_1 \in \mathbb{R}^{N_1}$  are the parameter matrix,  $N_1$  is number of neurons in this hidden layer,  $z_1 \in \mathbb{R}^{N_1}$ . Hyperbolic tangent tanh is used as activation function to include nonlinearity.

$$f_1 = \tanh(z_1),$$

with  $f_1 \in \mathbb{R}^{N_1}$  the result vector that goes to the nodes in next layer.

- Output layer uses one-hot-encoder<sup>1</sup> to describe classification results.

$$z_2 = f_1W_2 + b_2,$$

with  $W_2 \in \mathbb{R}^{N_1 \times 2}$ ,  $b_2 \in \mathbb{R}^2$ ,  $z_2 \in \mathbb{R}^2$ .

---

<sup>1</sup>Use 1 to specify which category and 0s as other entries in a vector that has length of number of categories.

- Softmax function is used to get probability for each category/entry in the  $z_2$  vector after the one-hot-encoder conversion,

$$\hat{y} = \text{softmax}(z_2), \quad \text{softmax}(z)_j = \frac{\exp(z_j)}{\sum_k \exp(z_k)},$$

where  $j$  means the  $j$ -th category, and  $\sum_k \exp(z_k)$  sums probability of all categories.

$L_2$ -norm is used as loss function:  $L = \sum_j \frac{1}{2}(\hat{y}_j - y_j)^2$ , with  $y_j$  the true category value (during the training process) in the one-hot-encoder form. Backpropagation process updates each parameter with the corresponding loss function derivative (with respect to the parameter). Since the value in each node is the convolution of the operations from previous layers, the derivatives must be calculated by a chain rule.

- Applying chain rule

$$\frac{\partial L}{\partial W_2} = \frac{\partial L}{\partial \hat{y}} \cdot \frac{\partial \hat{y}}{\partial z_2} \cdot \frac{\partial z_2}{\partial W_2} = (\hat{y} - y) \times 1 \times f_1 = f_1^T (\hat{y} - y)$$

$$\frac{\partial L}{\partial b_2} = \frac{\partial L}{\partial \hat{y}} \cdot \frac{\partial \hat{y}}{\partial z_2} \cdot \frac{\partial z_2}{\partial b_2} = \hat{y} - y$$

$$\frac{\partial L}{\partial W_1} = \frac{\partial L}{\partial \hat{y}} \cdot \frac{\partial \hat{y}}{\partial z_2} \cdot \frac{\partial z_2}{\partial f_1} \cdot \frac{\partial f_1}{\partial z_1} \cdot \frac{\partial z_1}{\partial W_1} = x^T \left[ (1 - f_1^2) (\hat{y} - y) W_2^T \right]$$

$$\frac{\partial L}{\partial b_1} = \frac{\partial L}{\partial \hat{y}} \cdot \frac{\partial \hat{y}}{\partial z_2} \cdot \frac{\partial z_2}{\partial f_1} \cdot \frac{\partial f_1}{\partial z_1} \cdot \frac{\partial z_1}{\partial b_1} = (1 - f_1^2) (\hat{y} - y) W_2^T$$

- Update parameters in each layer by a small coefficient  $\alpha_{lr}$  (learning rate),

$$W_1, b_1, W_2, b_2 += \alpha_{lr} \times \frac{\partial L}{\partial W_1}, \frac{\partial L}{\partial b_1}, \frac{\partial L}{\partial W_2}, \frac{\partial L}{\partial b_2}$$

More layers can be added to the above formulations, mainly by modifying the chain rule in the backpropagation. To date, software like TensorFlow and Keras hide these detailed implementations in the backend and allow users to easily build and adjust (customized) networks by tuning specification parameters.

The training process can be stopped at a small loss function value or after a certain number of iterations. Then the trained ANN can be used for classifying new (or unlabeled) data. To evaluation the performance of the trained ANN, another set of labeled data is used to calculate

the classification accuracy, *e.g.*, the fraction of correct classifications. The training and testing processes are expected to repeat until stable classification accuracy is reached. If the dataset is small, training and testing data (non-overlapping) are usually obtained from a portion of the whole dataset by a random sampling strategy.

ANN and its variations can be used to deal with complicated hierarchical problems such as text mining, image recognition as well as segmentation (convolutional neural network), and speech recognition (recurrent neural network) [109]. Although ANN has been used in some research studies related to metallurgy, *e.g.*, processing microstructure images [27] and predicting materials properties from compositions [25, 48], applications of machine learning techniques are generally not widespread in materials science research because these researches typically do not deal with the massive amount of data<sup>2</sup>. However, with advances in characterization techniques and computational capability, an increasing amount of data will be generated in materials science research, and there will be a growing need to use these tools.

---

<sup>2</sup>For small dataset, simple (*typically* one or two hidden layer) ANN should be used to avoid overfitting or memorizing the training data.

### 4.3 Transformation between hexagonal $\alpha$ and body-centered cubic $\beta$ crystals

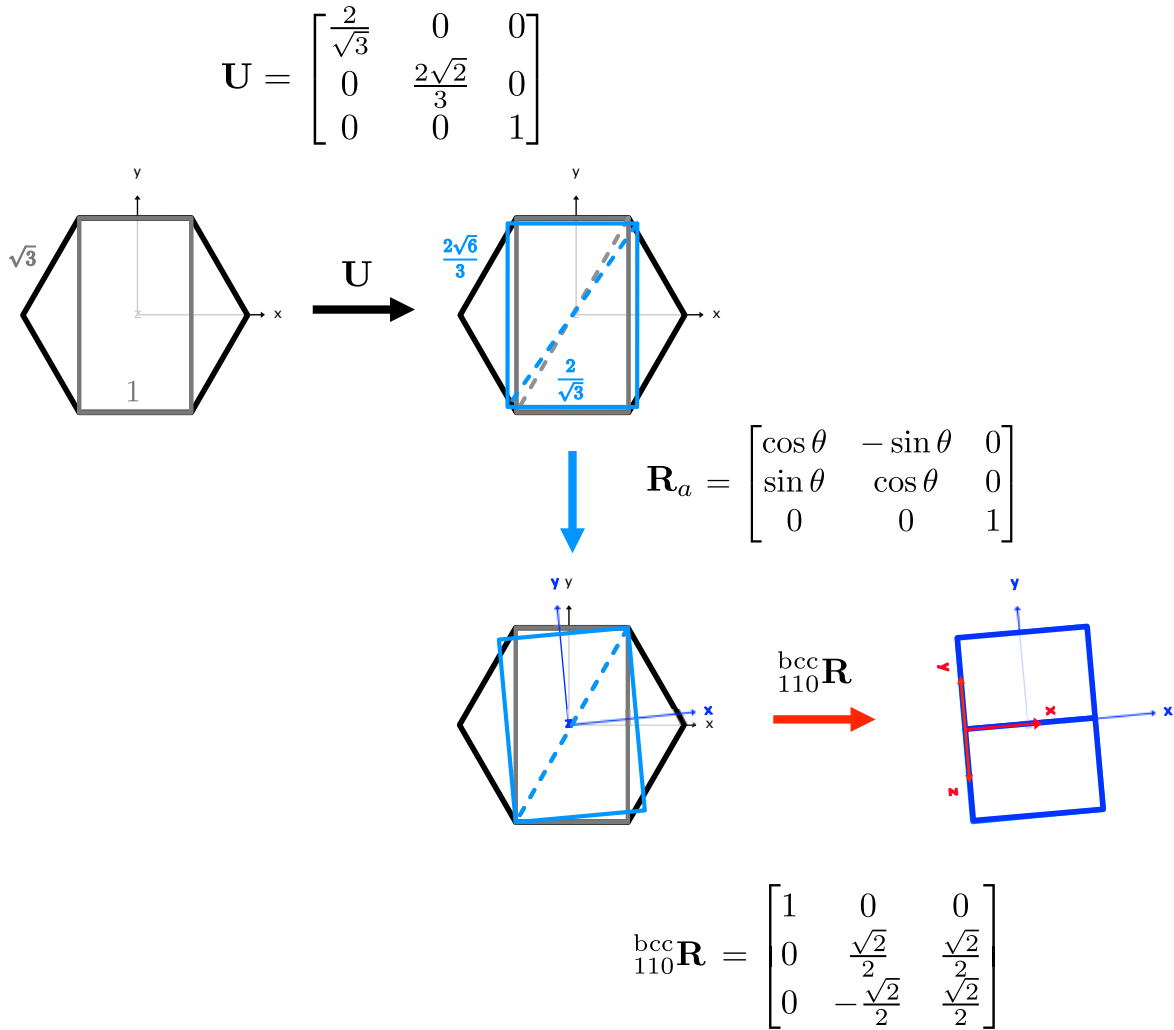


Figure 4.12: Schematics of hcp lattice (Euler angles  $\phi_1 = 0^\circ, \Phi = 0^\circ, \phi_2 = 0^\circ$ ) transforming to bcc lattice (one scenario,  $\theta = \pm 5.26^\circ$ ).

The transformation from close-packed hexagonal (hcp) to body-centered cubic (bcc) crystal structure is accommodated by modulating atoms on the basal plane to reach the stacking of bcc  $\{110\}$  planes such that the original basal plane transforms to one of the  $\{110\}$  planes in bcc

structure. The height of the hexagonal cell remains constant, and each of the three intermediate atoms rearranges its position slightly to become the center atom in the bcc unit cell. This process comprises a  $5.26^\circ$  rotation (either clockwise or counterclockwise)  $\mathbf{R}_a/\mathbf{R}_b$  ( $a, b$  means the rotation in the 1st and 2nd step, respectively) around the basal plane normal, *i.e.*,  $\langle c \rangle$  direction, to align the long diagonal of the hexagon ( $\langle 2\bar{1}\bar{1}0 \rangle$  direction) with bcc  $\langle 111 \rangle$  direction, and a stretch of hcp  $\langle 1\bar{2}10 \rangle$  and a contraction along  $\langle 10\bar{1}0 \rangle$ , see Fig. 4.12. The transformation from bcc to hcp is a reversal of the above process. In contrast, there are six equivalent  $\{110\}$  planes to choose to form the new basal plane in the hcp unit cell according to bcc symmetries.

To demonstrate the approach to calculate the kinematics of such phase transformation, two specific calculations, *e.g.*, lattice orientation and deformation gradient (shape change) involving hcp-bcc-hcp phase transformation, are presented in this section.<sup>3</sup> The calculation of lattice orientation only involves frame rotations, whereas the transformation matrix calculation also requires shape change (stretches and contractions) besides frame rotations.

### 4.3.1 Orientation calculation

The orientation calculation in hcp-bcc-hcp transformation follows a series of rotational and frame transformations, which was first introduced by Humbert et al. [59].

- Convert original Euler angles<sup>4</sup> to the orientation matrix (lab to crystal frame),  $\mathbf{G}_{\text{lab}}^{\text{hex}}$ .
- Apply hexagonal symmetry operators (see Table .1) in the hexagonal frame  $\mathbf{S}_{\text{hex}}$ .
- Apply rotation  $\mathbf{R}_a$  around  $\langle c \rangle$  (clockwise “-” and counter clockwise “+”) to align the hcp  $\langle 2\bar{1}\bar{1}0 \rangle$  direction of the hcp basal plane with the corresponding bcc  $\langle 111 \rangle$  direction (bcc  $\{110\}$  plane diagonal), which essentially transforms the hexagonal frame to the bcc  $\{110\}$  plane frame.

---

<sup>3</sup>Since  $\alpha$  phase typically dominates the microstructure at ambient temperature, comparisons among different  $\alpha$  grains undergone hcp-bcc-hcp phase transformation are of great interest.

<sup>4</sup>Quaternions or any other conventions to represent crystal orientation in the lab frame.



- Convert from the bcc  $\{110\}$  plane frame to the default bcc frame,  ${}_{110}^{\text{bcc}}\mathbf{R}$ .
- Apply cubic symmetry operators  $\mathbf{S}_{\text{bcc}}$  (see Table .2) in the bcc frame.
- Convert from the bcc frame back to the bcc  $\{110\}$  plane frame,  ${}_{110}^{\text{bcc}}\mathbf{R}^{\text{T}}$  (equivalent to  ${}_{\text{bcc}}^{110}\mathbf{R}$ ).
- To start the bcc-hcp transformation, apply in-plane rotation  $\mathbf{R}_b$  to align the bcc  $\langle 111 \rangle$  direction with the hcp  $\langle 2\bar{1}\bar{1}0 \rangle$  direction, which essentially transforms the bcc  $\{110\}$  plane frame back to the hexagonal frame. The new orientation matrix  $\mathbf{G}^{\text{new}}$  expressed in the lab coordinates after the hcp-bcc-hcp transformation is calculated as follows.

$$\mathbf{G}^{\text{new}} := {}_{\text{lab}}^{\text{hex}}\mathbf{G}^{\text{T}} \mathbf{R}_b {}_{110}^{\text{bcc}}\mathbf{R}^{\text{T}} \mathbf{S}_{\text{bcc}} {}_{110}^{\text{bcc}}\mathbf{R} \mathbf{R}_a \mathbf{S}_{\text{hex}} {}_{\text{lab}}^{\text{hex}}\mathbf{G}$$

### 4.3.2 Deformation gradient calculation

A method to calculate the deformation gradient in the hcp-bcc-hcp phase transformation (similar to the orientation calculation) is proposed in this section, which will facilitate the implementation of such transformation into continuum models. The deformation gradient calculations are essentially doing two shape changes in the correct frames. The two steps are summarized as follows:

- hcp $\rightarrow$ bcc: the first shape change  $\mathbf{R}_a^{\text{T}}\mathbf{U}$  is composed of an active plane rotation  $\mathbf{R}_a^{\text{T}}$  and an active plane stretch  $\mathbf{U}$  to transform from the hcp basal plane to the bcc  $\{110\}$  plane in the standard hexagonal frame  $\mathbf{R}_{\text{fr1}}$ .

$$\mathbf{F}_1 := \underbrace{{}_{\text{lab}}^{\text{hex}}\mathbf{G}^{\text{T}} \mathbf{S}_{\text{hex}}^{\text{T}} \mathbf{R}_a^{\text{T}} \mathbf{U}}_{\mathbf{R}_{\text{fr1}}^{\text{T}}} \underbrace{\mathbf{S}_{\text{hex}} {}_{\text{lab}}^{\text{hex}}\mathbf{G}}_{\mathbf{R}_{\text{fr1}}} \quad (4.13)$$

- bcc $\rightarrow$ hcp: the second shape change  $\mathbf{R}_b^{\text{T}}\mathbf{U}^{-1}$  includes an active plane rotation  $\mathbf{R}_b^{\text{T}}$  and an operation to undo the stretch that transforms the bcc  $\{110\}$  plane back to the hcp basal plane shape in the transformed bcc frame  $\mathbf{R}_{\text{fr2}}$ .

$$\mathbf{F}_2 := \underbrace{{}_{\text{lab}}^{\text{hex}}\mathbf{G}^{\text{T}} \mathbf{S}_{\text{hex}}^{\text{T}} \mathbf{R}_a^{\text{T}} {}_{110}^{\text{bcc}}\mathbf{R}^{\text{T}} \mathbf{S}_{\text{bcc}}^{\text{T}} {}_{\text{bcc}}^{110}\mathbf{R}^{\text{T}}}_{\mathbf{R}_{\text{fr2}}^{\text{T}}} \mathbf{R}_b^{\text{T}} \mathbf{U}^{-1} \underbrace{{}_{\text{bcc}}^{110}\mathbf{R} \mathbf{S}_{\text{bcc}} {}_{110}^{\text{bcc}}\mathbf{R} \mathbf{R}_a \mathbf{S}_{\text{hex}} {}_{\text{lab}}^{\text{hex}}\mathbf{G}}_{\mathbf{R}_{\text{fr2}}} \quad (4.14)$$

The combined calculations of the deformation gradient  $\mathbf{F}$  are as follows.

$$\mathbf{F} := \mathbf{F}_2 \mathbf{F}_1 \quad (4.15)$$

$\mathbf{F}$  has different values with a different initial orientation and by applying different symmetry operators. Note the rotation matrix  $\mathbf{R}_a/\mathbf{R}_b$  and the shape change operator  $\mathbf{U}$  in Fig. 4.12 are determined based on the hcp crystal. For alloys with varying alloying compositions, a specific  $c/a$  ratio should be applied to ensure more accurate orientation and deformation gradient calculations.

### 4.3.3 Variants in hcp–bcc ( $\alpha$ – $\beta$ ) phase transformation

**$\alpha \rightarrow \beta \rightarrow \alpha$  transformation** There are 6 equivalent  $\{110\}$  planes (symmetry) in bcc and 4 possible combinations of rotations in the hex-bcc-hex transformation. However, for the symmetry that corresponds to invariant transformation (identity matrix), there are only 3 resulting variants because the combination of a positive rotation in the first step and negative rotation in the second step would be equal to the combination of the two rotations in a reversed order. Therefore, there are a total of 57 distinct variants of the hcp-bcc-hcp transformation. This also means there are theoretically 57 distinct variants of hcp crystals resulting from bcc parent crystals ( $\beta$ -Ti) of the same orientation.

Table 4.1: Statistics of random distribution of variants (1152 explorations in total) from a common initial hcp lattice in the hcp-bcc-hcp transformation.

misorientation angle ( $^\circ$ )	counts	fraction
0	96	1/12
10.53	96	1/2
60	192	1/6
60.83	384	1/3
63.26	192	1/6
90	192	1/6

The misorientation angle between each variant and the parent/original hcp orientation and probability of observing the angle is shown in Table 4.1. Only 6 disorientation angles ( $0^\circ$ ,  $10.53^\circ$ ,  $60^\circ$ ,

60.83°, 63.26° and 90°) between the parent hcp crystal and the transformed hcp crystal are possible. This is consistent with the report by Karthikeyan et al. [63] that shows all of the possible misorientations between two random transformed hex crystals from the same bcc parent crystal based on a different approach.

Misorientation angles of 60° and 63.26° are only possible by opposite sign rotations in the hcp-bcc and bcc-hcp transformation steps, while a misorientation angle of 60.83° is only possible by the same sign rotations in those two transformation steps. Table 4.2 summarizes the orientations and shape changes (leftmost cubes) of these 57 variants. The top three rows show the transformations with the unit symmetry operation in both steps, resulting in an invariant case and essentially pure rotations in two different directions.

Table 4.2 : List of 57 possible variants in hcp-bcc-hcp phase transformation.  $b_i$  is the bcc symmetry operator in Table .2, and  $h_i$  is the hexagonal symmetry operator in Table .1. “+” and “-” denote clockwise and counterclockwise rotation, respectively. The cubes in the rightmost column show the transformed cubic volume (the original shape is the same as the first cube).

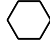

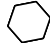

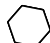









hex	$R_a$	bcc	$R_b$	$\Delta\theta$ (°)	new orientation	shape
	+		-	0.00		
$h_1$	+	$b_1$	+	10.53		
	-		-	10.53		
$h_1$	+	$b_2$	-	90.00		
	+		+	90.00		
	-		-	90.00		
	-		+	90.00		

Table 4.2 (cont'd)









































hex	$R_a$	bcc	$R_b$	$\Delta\theta$ (°)	new orientation	shape
h <sub>1</sub>	+	b <sub>3</sub>	-	60.00		
	+		+	60.83		
	-		-	60.83		
	-		+	63.26		
h <sub>1</sub>	+	b <sub>4</sub>	-	63.26		
	+		+	60.83		
	-		-	60.83		
	-		+	60.00		
h <sub>1</sub>	+	b <sub>9</sub>	-	60.00		
	+		+	60.83		
	-		-	60.83		
	-		+	63.26		
h <sub>1</sub>	+	b <sub>10</sub>	-	63.26		
	+		+	60.83		
	-		-	60.83		
	-		+	60.00		
h <sub>2</sub>	+	b <sub>2</sub>	-	90.00		
	+		+	90.00		
	-		-	90.00		
	-		+	90.00		

Table 4.2 (cont'd)















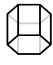























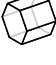



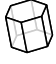











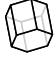
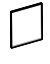




hex	$R_a$	bcc	$R_b$	$\Delta\theta$ ( $^\circ$ )	new orientation	shape
h <sub>2</sub>	+	b <sub>3</sub>	-	60.00		
	+		+	60.83		
	-		-	60.83		
	-		+	63.26		
h <sub>2</sub>	+	b <sub>4</sub>	-	63.26		
	+		+	60.83		
	-		-	60.83		
h <sub>2</sub>	+	b <sub>9</sub>	-	60.00		
	+		+	60.83		
	-		-	60.83		
	-		+	63.26		
h <sub>2</sub>	+	b <sub>10</sub>	-	63.26		
	+		+	60.83		
	-		-	60.83		
h <sub>3</sub>	+	b <sub>2</sub>	-	90.00		
	+		+	90.00		
	-		-	90.00		
	-		+	90.00		

Table 4.2 (cont'd)

hex	$R_a$	bcc	$R_b$	$\Delta\theta$ (°)	new orientation	shape
h <sub>3</sub>	+	b <sub>3</sub>	+	60.83		
	-		-	60.83		
	-		+	63.26		
h <sub>3</sub>	+	b <sub>4</sub>	-	63.26		
	+		+	60.83		
	-		-	60.83		
h <sub>3</sub>	+	b <sub>9</sub>	+	60.83		
	-		-	60.83		
	-		+	63.26		
h <sub>3</sub>	+	b <sub>10</sub>	-	63.26		
	+		+	60.83		
	-		-	60.83		

$\beta \rightarrow \alpha \rightarrow \beta$  **transformation** Similarly, the misorientation angle between  $\beta$  variants in the  $\beta \rightarrow \alpha \rightarrow \beta$  transformation can be calculated and summarized in Table 4.3.

Table 4.3: Misorientation angle between two  $\beta$  variants from the same parent alpha grain.

misorientation angle (°)
0
10.53
60.00
60.00
60.00
49.47

## CHAPTER 5

### QUANTIFYING UNCERTAINTIES OF CRSS VALUES OF HEXAGONAL TI ALLOYS DERIVED FROM NANO-INDENTATION

This chapter is adapted from a manuscript by Zhao et al. 2021.

#### 5.1 Introduction and motivation

As discussed in Section 3.1, the reported CRSS values for CP-Ti varies with different methods, which calls for evaluations of the intrinsic uncertainty associated with each method. Based on synthetic reference data, Chakraborty et al. [21] comprehensively analyzed the accuracy and precision of inverse indentation analysis (IIA). They found IIA produces consistent CRSS values that are close to the true values used to create the synthetic reference with selective orientations having high sensitivity to all three considered slip systems, *i. e.*, basal, prism, and pyramidal  $\langle c + a \rangle$  slip. The goal of the present contribution is to more deeply assess the IIA method using measured (instead of synthetic) topography and load–depth data sets that were acquired for three different Ti alloys at ambient and elevated temperature.

#### 5.2 Materials and Methods

**Materials** Polycrystalline samples of commercially pure Ti (CP-Ti), Ti-3Al-2.5V, and Ti-6Al-4V (with compositions in wt%) were cut from larger pieces. The CP-Ti sample had an average grain size of 60  $\mu\text{m}$  as determined by the line intercept method. The two alloys were annealed at 1173 K (900 °C) for 14 h to homogenize the microstructures, which resulted in grain sizes of 10  $\mu\text{m}$ .

**Experiment procedures** Following mechanical grinding with SiC paper down to grit 4000, sample surfaces were mechanically polished with diamond paste sizes down to 0.10  $\mu\text{m}$  before a final polishing step using a 95 % / 5 % mixture of 0.04  $\mu\text{m}$  OPS suspension (Buehler) and hydrogen peroxide to reach a surface quality that gives high indexing quality for electron backscattered diffrac-



tion (EBSD, Tescan MIRA 3). Nanoindentations (NanoTest Alpha, Micro Materials Ltd.) using a conospherical diamond tip with a cone angle of  $90^\circ$  and a tip radius of  $1\ \mu\text{m}$  were placed on the polished surfaces in square grids that each covers an area containing tens of grains. To consistently obtain indentation depths in the range of  $0.30\ \mu\text{m}$  to  $0.60\ \mu\text{m}$ , the maximum load was  $10\ \text{mN}$  for all three alloys at ambient temperature and  $4\ \text{mN}$  ( $6\ \text{mN}$ ) for CP-Ti (Ti-6Al-4V) at  $523\ \text{K}$ .<sup>1</sup> In the ambient temperature indentations, the load was increased up to the prescribed maximum in  $10\ \text{s}$  followed by an immediate unload in  $2\ \text{s}$ . The high temperature indentations in CP-Ti and Ti-6Al-4V were carried out under flowing Argon, using the same loading and unloading times, but with an additional  $2\ \text{s}$  of dwell at maximum load. The resulting surface topographies were measured using atomic force microscopy (AFM, Bruker Veeco Icon) that typically mapped an area of  $10 \times 10\ \mu\text{m}^2$  at a resolution of  $256 \times 256$ . Figures 5.1 and 5.2 assemble the surface topographies and load–depth responses collected across the three alloys at ambient temperature and  $523\ \text{K}$ .

### 5.3 Indentation measurements

**Ambient temperature indentation measurements for Ti alloys** The indent surface topography was measured over a number of distinct orientations for CP-Ti, Ti-3Al-2.5V, and Ti-6Al-4V using atomic force microscopy (AFM). These indents are plotted on an inverse pole figure map (Fig. 5.1) of the indentation axis in a convention following Zambaldi and Raabe [135], which is an invariant presentation of equivalent relations of indentation axis and crystallographic orientation.

Some general trends are observed for all Ti alloys. Within each material, the surface topography possesses a nominally two-fold symmetry for most selected orientations and the maximum elevation becomes larger toward the outer perimeter. This feature is most likely an indication of dominant prismatic slip during deformation in these orientations. However, a few orientations close to c-axis show more circular features, which suggest complicated deformation modes. Also, the maximum pile-ups elevation is much smaller for orientations close to the c-axis, indicating that these are harder orientations. These general trends may indicate CP-Ti, Ti-3Al-2.5V, and

---

<sup>1</sup>No elevated-temperature indentation was performed for Ti-3Al-2.5V.

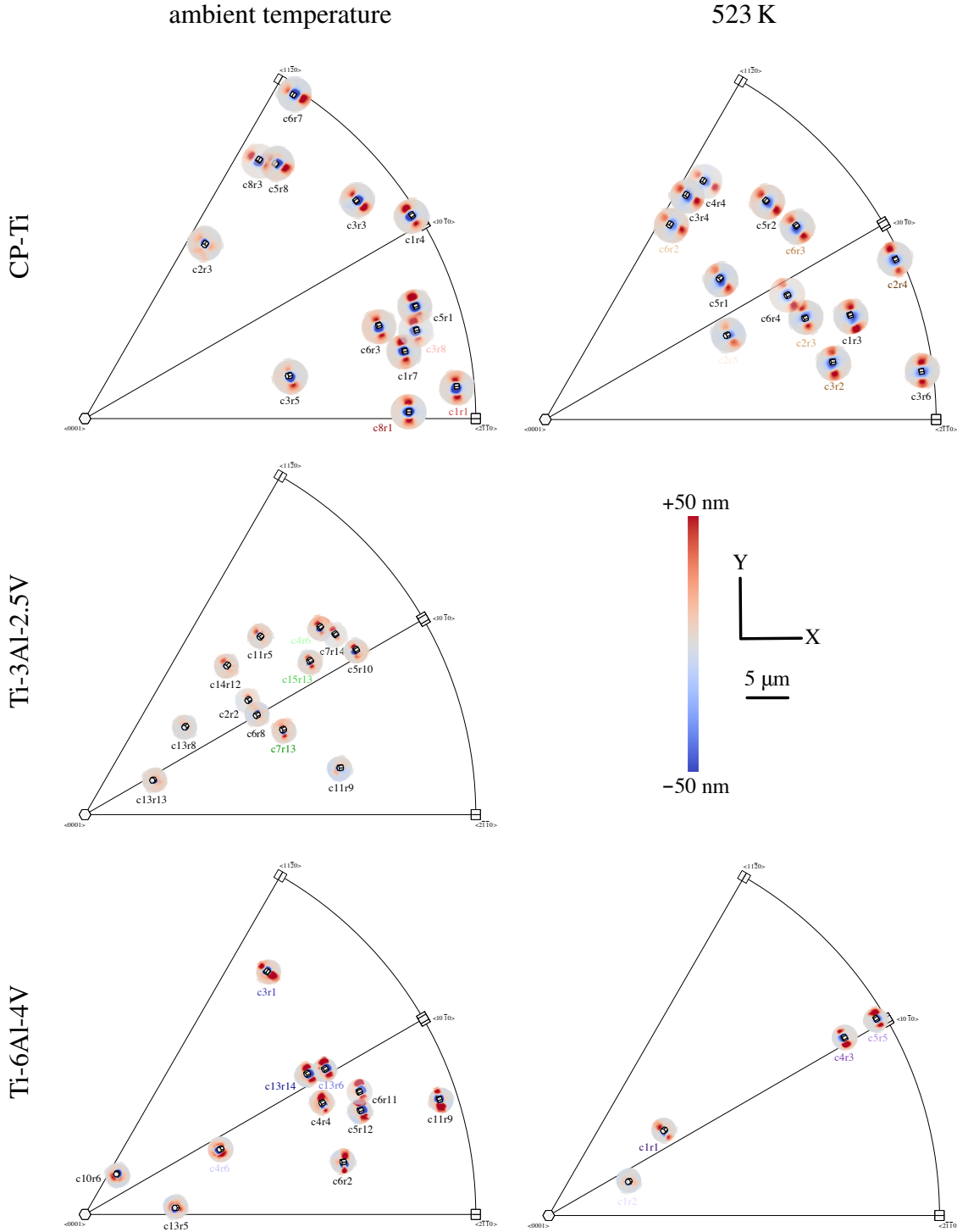


Figure 5.1: Surface topographies resulting from indentations at ambient temperature (left) and elevated temperature (right) for the three investigated Ti alloys (rows). Location of each topography on the inverse pole figure indicates the crystallographic indentation direction; in-plane rotation follows the convention of Zambaldi and Raabe [135]. For each material–temperature combination, all indents labeled in black were individually subjected to inverse indentation analysis to establish CRSS values of basal, prismatic, and pyramidal  $\langle c + a \rangle$  slip families.

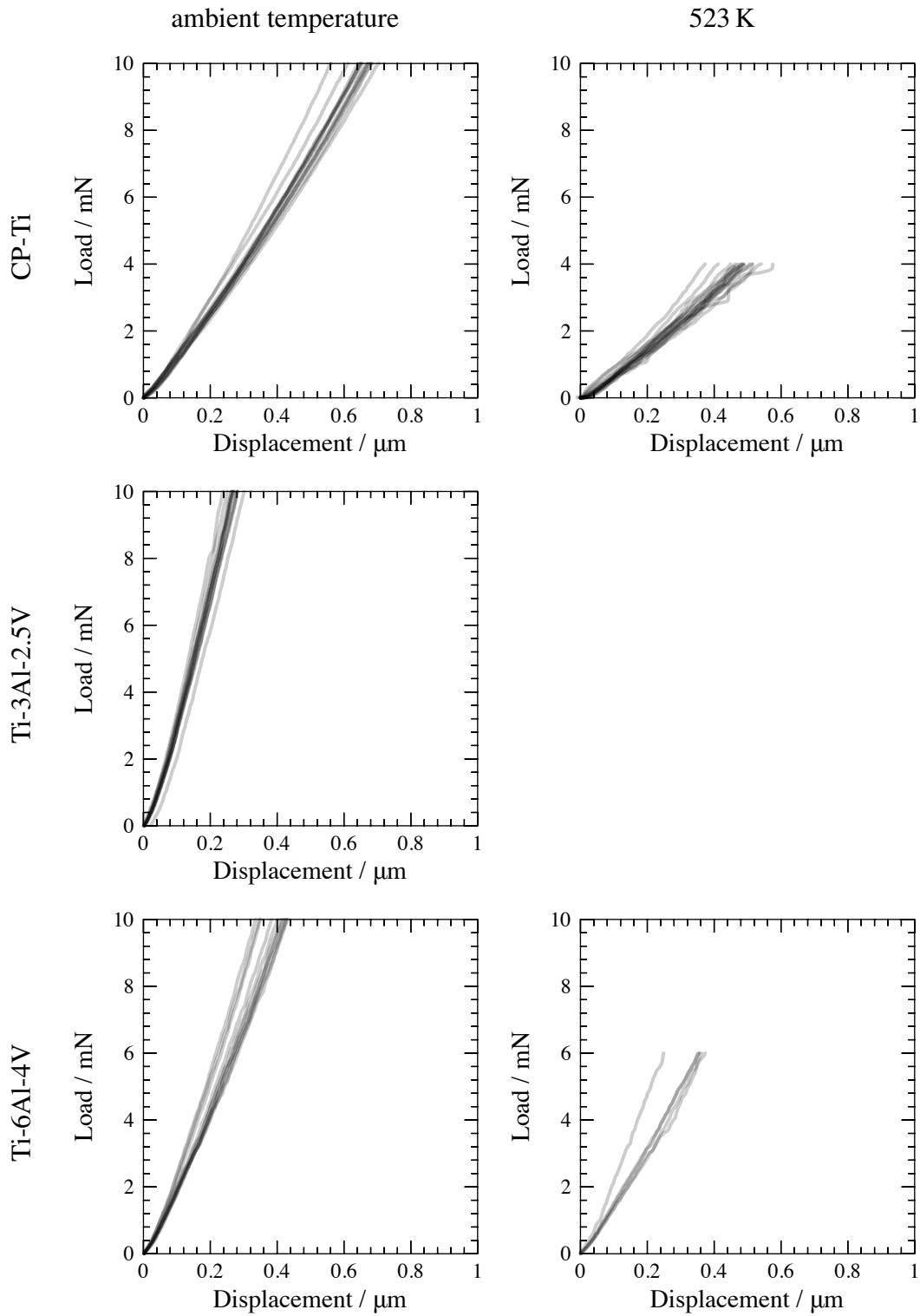


Figure 5.2: Increase of indenter force with depth up to maximum load (4, 6, or 10 mN) for all crystallographic indentation directions shown in Fig. 5.1.

Ti-6Al-4V are likely to share similar deformation modes for the corresponding crystallographic orientations, which means that the alloying elements may not strongly affect the slip mode for these alloys.

On the other hand, indents and their surface topographies are much smaller for Ti-3Al-2.5V and Ti-6Al-4V compared to CP-Ti even though the same loading conditions were used. This is a result of alloy strengthening.

The load-displacement data are plotted in Fig. 5.2. The CP-Ti and Ti-6Al-4V samples exhibit two groups—curves with steeper slopes are those harder orientations and the other group contains softer orientations (two-fold features). Interestingly, the Ti-3Al-2.5V sample does not show obvious slope separations.

**High temperature (HT) indentation measurements for CP-Ti and Ti-3Al-2.5V** The sizes of measured indentation surface topography are comparable to RT indents under a smaller indentation load (6 mN) as materials become softer at higher temperatures. These HT indents exhibit similar trends to RT indentation. This indicates that the deformation modes do not change when temperature is increased to 250 °C. The load-displacement curves show two groups reflecting hard and soft orientations, respectively.

## 5.4 Simulation and optimization set-ups

**Indentation simulation** Similar to prior work [19], the phenomenological power-law [98] implemented in the Düsseldorf Advanced Material Simulation Kit (DAMASK) [106] was used as crystal plasticity constitutive description and installed as a user subroutine within the finite element software ABAQUS 2017. Details about mesh discretization and phenomenological power-law model are introduced in Section 4.1.2.

As the numerical effort for each simulation grows substantially with increasing indentation depth, one possible strategy to reduce the computational effort is to terminate simulations at a relatively shallow depth and extrapolate their results to larger indentation depths, which would then be compared to the actually measured results. To test the viability of such an extrapolation

scheme, one deep (expensive) indentation simulation was performed. With this dataset, surface topographies at early simulation stages were scaled in radial direction by a factor  $f_r$  as well as normal to the surface by a factor  $f_z$  to minimize their deviation from simulation results at larger depths. The optimal values of  $f_r$  and  $f_z$  vary with the indentation depth ratio, *i.e.*, the ratio between the larger depth and the smaller depth from which the extrapolation was done, and are presented in the top left panel of Fig. 5.4 (other parts of the figure are discussed later). Within the range illustrated, both factors can be consistently approximated by a power law with exponents of 0.48 and 1.22, respectively.

In contrast to the viable extrapolation of the topography, there is no clear way to extrapolate the simulated load–depth response. Hence, the experimental load–depth response needs to be cropped in order to compare to the simulated load–depth response when the latter only reaches a smaller depth.

**Optimization of adjustable constitutive parameters** Following the same rationale as Chakraborty et al. [21], the constitutive parameters to be optimized are restricted to the initial slip resistance values  $\xi_0$  of basal, prismatic, and pyramidal  $\langle c + a \rangle$  slip. This choice results in a (computationally tractable) three-dimensional parameter space and encompasses the most sensitive parameters that determine the indentation response. All other constitutive parameters were taken from [136], assumed to be valid for all three alloys, and are listed in Table 5.1.

The optimization strategy is largely similar to the one used by Chakraborty et al. [21], *i.e.*, initial particle swarm optimization (PSO [32]) followed by a Nelder–Mead (N–M [91]) simplex search. Notable differences to this prior approach are: (i) the swarm is comprised of 20 instead of 10 particles, (ii) transition to N–M occurs after a maximum of 25 instead of 10 PSO iterations, (iii) the N–M simplex is constructed considering the four particles with highest fitness instead of four random particles. Contrary to the findings by Chakraborty et al. [21], in the present study neither the fitness nor the associated CRSS values changed significantly during subsequent N–M optimization but remained at similar levels as observed by the end of PSO.

Table 5.1: Constitutive parameters of the phenomenological power-law (see [106] for details) used in the indentation simulations as adopted from [136]. Sole values in a row reflect published data of CP-Ti but are used for all three materials, as differences are assumed to be trivial.

Parameter	Value			Unit
	CP-Ti	Ti-3Al-2.5V	Ti-6Al-4V	
$c/a$		1.59		
$C_{11}$		160		GPa
$C_{12}$		90		GPa
$C_{13}$		66		GPa
$C_{33}$		181.70		GPa
$C_{44}$		46.50		GPa
$\xi_0^{\text{basal}}$	0.01–0.5	0.01–1	0.01–1	GPa
$\xi_0^{\text{prism}}$	0.01–0.5	0.01–1	0.01–1	GPa
$\xi_0^{\text{pyr}\langle c+a \rangle}$	0.01–2	0.01–4	0.01–4	GPa
$\xi_\infty^{\text{basal}}$		0.57		GPa
$\xi_\infty^{\text{prism}}$		1.50		GPa
$\xi_\infty^{\text{pyr}\langle c+a \rangle}$		3.40		GPa
$h_0(298\text{ K})$		0.20		GPa
$h_0(523\text{ K})$		0.16		GPa
$q\xi\zeta$		1		
$a$		2		
$\dot{\gamma}_0$		0.00		$\text{s}^{-1}$
$n$		20		

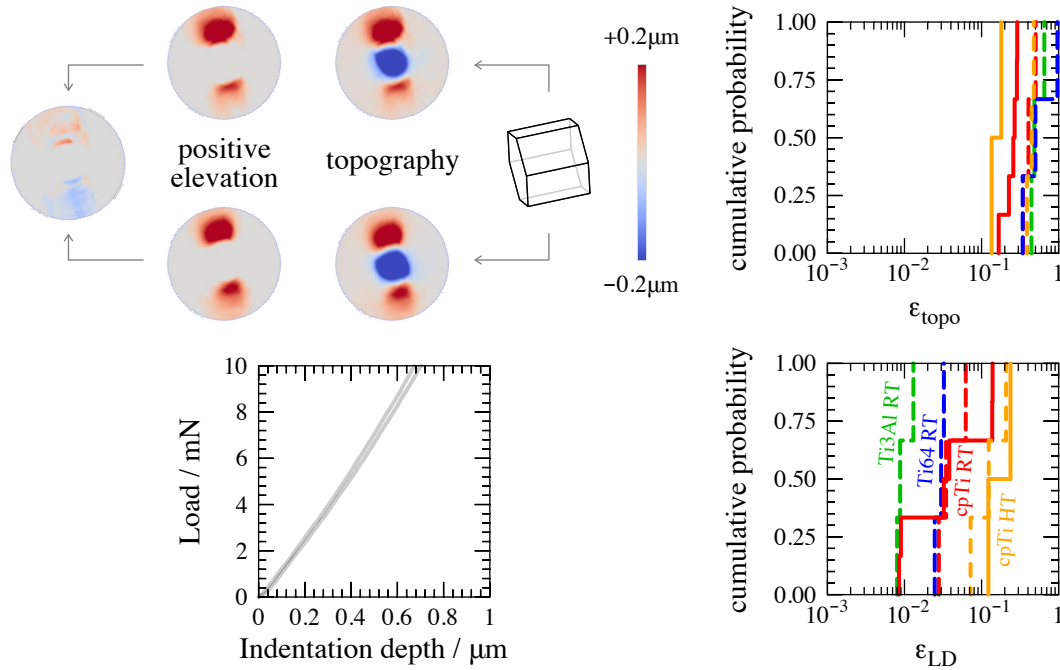


Figure 5.3: Exemplary deviations between the measured topographies (top left) and load–depth responses (bottom left) of two nominally identical indentations. Distributions of  $\epsilon_{\text{topo}}$  (top right) and  $\epsilon_{\text{LD}}$  (bottom right) resulting between indentation experiments with either nominally identical (solid) or closely agreeing (dashed) crystallographic indentation directions for the different (color-coded) material–temperature combinations.

## 5.5 Quantification of errors

Quantification of the deviation between a measured and simulated indentation response follows the same strategy as outlined in Chakraborty and Eisenlohr [19] with a few adjustments, which is introduced in Section 4.1.5. Three distinct sources of uncertainty contribute to the error  $\epsilon$  as summarized in Figs. 5.3 and 5.4.

**Measurement uncertainty** The uncertainty inherent in the indentation experiments was quantified by establishing  $\epsilon_{\text{topo}}$  and  $\epsilon_{\text{LD}}$  errors between multiple identical indentations and between multiple closely agreeing<sup>2</sup> crystallographic indentation directions. The distributions of both errors

<sup>2</sup>Pairs of indentations were selected for which the crystallographic indentation direction differs by no more than  $7^\circ$  (7 out of the 12 selected pairs have misorientation less than  $2^\circ$ ). To account for the deviation in orientation of the paired grains, one of the two indentation surface topographies was rotated about the sample normal to consistently align with the other. The in-plane rotation an-

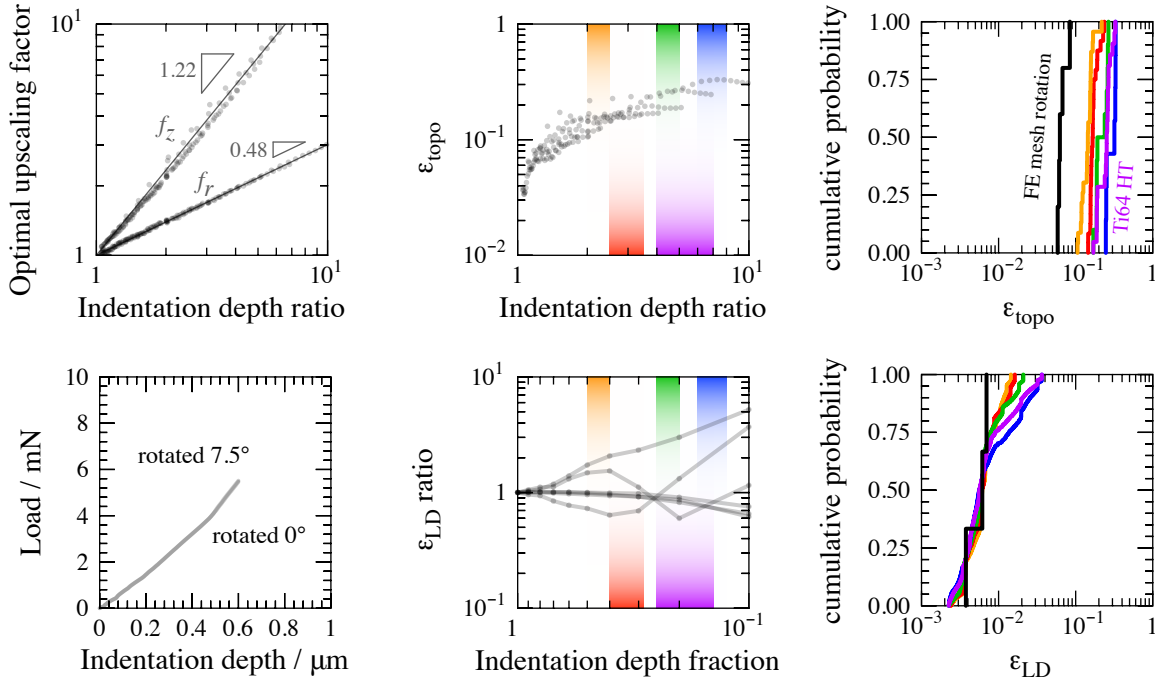


Figure 5.4: Example of (typically minor) deviations between simulated load–depth responses (bottom left) for two identical indentation directions that only differ by an in-plane rotation (of  $7.50^\circ$ ); black curves in rightmost diagrams (top and bottom) show the associated distributions of  $\epsilon_{\text{topo}}$  and  $\epsilon_{\text{LD}}$  expected from differing FE mesh alignments. Optimal factors to upscale simulated topographies in vertical and radial direction ( $f_z$  and  $f_r$ ) closely follow a power-law with respect to the indentation depth ratio (target/simulated depth, top left). Topography deviations due to such upscaling increase systematically with increasing depth ratio (top center) and result in the color-coded  $\epsilon_{\text{topo}}$  distributions (top right). Similarly, the scatter in  $\epsilon_{\text{LD}}$  ratios increases with decreasing depth fraction (evaluated/experimental target depth, bottom center); each group of ratios observed within one (color-coded) range of indentation depths applicable to that material–temperature combination is used to scale the mesh rotation-induced  $\epsilon_{\text{LD}}$  distribution (black, bottom right) to estimate the uncertainty (color-coded, bottom right) associated with simulating only up to a limited indentation depth. Indentation depth fraction in bottom center is arranged in a reversed order to have the same colored bands as indentation depth ratio in top center.



are, respectively, presented in the upper and lower row of Fig. 5.3 (right) together with one exemplary pair of nominally identical indentations (left). The  $\epsilon_{\text{topo}}$  values between indentations for which the crystallographic surface normal directions closely agree (dashed lines in Fig. 5.3) are systematically larger—by a factor of two or more—than between nominally identical indentations (solid lines). Overall,  $\epsilon_{\text{topo}}$  scatters within a range of 0.10 to 1 while  $\epsilon_{\text{LD}}$  values are generally smaller by about an order of magnitude than  $\epsilon_{\text{topo}}$ .

**Mesh alignment relative to in-plane crystallographic orientation** An in-plane rotational degree of freedom exists when only the crystallographic indentation direction (parallel to  $z$ ) is fixed. Thus, the alignment of the chosen finite element mesh (Fig. 4.4) relative to the developing indentation topography is essentially random.<sup>3</sup> To quantify the associated ranges of  $\epsilon_{\text{topo}}$  and  $\epsilon_{\text{LD}}$ , deviations between multiple simulations with different in-plane rotations of the mesh ( $0^\circ$  to  $15^\circ$ ) were calculated and their distributions plotted in Fig. 5.4 (right, black curves labeled “FE mesh rotation”). Similar to what was observed above regarding the experimental reproducibility, resulting values of  $\epsilon_{\text{topo}}$  are about an order of magnitude larger than those of  $\epsilon_{\text{LD}}$ .

**Upscaling of simulated topography** The upscaling strategy introduced in Section 5.4 has the potential to introduce  $\epsilon_{\text{topo}}$  and  $\epsilon_{\text{LD}}$  deviations. Figure 5.4 (top center) presents the values of  $\epsilon_{\text{topo}}$  resulting from the collection of upscaled simulations shown in Fig. 5.4 (top left). Since the range of indentation depth ratios between experiment and simulation is different for each material, the distribution of  $\epsilon_{\text{topo}}$  values plotted in Fig. 5.4 (top right) represents only those values that fall within the color-coded band of that respective material. For instance, the simulated indentation of CP-Ti at elevated temperature (orange) was scaled up to about twice its indentation depth, which corresponds to  $\epsilon_{\text{topo}}$  values of around 0.10 to 0.20, while the ambient temperature indentation is obtained by adding the difference of the 3rd Euler angle following Zambaldi and Raabe [135] convention and the difference of azimuthal angle between the two indents, detailed calculations of which can be found in [20].

<sup>3</sup>This concern disappears with finer mesh resolutions, but the chosen mesh used in this study is coarse to increase the affordability.

of Ti-6Al-4V (blue) was scaled up to about seven times the depth, corresponding to topography deviations  $\varepsilon_{\text{topo}} \approx 0.3$ .

**Truncation of measured load–depth response** As mentioned before, the simulated load–depth response cannot be meaningfully extrapolated to the larger experimental indentation depth. Therefore, the ratio  $\varepsilon_{\text{LD}}^{\text{trunc}}/\varepsilon_{\text{LD}}^0$ , where  $\varepsilon_{\text{LD}}^{\text{trunc}}$  is the error between a shallower simulation and the correspondingly cropped measurement and  $\varepsilon_{\text{LD}}^0$  is the error between the measured response and the corresponding (full depth) simulation, quantifies the uncertainty associated with capturing  $\varepsilon_{\text{LD}}$  at shallower simulated indentation depths. A total of six comparisons (between one simulation with fixed set of constitutive parameters, which reflect ambient temperature properties, and six distinct indents at both temperatures) are presented in Fig. 5.4 (bottom center). Each case (necessarily) agrees at the target depth, *i. e.*, at an indentation depth fraction of one, but increasingly deviates when  $\varepsilon_{\text{LD}}$  is assessed at decreasing simulated depths (or decreasing indentation depth fraction, *i. e.*, to the right in Fig. 5.4 bottom center). The deviation from unity correlates with how closely the chosen (and fixed) set of constitutive parameters approximates the experimentally probed conditions. In the plot, indentations performed at ambient temperature result in the three curves that are consistently around a ratio of one, while the other three correspond to elevated temperature indentations, for which the constitutive parameters were not optimized.

The anticipated overall distributions of  $\varepsilon_{\text{LD}}$  are generated by convolution of the  $\varepsilon_{\text{LD}}$  distribution resulting from the mesh rotation uncertainty (black curve) with the linearly interpolated distributions of the (small) population of  $\varepsilon_{\text{LD}}$  ratios within each of the color-coded bands representing a material–temperature combination. The convolution results are plotted in Fig. 5.4 (bottom right) and fall into a range of about  $2 \cdot 10^{-3}$  to  $4 \cdot 10^{-2}$ .

**Overall reliability limits for CRSS value identification** The uncertainty caused by combining deviations in topography and load–depth response was established by randomly sampling the respective distributions (right-hand side of Figs. 5.3 and 5.4) multiple times and combining the

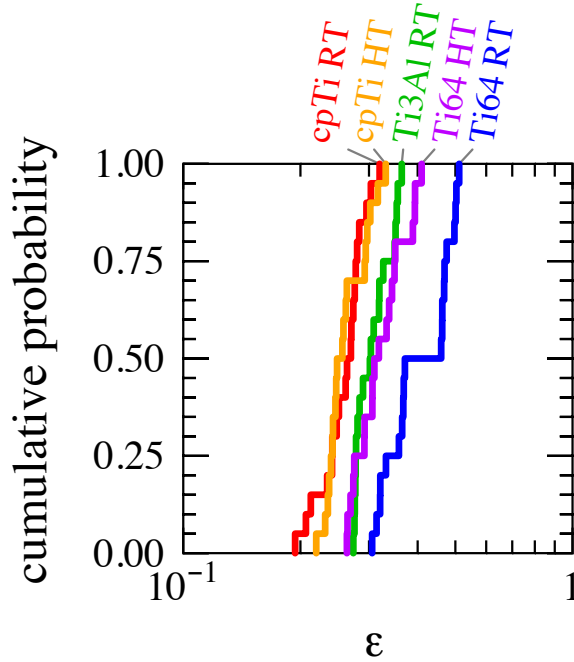


Figure 5.5: Distributions of expected overall uncertainty (Eq. (4.11)) caused by measurement and simulation limitations for each of the five material–temperature combinations.

distinct error contributions according to Eq. (4.11).<sup>4</sup> Figure 5.5 presents the resulting error distributions expected for each material–temperature combination. The range of each distribution constrains the reliability of CRSS values identified by IIA, as any error values that fall below the low end of such ranges do not provide a more reliable estimate of CRSS values than results falling within the uncertainty range.

## 5.6 CRSS values identified by inverse indentation analysis

For each of the five investigated material–temperature combinations, a subset of three to six crystallographic indentation directions that are expected to be of high sensitivity [21] was chosen from the pool of all indentations. Each of these selected indentations (labeled in black in Fig. 5.1) was subjected to inverse indentation analysis, *i. e.*, iterative adjustment of the CRSS values of basal,

<sup>4</sup>Repeat measurements along *nominally identical* directions are lacking for Ti-3Al-2.5V and Ti-6Al-4V (see Fig. 5.3 top right). Therefore, these missing distributions of  $\epsilon_{\text{topo}}$  and  $\epsilon_{\text{LD}}$  in Fig. 5.3 were estimated by shifting the distributions resulting from *closely agreeing* indentation directions (dashed lines) to lower values by factors consistent with those observed for CP-Ti.

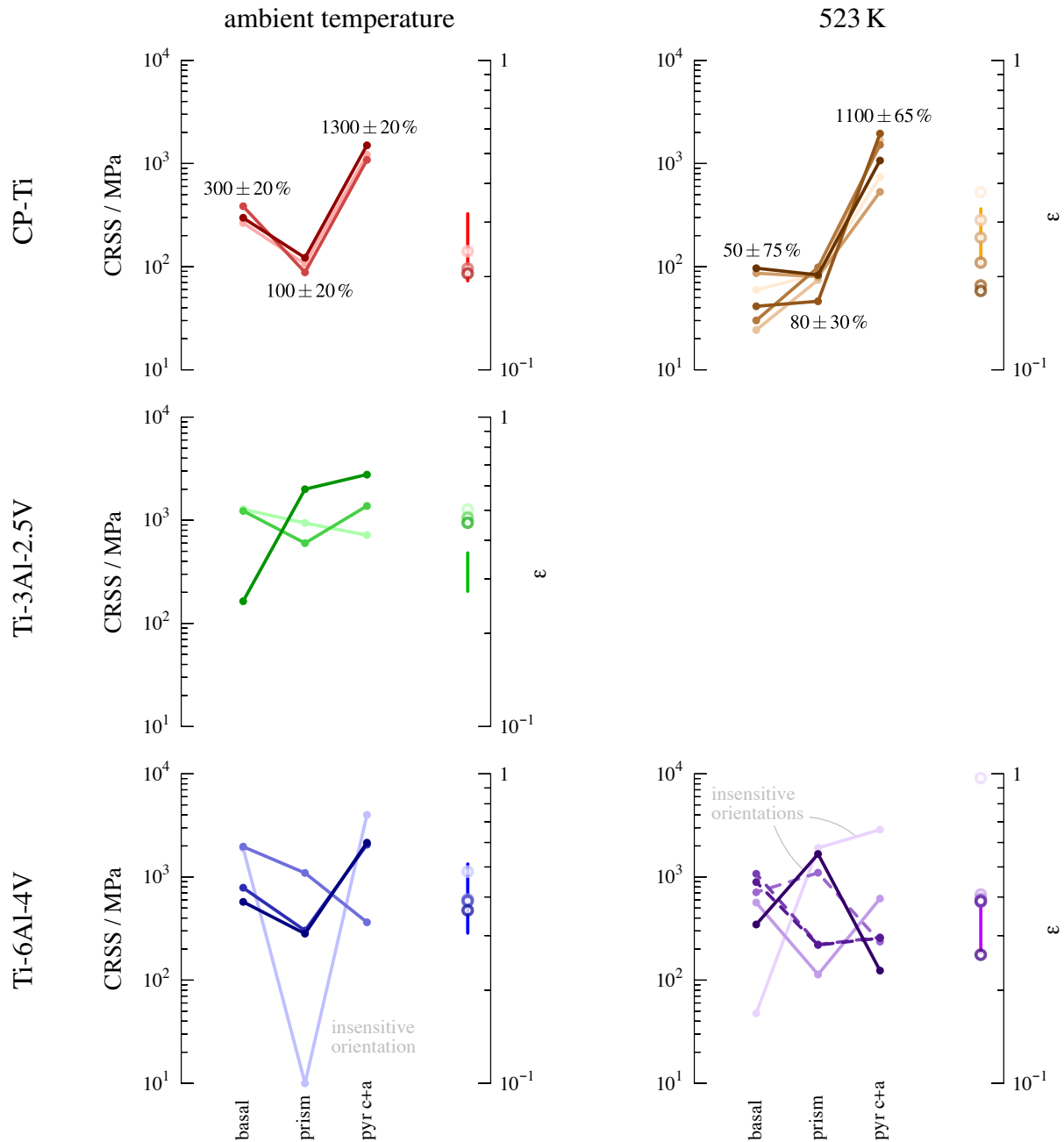


Figure 5.6: CRSS values for basal, prism, and pyramidal  $\langle c+a \rangle$  slip identified by inverse indentation analysis based on the crystallographic indentation directions highlighted in Fig. 5.1. Darker shading within each material–temperature combination corresponds to better, *i.e.* lower, fitness indicated by open circles on the right axis. Dashed lines in the bottom left show the outcomes of three independent optimization runs for the same indentation. Vertical lines represent the range of expected uncertainty as shown in Fig. 5.5.

prismatic, and pyramidal  $\langle c + a \rangle$  slip to minimize the deviation between simulated and measured load–depth curves and (piled-up) surface topography.

The resulting sets of three CRSS values are plotted in Fig. 5.6, together with the corresponding  $\varepsilon$  (right axis) reached during IIA. The degree of consistency among the CRSS sets varies notably between the five material–temperature combinations, with CP-Ti at ambient temperature (top left) being the most self consistent. When comparing the degree of consistency to the respective magnitude of the final IIA error (open circles in Fig. 5.6), a clear correlation becomes apparent. For instance, all three CRSS value sets of CP-Ti at ambient temperature reach error values slightly above 0.2, which coincides with the lower end of the expected uncertainty (vertical red line). In contrast, all other cases exhibit  $\varepsilon$  values that do not cluster near the bottom of the uncertainty range but are spread out with values frequently exceeding 0.4. Thus, we conclude that consistent identification of CRSS values by IIA cannot be expected unless the overall uncertainty  $\varepsilon$  (Eq. (4.11)) introduced through experiment and simulation stays below about 0.2. The dominant contribution to the overall uncertainty is, in general, from  $\varepsilon_{\text{topo}}$  as demonstrated by the results shown in Figs. 5.3 and 5.4 (right). Most critically, the indentation simulations were expedited by upscaling them to the experimental depths. However, to keep the associated  $\varepsilon_{\text{topo}}$  below 0.2 (see Fig. 5.4 top center), the indentation depth ratio between both should be less than 3, which was not the case for Ti-3Al-2.5V and Ti-6Al-4V. Other considerations to keep  $\varepsilon_{\text{topo}}$  within the acceptable range include adopting good surface preparation (for instance, prevention of surface oxidation at elevated temperature) and having a large grain size to reduce heterogeneity below the surface.

For the most reliable case of CP-Ti at ambient temperature (Fig. 5.6 top left), the CRSS values could be established to within about 20 % uncertainty. Those values agree closely with the findings in the originally proposed IIA [136], which optimized the CRSS values concurrently against two indentations. An analysis of the IIA methodology applied to face-centered cubic materials [19] indicated that the use of two indentations was not necessary, as it provided no additional accuracy or precision. Following [21], our use of a single (strategically chosen) orientation with high sensitivity for identifying CRSS values reproduced the results of [136], which again confirms that one

indent is sufficient for hexagonal metals.

Despite being not as reliable as the ambient temperature evaluation, the IIA results for CP-Ti at elevated temperature (Fig. 5.6 top right) suggest that the resistance of basal slip is reduced at 523 K compared to ambient temperature. In contrast, the outcome of the IIA for both alloys (Ti-3Al-2.5V and Ti-6Al-4V) exhibits even less certainty such that there is little confidence to extract reliable CRSS values from them.

## 5.7 Summary

Inverse indentation analysis (IIA) performed to establish initial CRSS values relies on the comparison of experimental and simulated load–depth curves and residual surface topography. Both metrics carry uncertainties that can be quantified, for instance by repeated nominally identical indentations. A quantitative error analysis was conducted in the context of IIA seeking initial CRSS values of basal, prism, and pyramidal  $\langle c + a \rangle$  in CP-Ti, Ti-3Al-2.5V, and Ti-6Al-4V at two temperatures. Generally, the uncertainty in the surface topography is greater than in the load–depth response. The IIA method shows good reproducibility of identified CRSS values when the errors associated with simulation and experimental uncertainty are less than about 20 %.

## CHAPTER 6

### GRAIN BOUNDARY SLIP TRANSFER CLASSIFICATION AND METRIC SELECTION

This chapter is an expanded version from Zhao et al. [140].

#### 6.1 Introduction and motivation

The deformation of polycrystalline materials is heterogeneous because the local stress states are constrained by complex evolving boundary conditions associated with the deformation in neighboring grains [8, 28, 35, 62]. Grain boundaries (GBs) are often considered as strong barriers to dislocations, which lead to the formation of dislocation pile-ups [6]. However, it is also possible that slip by an incoming dislocation can be transferred into the neighboring grain by passing through the boundary or by absorbing it into the GB and re-emitting a dislocation on a similarly oriented slip system in the receiving grain [6, 85]. This process could reduce the buildup of local stress, or weaken the GB by accumulation of residual Burgers vector content that could facilitate crack nucleation at GBs [7, 13, 105, 108]. Comparisons of crystal plasticity simulations of carefully characterized experiments demonstrate the greatest disagreement in regions near grain boundaries, implying that introducing GB properties into crystal plasticity models is needed to improve the ability to predict the evolution of local stress and strain near boundaries [9, 14, 15, 29, 45, 46, 61, 76, 77, 78, 101]. Nevertheless, reliable metrics that describe slip transfer occurrence at GBs are not well established [2, 9, 56], and they are critical for implementing this phenomenon into standard crystal plasticity simulations of polycrystals [9, 53].

Some frequently discussed metrics relevant to slip transfer from slip system  $\alpha$  to slip system  $\beta$  in the neighboring grain include the misorientation between the two neighboring grains (disorientation angle), Luster–Morris parameter ( $m'_{\alpha\beta}$ ), and the magnitude of the normalized residual Burgers vector ( $\Delta b_{\alpha\beta}$ ) [9, 72, 82, 110]. Recent experimental quantification of slip transfer metrics in pure aluminum reported by Bieler et al. [9] and Alizadeh et al. [2] indicate that slip transfer was observed at low-angle boundaries when  $m'_{\alpha\beta} > 0.97$  or  $m'_{\alpha\beta} > 0.9$  together with  $\Delta b_{\alpha\beta} < 0.35$ .

Bieler et al. [9] also suggested there might exist two “composite” metrics, namely  $m'_{\alpha\beta}$  either multiplied by the sum  $SF_{\alpha} + SF_{\beta}$  of Schmid factors of the observed slip systems or divided by  $\Delta b_{\alpha\beta}$ . The effectiveness of these metrics and their relative importance is presented graphically and assessed with simple statistical comparisons. An assessment of the interrelationship of three or more metrics is difficult when limited to human perception that most easily detects relationships in a (two-dimensional) space spanned by two metrics.

In this chapter, an exhaustive evaluation of the aforementioned metrics and their combinations are performed based on the oligo pure Al data of Bieler et al. [9] and Alizadeh et al. [2] using artificial neural network (ANN) as classifier for slip transfer in order to take advantage of its ability to solve hierarchical problems in multidimensional space by mimicking the behavior of the brain [70, 102, 131]. Furthermore, same evaluations were performed for an alloy with a less symmetric crystal structure, *i. e.*, hexagonal Ti-5Al-2.5Sn, using a simple ANN architecture that was previously established in the Al study. This sample also has more complicated sub-surface neighboring grain and grain boundary geometries as oppose to nominally columnar grain boundaries between large grains presented in the Al samples. In addition to the metrics used in the previous study, an extra slip transfer metric, *i. e.*, the significance of ledge observations, was considered in the Ti alloy study.

## **6.2 Slip transfer dataset**

### **6.2.1 Al oligocrystals dataset**

Observations of slip transfer, possible slip transfer, and no slip transfer were collected from 222 GBs across two oligocrystalline Al foils with either a near-cube texture (84 GBs) or a rotated-cube texture (138 GBs) deformed 4 % in tension at ambient temperature [2, 9]. The criteria used to make these observations are discussed at length in [9] and are briefly noted here: Convincing instances of slip transfer occurred when there was highly apparent continuity of slip traces (microshear bands) from one grain to the other grain, with little topography other than slip traces along the grain boundary, implying that the boundary did not cause a significant disruption of slip (the surface between



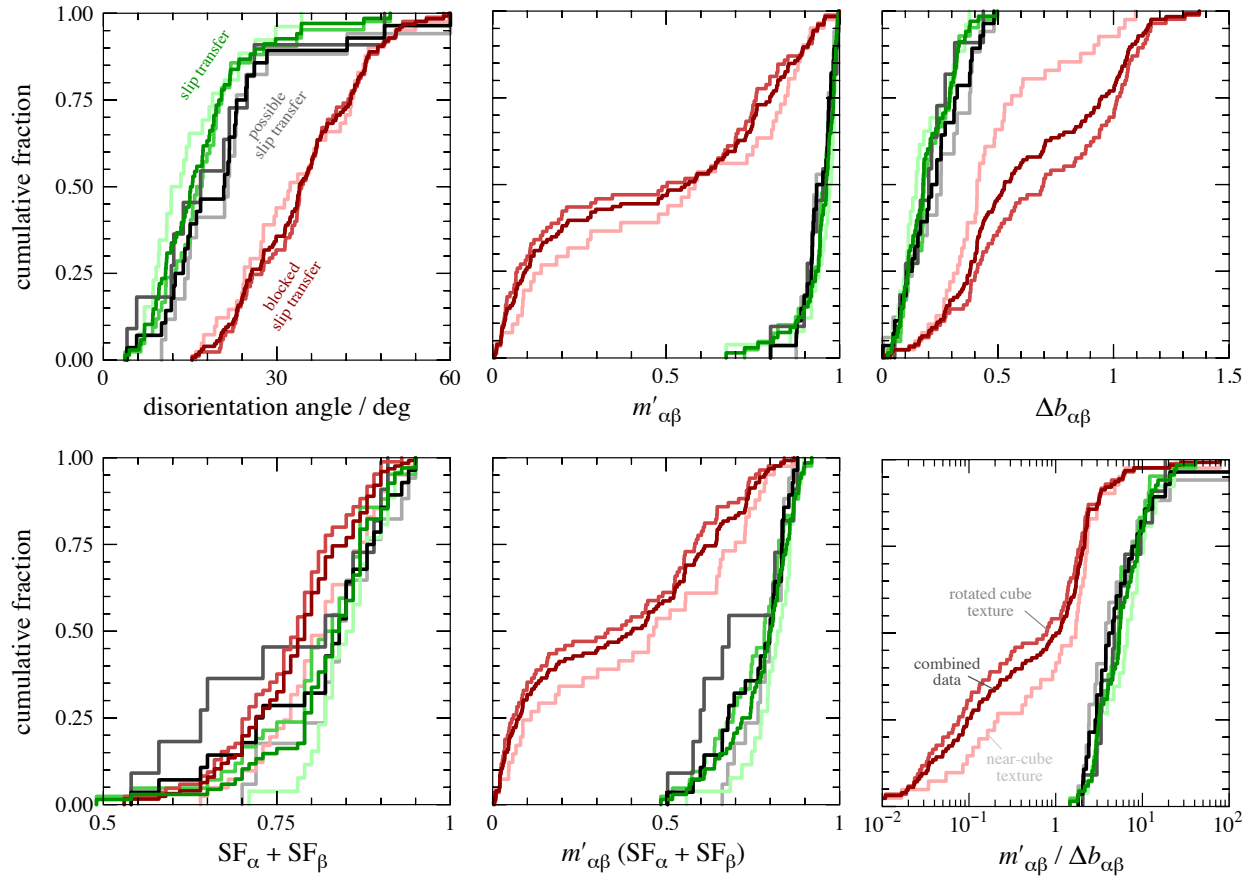


Figure 6.1: Distributions of metric values classified as either definite, likely, or no slip transfer (green, gray, red) based upon oligo Al data. The underlying population of near-cube texture, rotated-cube texture, and their union are indicated by light, intermediate, and dark color shade, respectively.

slip bands going across the boundary was smooth). Instances of no slip transfer were indicated by a lack of continuity of slip across the boundary, but slip bands were still clearly visible in the grain on either side of the boundary; such grains often had significant topographic features along the GB such as a ledge that indicated a discontinuity in strain. Cases with less certainty about slip transfer, where evidence of contiguous slip was present together with heterogeneous strain along the boundary, were put in the ‘possible slip transfer’ category, representing about 15 % of the observations. The clearest identification of metrics for the activity of slip transfer emerged when non-slip transfer cases were assessed using only the observed slip systems within the neighboring grains (recognizing that some slip systems in neighboring grains had well aligned slip systems, but

no slip activity was observed on these systems). For each observation, there are four “direct” metrics, namely the disorientation angle, Luster–Morris parameter  $m'_{\alpha\beta}$ , normalized residual Burgers vector magnitude  $\Delta b_{\alpha\beta} = 2\|\mathbf{b}_\alpha - \mathbf{b}_\beta\| / (\|\mathbf{b}_\alpha\| + \|\mathbf{b}_\beta\|)$ , and the sum  $SF_\alpha + SF_\beta$  of Schmid factors of the observed slip systems, and two “composite” features, namely  $m'_{\alpha\beta} (SF_\alpha + SF_\beta)$  and  $\log(m'_{\alpha\beta} / \Delta b_{\alpha\beta})$ .

Figure 6.1 compares for each of the six metrics, the cumulative fraction of observations of slip transfer, possible slip transfer, and blocked slip (green, gray, and red, respectively) for both textures individually (two lighter shades) as well as for their combination (darkest shade), resulting in nine populations per metric. Two observations can be made: First, the (gray) populations of possible slip transfer are smaller than either of the other sets, and they are consistently close to those of actual slip transfer (green). Second, except for  $\Delta b_{\alpha\beta}$ , both textures result in similar distributions. Therefore, only the categories of slip transfer and no slip transfer are considered in the subsequent assessment using the combined texture data (*i.e.*, the dark green and dark red distributions, constituting 194 out of the 222 data).

## 6.2.2 Polycrystalline Ti-5Al-2.5Sn dataset

A total of 158 GBs in a tensioned Ti-5Al-2.5Sn sample (up to 13 % elongation at 728 °C) were analyzed and categorized as either slip transfer or no transfer for each boundary by Edge [33]. In addition to the six slip transfer metrics that were considered in Al study, another direct metric, *i.e.*, the significance of ledge observations (based on human observations), were also included for Ti-5Al-2.5Sn. Distributions of slip transfer activity based on each metric are plotted in Fig. 6.2, with green represents slip transfer and red reflects no transfer events.

## 6.3 Double-layer ANN architecture

The biggest problem with applying machine learning on a small training set is a higher risk of overfitting or, equivalently, of poor generalization. Feng et al. [37] showed that an ANN with a simple network structure containing only a few hidden layers is potentially effective with small

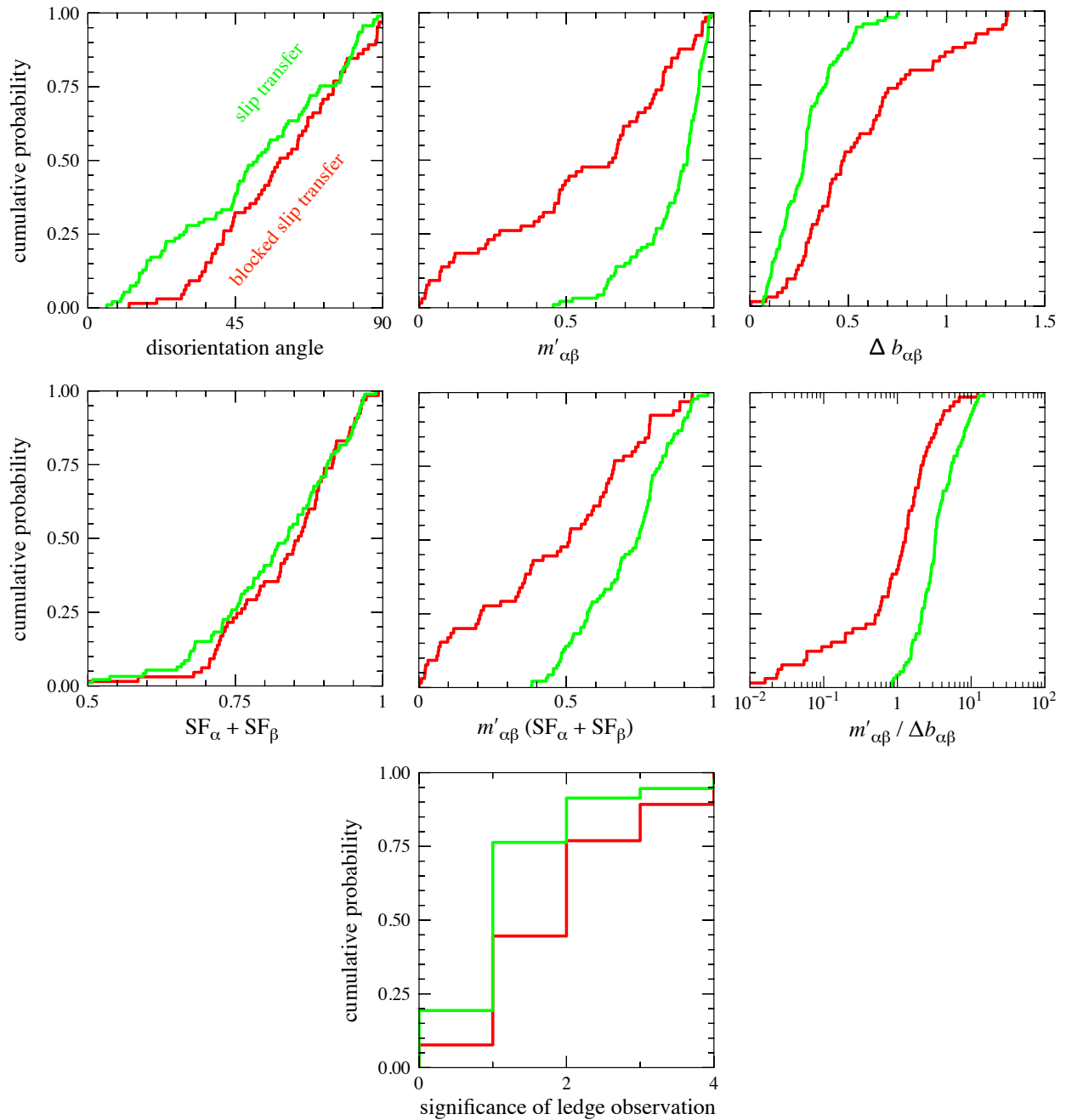


Figure 6.2: Distributions of metric values classified as either definite (green) or no slip transfer (red) based on Ti-5Al-2.5Sn data (tensile deformed at 728 K).

training sets that are quite common for materials science research. They also demonstrated that a simple ANN does an incrementally better job than a support vector machine (SVM), another commonly used machine learning tool. This motivated our use of an ANN with two hidden layers (Fig. 4.10). The appropriateness of using this network is validated in the rightmost plots in Fig. 6.3—no apparent overfitting is observed in our case when training with more than about 40 data sets.

The complete architecture of the network used in this study is shown in Fig. 4.10 and has an input layer with  $N_{\text{input}}$  nodes, two hidden layers containing  $N_{\text{hidden}}$  nodes each, and a two-node output layer to classify the input data into either slip transfer being observed or not. Every edge linearly maps the source node value to the target node. All edge values are summed and modified by either the (local) rectified linear units (“ReLU”) function within the hidden layer or the (non-local) softmax function at the output layer. The ultimate classification is based on which of the two output node values is larger.

One training cycle of the ANN consists of forward-feeding all data sets and reducing the value of the loss function (squared  $L_2$  norms of the respective differences between predicted and correct classification) by gradient descent, *i.e.*, updating all edge mapping functions through back-propagation (with a learning rate of  $10^{-4}$ ). Training is terminated when changes to the edge mapping stabilize, which corresponds to roughly 2000 cycles (epochs). The computation work was supported in part by Michigan State University through computational resources provided by the Institute for Cyber-Enabled Research.

## 6.4 Classifying slip transfer in Al oligocrystals

### 6.4.1 Results

The major question addressed in this study is how accurately an ANN can classify slip transfer across GBs based on six metrics related to the crystallography at the boundary and an assumed uniaxial stress state that provides Schmid factor values for each slip system (a measure of the resolved shear stress acting on each slip systems). Each individual metric and all their various

combinations have been tested. Moreover, the influence of the ANN architecture ( $N_{\text{hidden}}$ ) and of the amount of training data ( $N_{\text{training}}$ ) has been examined. To investigate the architecture, the number of hidden layer nodes was varied as  $N_{\text{hidden}} = 1, 2, 5, 10, 25, 50$  and  $100$ . To establish how much training data is necessary, two non-overlapping subsets, each containing  $N_{\text{training}} = 2, 5, 10, 20, 40, 80$  and  $97$  data points, are randomly selected from the overall data (194 observations). The first set is used for training, while the first or the second are utilized to evaluate the classification performance of the trained ANN. Systematic differences in classification performance obtained using the test data or the training data indicates overfitting (*i.e.*, memorization) of the training data. Figure 6.3 presents the classification accuracy (reflecting the average of 20 independently trained ANN instances) resulting from varying  $N_{\text{input}}$ ,  $N_{\text{hidden}}$ , as well as  $N_{\text{training}}$ .

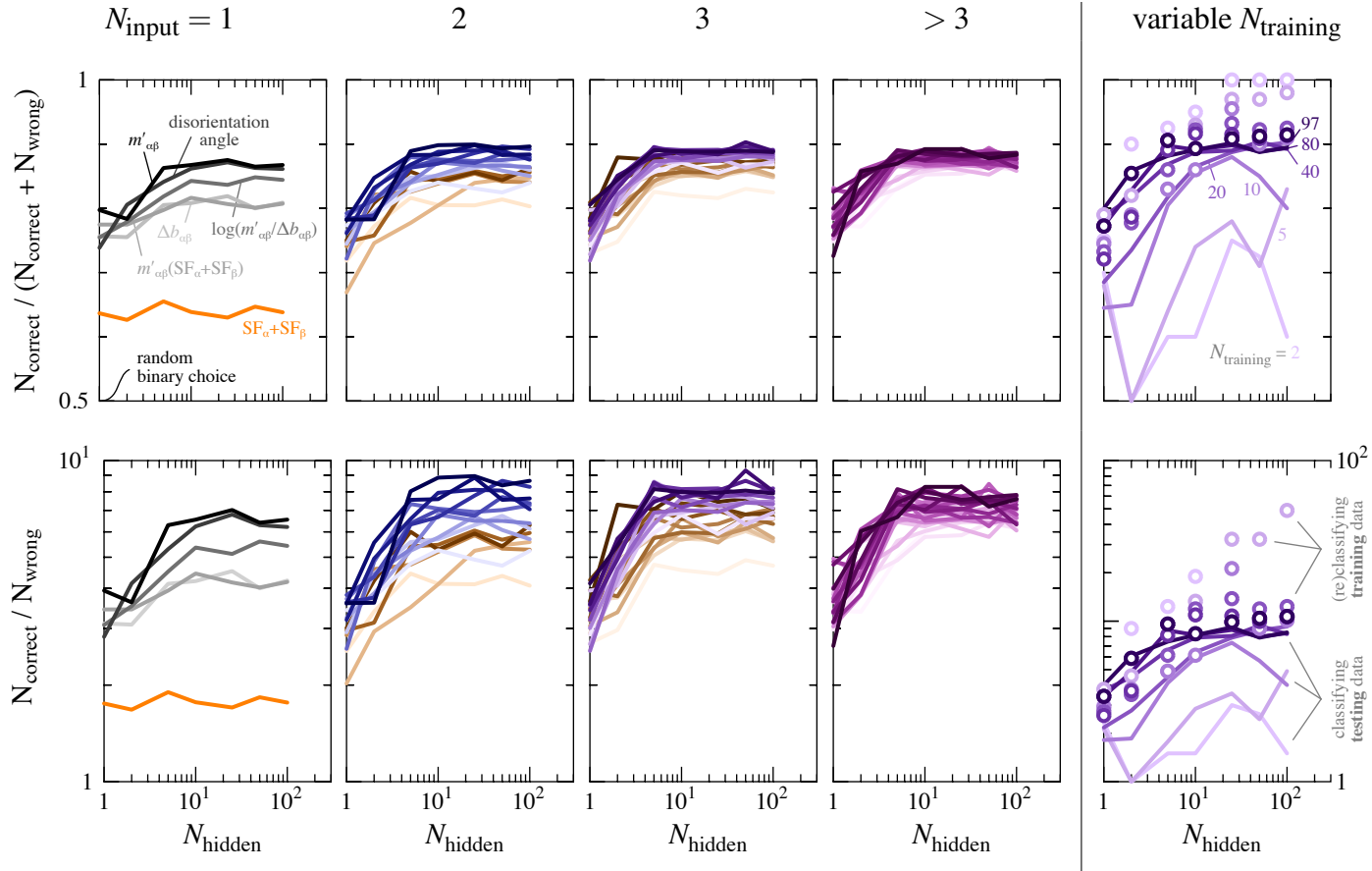


Figure 6.3: Classification accuracy as function of hidden layer node count  $N_{\text{hidden}}$  for different  $N_{\text{input}}$  of compounded slip transfer metrics with  $N_{\text{training}} = 97$ . Both rows present the *same* data but use different ratios (and different scales) to measure accuracy. Color shading reflects relatively better accuracy from light to dark. Orange and brownish shading indicates that  $\text{SF}_\alpha + \text{SF}_\beta$  are included in the input metric(s). The right-most column varies  $N_{\text{training}}$  (shades of purple) for one case of  $N_{\text{input}} = 3$  and contrasts the classification accuracy of testing data (lines) to that of just reclassifying the training data (circles).

Table 6.1:  $F$ -scores of metric value distributions shown in Fig. 6.1.

metric	$F$ -score
$m'_{\alpha\beta}$ ( $SF_{\alpha} + SF_{\beta}$ )	1.0
disorientation angle	0.97
$m'_{\alpha\beta}$	0.96
$\Delta b_{\alpha\beta}$	0.84
$\log(m'_{\alpha\beta}/\Delta b_{\alpha\beta})$	0.75
$SF_{\alpha} + SF_{\beta}$	0.063

## 6.4.2 Discussion

**Classification based on single metric** These accuracies should reflect the distinctiveness (or separability) of the metric distributions plotted in Fig. 6.1. The quantity

$$F = \frac{\left(\langle x_{(+)} \rangle - \langle x \rangle\right)^2 + \left(\langle x_{(-)} \rangle - \langle x \rangle\right)^2}{\sigma_{(+)}^2 + \sigma_{(-)}^2}, \quad (6.1)$$

termed  $F$ -score [22], is one method to quantify the ability to discriminate two sets  $x_{(+)} \cup x_{(-)} = x$  of real numbers having unbiased variances of  $\sigma_{(+)}^2$  and  $\sigma_{(-)}^2$  and average values of  $\langle x_{(+)} \rangle$  and  $\langle x_{(-)} \rangle$ . Here,  $x_{(+)}$  and  $x_{(-)}$  correspond to observations of slip transfer and blocked slip, *i. e.*, green and red distributions in Fig. 6.1, respectively. An  $F$ -score of zero is interpreted as  $x_{(+)}$  being inseparable from  $x_{(-)}$  and separability increases with increasing  $F$ -score. Table 6.1 collects the  $F$ -scores of all six metrics sorted from large (easily separable) to small (not easily separated). Surprisingly, the relative ranking of the  $F$ -scores and the ANN ranking are nearly in the opposite order when only a single metric is used for classification (*i. e.*  $N_{\text{input}} = 1$  in Fig. 6.3 left). However, the exceptionally low accuracy resulting from the  $SF_{\alpha} + SF_{\beta}$  metric is consistent with its  $F$ -score being almost zero.

**Classification based on more than one metric** Compounding more than one metric as ANN classification inputs results in a slight but notable increase in the observed accuracy compared to the classification based on only a single metric. The attainable accuracy does not improve after compounding more than two metrics, *i. e.* for  $N_{\text{input}} > 2$ , but the resulting variation decreases

with increasing the number of input metrics. If the metric  $SF_\alpha + SF_\beta$  is part of the input, the accuracy is systematically worse than without (orange curves in Fig. 6.3). This effect diminishes with increasing  $N_{\text{input}}$ , in line with the overall decrease of the variance.

**Influence of ANN architecture** The attainable classification accuracy saturates at a hidden layer size of 10 nodes and does not change meaningfully up to the maximum investigated  $N_{\text{hidden}} = 100$ . This indicates that the complexity of the binary slip transfer classification based on one (or more) metrics is low and can be mapped as accurately as possible with an ANN containing a hidden bi-layer of no more than  $2 \times 10$  nodes.

**Influence of input data size** When using subsets with less than 40 data sets to train the ANN, the accuracy of the classification resulting from the (unseen) testing data are distinctly lower than those resulting from reclassifying the (already seen) training data. This discrepancy between lines and circles in Fig. 6.3 (right) is indicative of memorization—in contrast to the desired generalization—by the ANN and becomes more pronounced with lower ratios of  $N_{\text{training}}/N_{\text{hidden}}$ . This is evidenced by (i) the growing deviation between lines and circles with increasing  $N_{\text{hidden}}$ , and (ii) the systematically larger deviation with decreasing  $N_{\text{training}}$  (lighter shades).

### 6.4.3 Summary

Prior work has identified  $m'_{\alpha\beta}$  and the disorientation angle between grains as metrics that are correlated with observations of slip transfer. An open question addressed with this study is whether a better slip transfer predictor can be extracted from simultaneously considering multiple metrics using an ANN as classifier, thus avoiding projections to lower dimensions.

The current ANN-based analysis indicates that no new insights emerge from an objective assessment of interrelationships between multiple metrics. Compared to using a single metric, compounding two (or more) metrics as ANN inputs slightly raises the attainable classification accuracy from 87 % to about 90 %. The highest accuracy results from considering metrics that reflect the geometrical relationship between the two grains, *i.e.* the disorientation angle and  $m'_{\alpha\beta}$ , a widely



used metric that encodes geometrical information of slip systems in neighboring grains. Nevertheless, these two metrics are scalar representations of three-dimensional geometric relationships, so they may have lost information critical to predicting slip transfer more effectively.

Because the accuracy could not be systematically improved by adding more than two input dimensions, these six metrics do not provide sufficient information to enable better prediction. Nevertheless, increasing the input dimension improves the “robustness” of the trained ANN as reflected by the diminishing “worsening effect” of the  $SF_\alpha + SF_\beta$  contribution and the smaller variance of resulting accuracy.

The low accuracy resulting from the  $SF_\alpha + SF_\beta$  metric indicates that high global resolved shear stress is insufficient to cause slip transfer. This also suggests that use of the global stress state cannot predict the driving forces that actually influence slip transfer at the scale of the grain boundary. At that scale, the local stress state is highly variable along the boundary, as shear bands periodically impose large local shear strains that are superimposed by far-field stress states, which evolve in a complex way as influenced by the changing boundary conditions that each grain imposes on its neighbor. Consequently, knowing the evolution of the local stress state may enable better assessments of driving forces for slip across the length of a particular boundary. However, this is difficult to discern, as prior efforts to identify correlations between local stress states and strain evolution near boundaries have not yielded lucid understanding [29, 45, 46, 101], suggesting that the history of activated slip systems imposes significant latent hardening effects that could prevent activation of additional slip systems with high resolved shear stresses. If so, then commonly used assumptions of plentiful dislocation sources may not be appropriate for predicting the local evolution of strain. Hence, an incremental approach of installing simple slip transfer mechanisms [1, 14, 53, 84] with strong latent hardening rules into crystal plasticity models to identify how they alter the evolution of the local stress state may provide insights about causes of the complex evolution of local stresses. If models of characterized experiments, such as those behind the data used here, are used to identify local stress states, locally informed Schmid factors may identify more convincingly conditions where slip transfer did and did not occur. With such improvements,

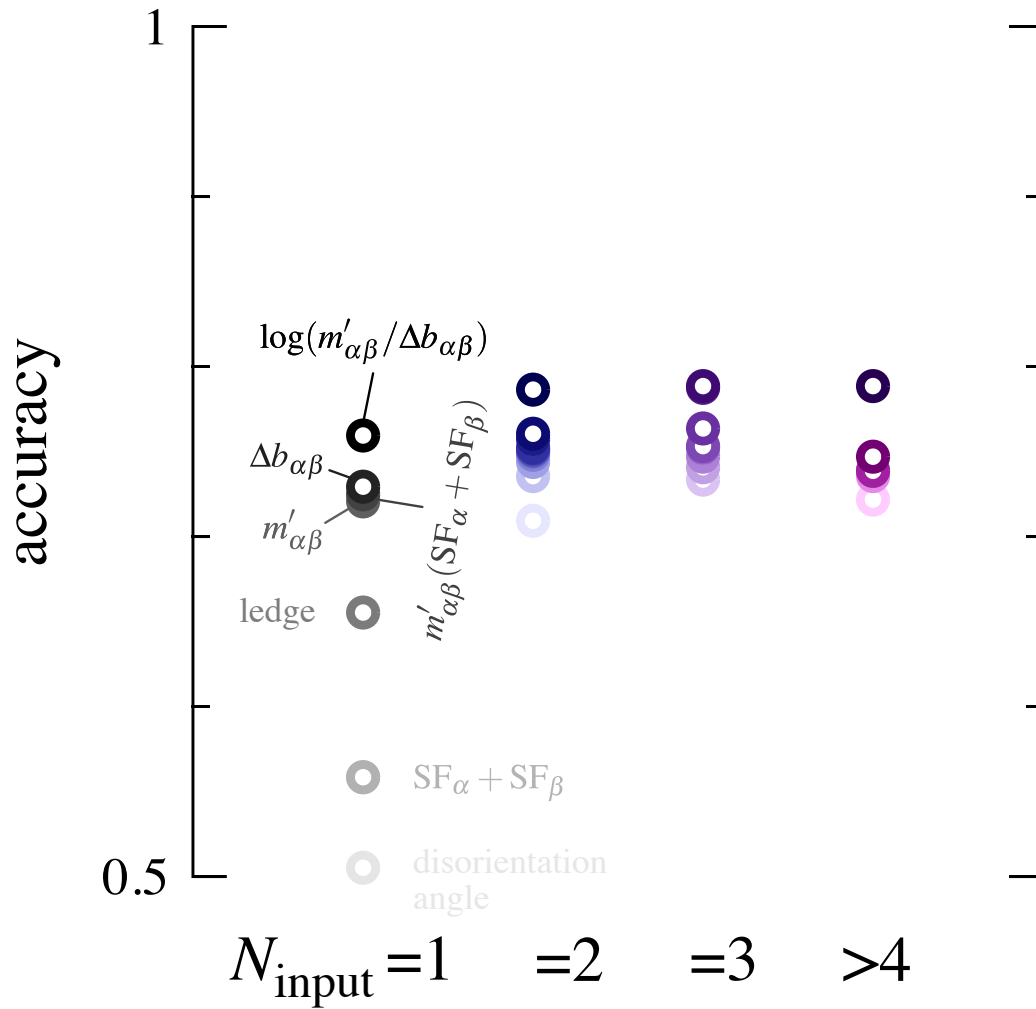


Figure 6.4: Average slip transfer classification accuracy of Ti-5Al-2.5Sn with double hidden layer ANN ( $N_{hidden} = 20$ ) based on different combinations of metrics.

it may be possible to reduce the uncertainty in identifying a criterion for slip transfer.

## 6.5 Classifying slip transfer in polycrystalline Ti-5Al-2.5Sn

### 6.5.1 Results & discussion

According to Section 6.4.2, a double-layer ANN architecture with 20 nodes per hidden layer is sufficient for classifying GBs slip transfer and thus it was fixed for all analyses for Ti-5Al-2.5Sn. Since known ineffective metrics can negatively affect the classification performance, only com-

binations of effective metrics are considered for  $N_{\text{input}} > 1$ . For each metric or combination, the average classification accuracy was obtained from 20 independently trained ANNs with each run using non-overlapping  $N_{\text{training}} = 111$  and  $N_{\text{testing}} = 47$  (to “test” classification accuracy) from random sampling of the 158 GB dataset. These accuracies are plotted as circles in Fig. 6.4.

Similar to Al study, the best classification accuracy for Ti-5Al-2.5Sn is achieved by considering two metrics and it cannot be further improved by adding more metrics. This suggests that there is no further insight into interrelationships among these metrics for hexagonal Ti-5Al-2.5Sn as well. On the other hand, different observations are noted in several aspects. First, the maximum attainable accuracy is between 75 % and 80 % for a single metric or a combination of multiple metrics, which is about 10 % smaller than that in the Al study. This might indicate that slip transfer phenomena are more complicated situations in hexagonal crystals than in cubic crystals. Furthermore, in contrast to Al study where disorientation angle is among the most effective slip transfer metrics, it is the most ineffective one for Ti-5Al-2.5Sn whereas  $m'_{\alpha\beta}$  remains one of the most effective metrics. This is likely due to the potential slip systems present in hexagonal crystals are less abundant and homogenous than in cubic crystals such that the alignment of slip systems becomes way more important than grain boundary inclination. Moreover, as there are four families of slip systems with different CRSS thresholds for slip behavior, there are many more conditions where a high misorientation between two grains leads to well aligned slip planes and Burgers vectors than is the case for cubic slip systems. For example a  $45^\circ$  misorientation about an  $\langle a \rangle$ -axis leads to perfect slip alignment between basal and pyramidal  $\langle a \rangle$  slip systems, and similarly, a  $90^\circ$  misorientation about an  $\langle a \rangle$ -axis leads to perfect alignment of prism and basal slip systems. In addition, the more complicated 3-D nominally equiaxed grain geometries beneath the surface in Ti-5Al-2.5Sn—rather than nominally columnar boundaries between large grains with free surfaces on both sides of the samples in the Al study—leads to more constraint and hence, complex states of stress than is present in the grains of the oligocrystals where most of the grain has a free surface.

### **6.5.2 Summary**

Slip transfer phenomena in hexagonal Ti-5Al-2.5Sn are more complicated situations than in the Al oligocrystal as the maximum classification accuracy obtained by ANN is consistently about 10 % smaller in the polycrystalline Ti alloy. The disorientation angle is not an effective metric in Ti-5Al-2.5Sn, which may be a result of less available slip systems present in hexagonal crystals as well as possible sub-surface neighbor grain and grain boundary influences. Similar to Al, classification accuracy for hexagonal Ti-5Al-2.5Sn cannot be improved with more than two slip transfer metrics.

## CHAPTER 7

### AUTOMATED BODY-CENTERED CUBIC $\beta$ RECONSTRUCTION

#### 7.1 Introduction and motivation

$\beta$  reconstruction is needed for studying Ti and Zr alloys when the historical information of the current microstructures is required. Automated tools to generate reconstructed  $\beta$  orientation maps from output files of a commercial tool to identify orientations, *i. e.*, EBSD mapping (*a. k. a.*, Orientation Imaging Microscopy<sup>TM</sup>, or OIM), is in great demand. A number of methods have been reported in the last 20 years [11, 18, 42, 49, 65, 94, 134]. These methods mainly deviate in how to group  $\alpha$  grains resulting from the same parent  $\beta$  grain. They are summarized into the following two categories.

The first category is grouping the reconstructed  $\beta$  orientations shared by the  $\alpha$  grains resulting from the same parent grain. The existing methods in this category are listed below.

- **The Monte Carlo method** [42] This method randomly selects pairs of points and finds the transformed  $\beta$  orientations by first minimizing the misorientation angle between the two points and followed by a global minimization of the sum of the misorientation angle. This method gives accurate results but is computationally costly because the back-transformation calculation (the most expensive part) needs to be performed beforehand.
- **Summation of mutual misorientation angle (SMMA) method** [119] The SMMA method is similar to the Monte Carlo method. The difference is that the SMMA method identifies the set of parent  $\beta$  orientations with just one step (by minimizing the sum of misorientation angles between the  $\beta$  members). Likewise, this method generates accurate results but is computationally expensive.
- **Image segmentation method** [134] This method uses the variational model of Mumford-Shah for computer vision image segmentation to cluster distinct  $\beta$  orientations. This method

depends on a clustering algorithm and does not need to calculate misorientation angles. Since it uses a “powerful” clustering algorithm, it can also be applied to non-Burgers orientation relation microstructures.

The second category is grouping  $\alpha$  orientations resulting from the same parent grain. Since the back-transformation calculations are not needed for the grouping, methods in this category are generally less expensive than those in the previous category.

- **The groupoid method** [18] or **the triplet method** [65] This method first identifies triplets of grains (“nucleus”) with a low tolerance angle. Then it grows the triplets with relaxed tolerance until grouping the whole map. This is a non-iterative and quick method, but it may not group all of the grains.
- **The clustering method** [49] This method is a more efficient version of the SMMA method. It tries to cluster the alpha grains instead of reconstructed  $\beta$  orientations to avoid massive back-transformation calculations. However, similar to the groupoid method, it is less accurate (may not group island grains within larger grains or small groups of child grains).
- **The Markov Cluster Algorithm (MCL) method** [11, 94] The MCL method also uses a computer vision tool designed to discover natural groups in graphs. Like other methods in this category, it is less accurate because it may add parent grain orientations if too many clusters are identified.

To summarize,  $\beta$  reconstruction is a competition between efficiency and accuracy: methods grouping  $\alpha$  grains are more efficient but less accurate than those grouping reconstructed  $\beta$  orientations.

This chapter presents a  $\beta$  cluster-averaging approach to facilitate automated  $\beta$  reconstruction from EBSD mapping in Section 7.3 and validation of the approach based on synthetic and measured data in Sections 7.3.2 and 7.3.3. Since the new approach works by grouping  $\beta$  orientations, it should be an accurate method. On the other hand, this new approach uses a window searching

algorithm to pre-select spatially-close  $\alpha$  grains (candidates) likely coming from the same parent grain. The window searching algorithm narrows down the  $\alpha$  population per reconstruction unit and inherently supports parallel execution, which can greatly accelerate the  $\beta$  reconstruction of the whole map. Therefore, the new cluster-averaging approach has a good balance of accuracy and efficiency.

## 7.2 The unique determination rule

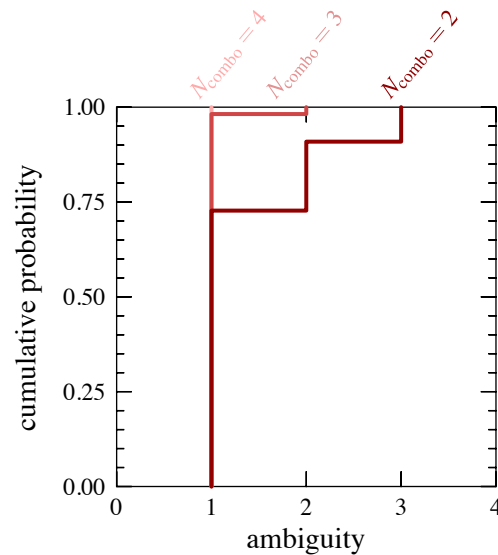


Figure 7.1: The “parent” beta orientation is uniquely determined when  $N_{\text{combo}} \geq 4$ .

During the phase transformation, a large  $\beta$  grain can dissociate into several child  $\alpha$  grains as due to the variant selections. As discussed in Section 4.3, each child  $\alpha$  has 6 possible parent  $\beta$  orientations according to the BORs. Therefore, to reconstruct the parent orientation, one must find a uniquely determined  $\beta$  orientation shared by all child  $\alpha$  variants.

To understand how many  $\alpha$  variants are needed to determine a unique  $\beta$  orientation and whether the determined  $\beta$  orientation is correct: a synthetic  $\beta$  is used to produce 12  $\alpha$  orientations; then the possible parent  $\beta$  orientations shared by a group ( $N_{\text{combo}} = 2, 3, 4, \dots, 12$ ) of these 12  $\alpha$  orientations are calculated and compared to the original  $\beta$  orientation. Figure 7.1 shows the number of possible parent  $\beta$  orientations determined from varying  $\alpha$  group sizes, and it is

found that the parent  $\beta$  orientation is uniquely determined when  $N_{\text{combo}} \geq 4$ . It is also found that the uniquely determined  $\beta$  orientation is always correct. Thus, a strategy to do  $\beta$  reconstruction is finding the unique  $\beta$  orientation shared by the largest  $\alpha$  group size, called the unique determination rule.

### 7.3 Automated bcc reconstruction

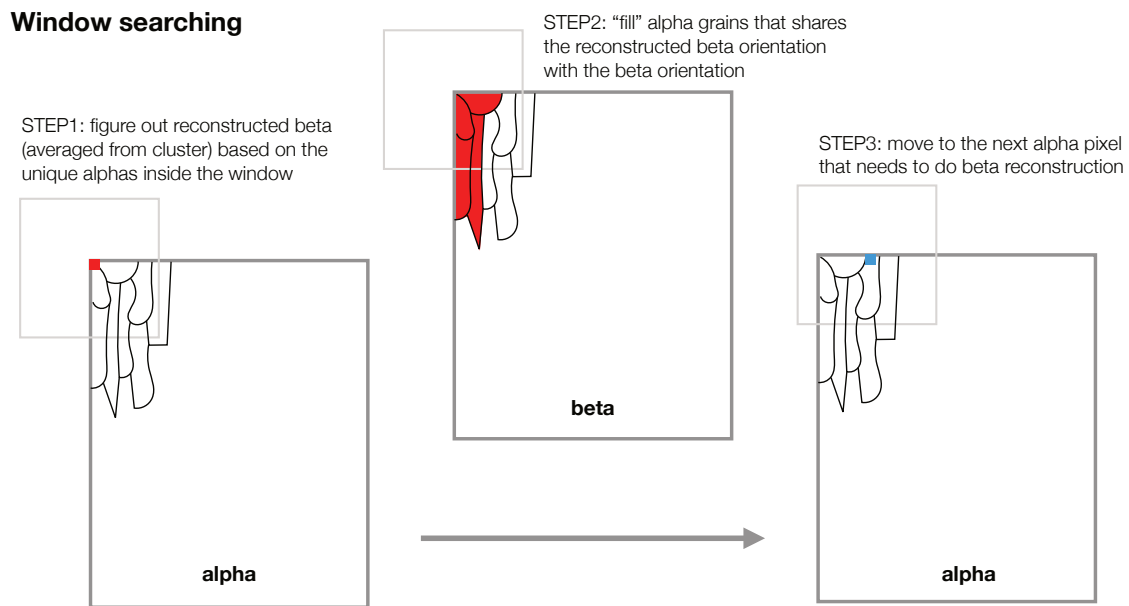


Figure 7.2: Schematic of reconstructing “parent” beta grains by a window searching algorithm.

A window searching algorithm is adopted to do  $\beta$  orientations reconstruction from known  $\alpha$  orientation groups. Figure 7.2 shows an illustration of the algorithm. To minimize the orientation variations in the measurement, averaged orientations of pixels belong to the same  $\alpha$  group (*distinct*) are needed as the first step. The following procedures establish this information:

1. Pixels that belong to the same grain are identified using the floodfill algorithm. Then the average orientation of each grain is calculated.



2. A sort-and-compare algorithm determines distinct  $\alpha$  groups: grains are classified to the same group when the misorientation angle is smaller than  $5^\circ$ . Then average orientation for each  $\alpha$  group is computed.

### 7.3.1 Determining the parent bcc orientation by a cluster-averaging algorithm

A window search approach is used to consider *distinct*  $\alpha$  orientation groups within an area (a square region with the seed pixel being the centroid) comparable to the average grain size of the parent  $\beta$  grains for each examination. The reconstructed  $\beta$  orientation cluster is achieved by three steps (using a case of 5 distinct  $\alpha$  orientations as an example):

1. Calculate six beta orientations for all of the five  $\alpha$  orientations. Then pick one  $\alpha$  as the “seed” and check the misorientation angle between each of the six  $\beta$  orientations of the seed and each  $\beta$  orientation of the other four  $\alpha$  orientations, see Fig. 7.3.

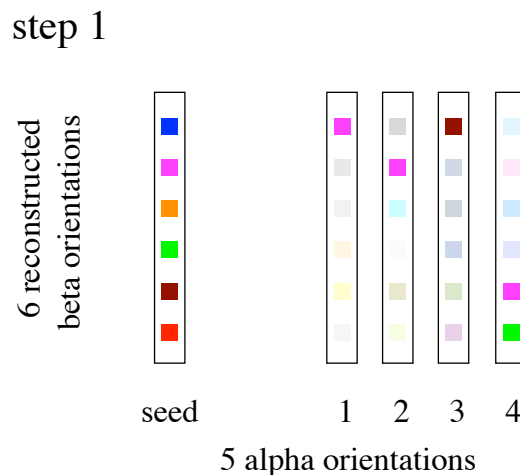


Figure 7.3: The first step: dynamically adding  $\beta$  orientations to the cluster by checking each  $\beta$  orientation of the “seed” against the  $\beta$  orientation of the other  $\alpha$  orientations (columns).

If the misorientation angle is smaller than the tolerance ( $5^\circ$  in this work), add that  $\beta$  orientation to the cluster. Then check the newly added  $\beta$  orientation against the  $\beta$  orientations in each column and repeat the same checking until no new  $\beta$  is added to the cluster. This step

establishes the  $\beta$  orientation clusters/clouds shared by different combinations of distinct  $\alpha$  grains.

- The second step establishes legitimate  $\beta$  clusters by excluding the members violating the unique determination rule. For example, alpha #4 (column 4 in Fig. 7.4) has two identified  $\beta$  orientations (magenta and green  $\beta$  orientation), which is not a uniquely determined situation.

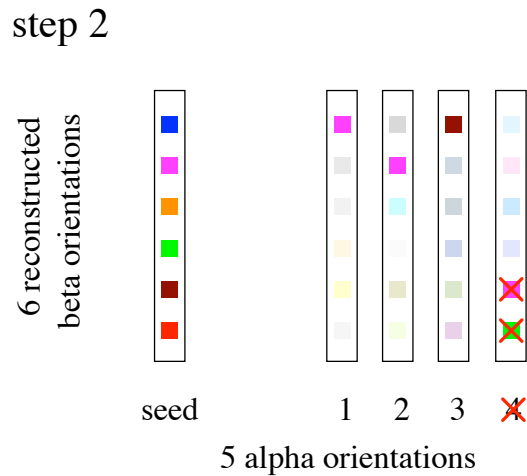


Figure 7.4: The second step excludes the members violating the unique determination rule.

- The third step finds the  $\beta$  cluster shared by the largest number of  $\alpha$  orientations. Figure 7.5 shows that the magenta  $\beta$  cloud is the “longest” shared cluster (shared by the seed, alpha #1, and alpha #2).

Once the longest shared  $\beta$  orientation cluster is established, the average orientation of the cluster is used as the reconstructed  $\beta$  orientation for the grains (within the window) having these  $\alpha$  orientations (seed, alpha #1, and alpha #2). A Python implementation of the cluster-averaging approach can be found in Appendix A.3.

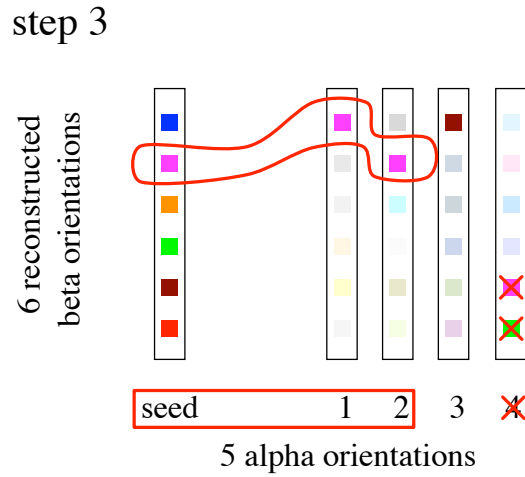


Figure 7.5: The third step finds the longest shared  $\beta$  cluster (magenta).

### 7.3.2 Validation of bcc reconstruction based on synthetic data

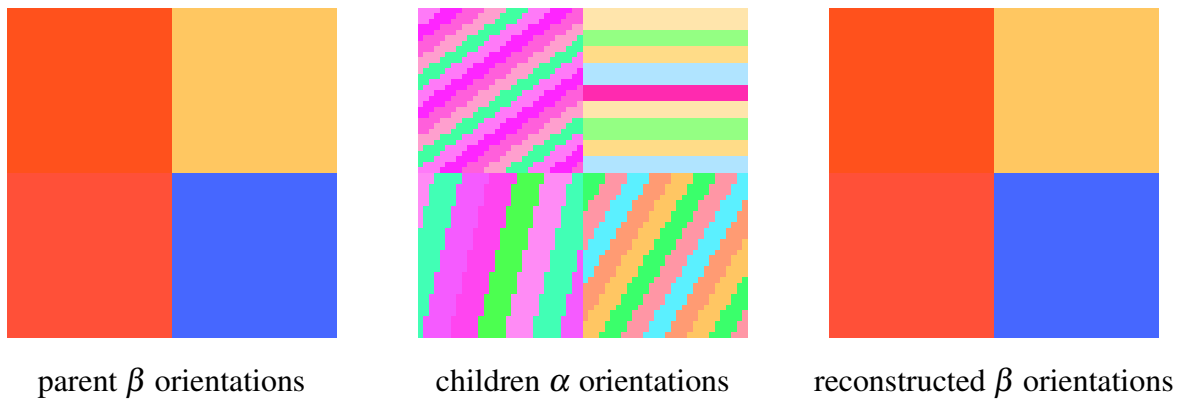


Figure 7.6: Correct  $\beta$  reconstruction results based upon synthetic data.

The above implementation was first tested with synthetic data made with four blocks of random parent  $\beta$  orientations for each, as shown in Fig. 7.6 left. Stripe-shape<sup>1</sup> child  $\alpha$  grains (Fig. 7.6 middle) were then generated to mimic the secondary alpha grains commonly observed in many Ti alloys, such as Ti-6Al-2Sn-4Zr-6Mo (w.t.%) as a result of variant selections. Figure 7.6 right shows the reconstructed orientations for  $\beta$  grains. They are consistent with the *actual* parent  $\beta$  orientations in Fig. 7.6 left.

<sup>1</sup>Note that the reconstruction is based on the distinct hexagonal orientations found within the window. The grain geometry, however, does not directly influence the results.

### 7.3.3 Validation of bcc reconstruction based on measured data

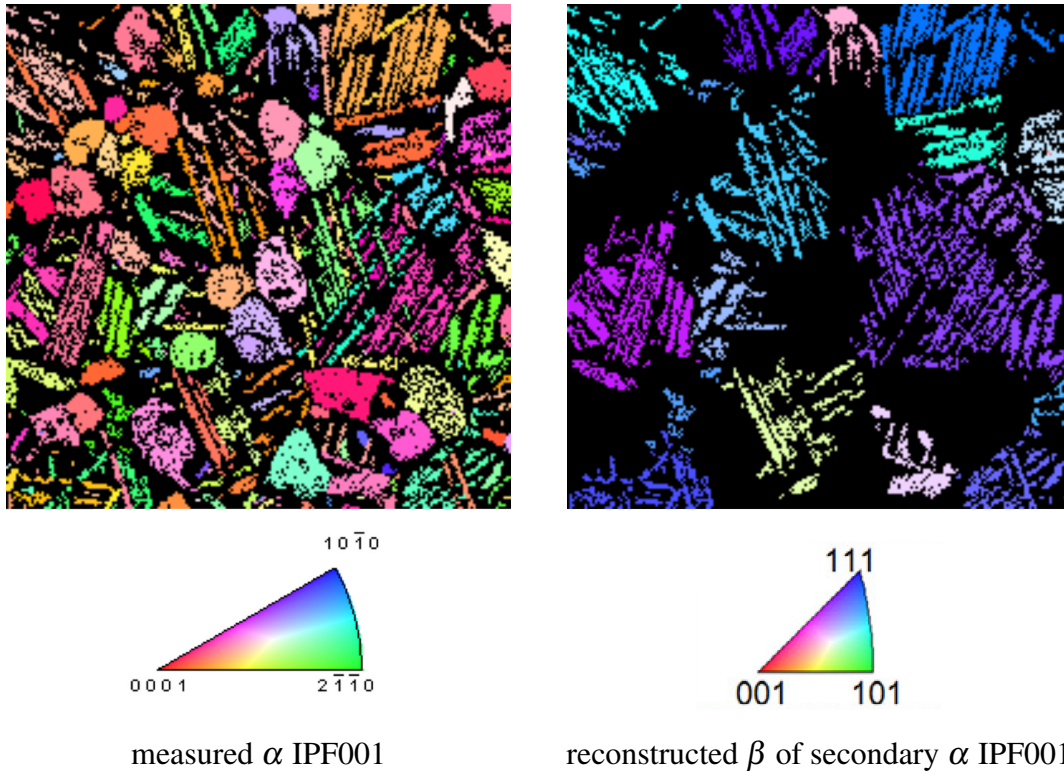


Figure 7.7:  $\beta$  reconstruction ( $200 \times 200$ ) of lamella  $\alpha$  phase in Ti-6Al-2Sn-4Zr-6Mo using window size of 71 ( $\alpha$  data provided by [3]).

A measured orientation map of the  $\alpha$  phase in a Ti-6Al-2Sn-4Zr-6Mo (w.t.%) sample measured by electron backscattered diffraction (EBSD) was used to test the robustness of the automated  $\beta$  reconstruction implementation. The sample has near-equiaxed primary alpha grains and plate-like secondary  $\alpha$  grains that form a *typical* “basket weave” microstructure resulting from variant selections in the  $\beta \rightarrow \alpha$  transformation (left in Fig. 7.7).

The reconstructed  $\beta$  orientations for lamella  $\alpha$  grains are presented in Fig. 7.7 right. The interwoven grains from the same  $\beta$  parent grain show the same orientation color in the reconstruction results.

## 7.4 Summary

A cluster-averaging approach to automate reconstruct  $\beta$  orientations from  $\alpha$  orientations was proposed. It was used to successfully reconstruct  $\beta$  orientation map from lamella microstructure of  $\alpha$  phase in a Ti-6Al-2Sn-4Zr-6Mo sample.

## CHAPTER 8

### CONCLUSIONS AND FUTURE WORK

#### 8.1 Conclusions

Motivated by the common goal that is to improve the prediction of heterogeneous plastic deformation in polycrystalline metallic materials, this thesis presents three projects that aim to establish a reliable approach to obtain constitutive parameters (the first project) and gain understandings of micro-mechanics such as slip interactions with grain boundaries (the second project) and phase transformation kinematics and slip behavior of the transformed microstructure (the third project).

The first project quantifies the uncertainty of *initial* slip resistance or critical resolved shear stress (CRSS) values of hexagonal crystals determined from inverse indentation analysis (IIA), which can be found in Chapter 5. The IIA method generates consistent results when the combined error from experimental measurements and simulation constraints is less than 20 %.

The second project evaluates the effectiveness of several slip transfer metrics and their combinations with artificial neural network (ANN) based on the data obtained from two tensile deformed Al oligocrystals and a tensile deformed polycrystalline Ti-5Al-2.5Sn sample (Chapter 6). This approach extends the one- or two-dimensional projection that was formerly applied to analyze slip transfer data. The maximum classification accuracy reaches around 90 % in the Al study whereas it is about 10 % less for Ti-5Al-2.5Sn. No further insight into the interrelationships among multiple slip transfer metrics is found for both materials as the attainable classification accuracy cannot be noticeably improved with more than two metrics.

The last project proposes a method to calculate orientation and deformation gradient variants in phase transformation between hexagonal  $\alpha$  and body-centered cubic  $\beta$  through a series of frame rotation and transformation. Based on this method, an approach to automate point-wise reconstruction of  $\beta$  orientations from known  $\alpha$  orientations is presented in Chapter 7. The implementation of this approach shows convincing results based upon synthetic data and measured data of a Ti-

6Al-2Sn-4Zr-6Mo sample that exhibits *typical* “basket weave” microstructure as a result of variant selections during the thermo-mechanical treatment.

## 8.2 Future work

Possible future work in these three projects are summarized below:

- IIA can be extended to metals or alloys having a crystal structure whose slip behavior is not well understood. For example, tin (Sn) has a body-centered tetragonal (bct) crystal structure that is more anisotropic than cubic or hexagonal structure.
- The ANN approach can be applied to study slip transfer metrics in other engineering polycrystalline metals or alloys such as Mg and its alloys.
- ANN can be implemented into the existing crystal plasticity models as an intelligent "decision-maker" to determine whether slip transfer happens or not for each individual slip–GB interaction. It would be interesting to compare simulation results of models having the ANN implementation with those using a rigid slip transfer threshold for all slip.
- The method to calculate deformation gradient that describes the kinematics of  $\alpha - \beta$  phase transformation can be included into continuum based models.
- The automated  $\beta$  reconstruction tool can be used to study research problems that need historical information of the current structures, for example, variant selections during the thermo-mechanical treatment of Ti alloys.

## **APPENDIX**



## APPENDIX

### SOFTWARE DEVELOPED AS PART OF THE THESIS

#### **A.1 Scripts for inverse indentation analysis using ABAQUS software**

The scripts to use inverse indentation analysis with ABAQUS software are stored in an open repository at <https://github.com/zhuowenzhao/Optimizer>.

#### **A.2 Python code for slip transfer classification**

The Python code to do artificial neural network analysis of surface observations of slip transfer traces can be accessed at a GitHub repository [https://github.com/zhuowenzhao/ANN\\_feature\\_evaluation](https://github.com/zhuowenzhao/ANN_feature_evaluation).

#### **A.3 Python code for automated $\beta$ phase reconstruction**

The Python implementation for doing automated  $\beta$  phase reconstruction from OIM ang files are kept and updated at <https://github.com/zhuowenzhao/BetaReconstruction>.

## APPENDIX

### SYMMETRY OPERATORS

The 12 hexagonal lattice symmetry operators are listed in Table .1 and the 24 cubic lattice symmetry operators are in Table .2 below in groups of equivalent  $\{110\}$  symmetries.

Table .1: List of 12 hexagonal lattice symmetry operators used in the thesis ( $a = \frac{\sqrt{3}}{2}$ )

$h_1$	$\begin{bmatrix} 1 & 0 & 0 \\ 0 & 1 & 0 \\ 0 & 0 & 1 \end{bmatrix}$	$h_2$	$\begin{bmatrix} -0.5 & a & 0 \\ -a & -0.5 & 0 \\ 0 & 0 & 1 \end{bmatrix}$	$h_3$	$\begin{bmatrix} -0.5 & -a & 0 \\ a & -0.5 & 0 \\ 0 & 0 & 1 \end{bmatrix}$
$h_4$	$\begin{bmatrix} 0.5 & a & 0 \\ -a & 0.5 & 0 \\ 0 & 0 & 1 \end{bmatrix}$	$h_5$	$\begin{bmatrix} -1 & 0 & 0 \\ 0 & -1 & 0 \\ 0 & 0 & 1 \end{bmatrix}$	$h_6$	$\begin{bmatrix} 0.5 & -a & 0 \\ a & 0.5 & 0 \\ 0 & 0 & 1 \end{bmatrix}$
$h_7$	$\begin{bmatrix} -0.5 & -a & 0 \\ -a & 0.5 & 0 \\ 0 & 0 & 1 \end{bmatrix}$	$h_8$	$\begin{bmatrix} -1 & 0 & 0 \\ 0 & -1 & 0 \\ 0 & 0 & 1 \end{bmatrix}$	$h_9$	$\begin{bmatrix} 0.5 & -a & 0 \\ a & 0.5 & 0 \\ 0 & 0 & 1 \end{bmatrix}$
$h_{10}$	$\begin{bmatrix} 0.5 & a & 0 \\ a & -0.5 & 0 \\ 0 & 0 & -1 \end{bmatrix}$	$h_{11}$	$\begin{bmatrix} -1 & 0 & 0 \\ 0 & 1 & 0 \\ 0 & 0 & -1 \end{bmatrix}$	$h_{12}$	$\begin{bmatrix} 0.5 & -a & 0 \\ -a & -0.5 & 0 \\ 0 & 0 & -1 \end{bmatrix}$

Table .2: List of 24 cubic lattice symmetry operators used in the thesis.

---

$\mathbf{b}_1$	$\begin{bmatrix} 1 & 0 & 0 \\ 0 & 1 & 0 \\ 0 & 0 & 1 \end{bmatrix}$	$\mathbf{b}_2$	$\begin{bmatrix} -1 & 0 & 0 \\ 0 & -1 & 0 \\ 0 & 0 & 1 \end{bmatrix}$	$\mathbf{b}_3$	$\begin{bmatrix} 0 & -1 & 0 \\ -1 & 0 & 0 \\ 0 & 0 & -1 \end{bmatrix}$	$\mathbf{b}_4$	$\begin{bmatrix} 0 & 1 & 0 \\ 1 & 1 & 0 \\ 0 & 0 & -1 \end{bmatrix}$	
$\mathbf{b}_5$	$\begin{bmatrix} 1 & 0 & 0 \\ 0 & -1 & 0 \\ 0 & 0 & -1 \end{bmatrix}$	$\mathbf{b}_6$	$\begin{bmatrix} -1 & 0 & 0 \\ 0 & 1 & 0 \\ 0 & 0 & -1 \end{bmatrix}$	$\mathbf{b}_7$	$\begin{bmatrix} 0 & 1 & 0 \\ -1 & 0 & 0 \\ 0 & 0 & 1 \end{bmatrix}$	$\mathbf{b}_8$	$\begin{bmatrix} 0 & -1 & 0 \\ 1 & 0 & 0 \\ 0 & 0 & 1 \end{bmatrix}$	
$\mathbf{b}_9$	$\begin{bmatrix} 0 & 0 & -1 \\ 1 & 0 & 0 \\ 0 & -1 & 0 \end{bmatrix}$	$\mathbf{b}_{10}$	$\begin{bmatrix} 0 & 0 & 1 \\ -1 & 0 & 0 \\ 0 & -1 & 0 \end{bmatrix}$	$\mathbf{b}_{11}$	$\begin{bmatrix} 1 & 0 & 0 \\ 0 & 0 & -1 \\ 0 & 1 & 0 \end{bmatrix}$	$\mathbf{b}_{12}$	$\begin{bmatrix} -1 & 0 & 0 \\ 0 & 0 & 1 \\ 0 & 1 & 0 \end{bmatrix}$	
$\mathbf{b}_{13}$	$\begin{bmatrix} 0 & 0 & -1 \\ -1 & 0 & 0 \\ 0 & 1 & 0 \end{bmatrix}$	$\mathbf{b}_{14}$	$\begin{bmatrix} 0 & 0 & 1 \\ 1 & 0 & 0 \\ 0 & 1 & 0 \end{bmatrix}$	$\mathbf{b}_{15}$	$\begin{bmatrix} -1 & 0 & 0 \\ 0 & 0 & -1 \\ 0 & -1 & 0 \end{bmatrix}$	$\mathbf{b}_{16}$	$\begin{bmatrix} 1 & 0 & 0 \\ 0 & 0 & 1 \\ 0 & -1 & 0 \end{bmatrix}$	
$\mathbf{b}_{17}$	$\begin{bmatrix} 0 & 1 & 0 \\ 0 & 0 & 1 \\ 1 & 0 & 0 \end{bmatrix}$	$\mathbf{b}_{18}$	$\begin{bmatrix} 0 & -1 & 0 \\ 0 & 0 & -1 \\ 1 & 0 & 0 \end{bmatrix}$	$\mathbf{b}_{19}$	$\begin{bmatrix} 0 & 0 & -1 \\ 0 & -1 & 0 \\ -1 & 0 & 0 \end{bmatrix}$	$\mathbf{b}_{20}$	$\begin{bmatrix} 0 & 0 & 1 \\ 0 & 1 & 0 \\ -1 & 0 & 0 \end{bmatrix}$	
$\mathbf{b}_{21}$	$\begin{bmatrix} 0 & 1 & 0 \\ 0 & 0 & -1 \\ -1 & 0 & 0 \end{bmatrix}$	$\mathbf{b}_{22}$	$\begin{bmatrix} 0 & -1 & 0 \\ 0 & 0 & -1 \\ 1 & 0 & 0 \end{bmatrix}$	$\mathbf{b}_{23}$	$\begin{bmatrix} 0 & 0 & 1 \\ 0 & -1 & 0 \\ 1 & 0 & 0 \end{bmatrix}$	$\mathbf{b}_{24}$	$\begin{bmatrix} 0 & 0 & -1 \\ 0 & 1 & 0 \\ 1 & 0 & 0 \end{bmatrix}$	

---

## **BIBLIOGRAPHY**

## BIBLIOGRAPHY

- [1] J. Albiez, H. Erdle, D. Weygand, and T. Böhlke. A gradient plasticity creep model accounting for slip transfer/activation at interfaces evaluated for the intermetallic NiAl-9Mo. *International Journal of Plasticity*, 113:291–311, 2019.
- [2] R. Alizadeh, M. Peña-Ortega, T. R. Bieler, and J. LLorca. A criterion for slip transfer at grain boundaries in Al. *Scripta Materialia*, 178:408–412, 2020.
- [3] Arunima Banerjee. Master’s thesis, Indian Institute of Science, Bangalore, India, 2015.
- [4] F. Barlat, J.C. Brem, J.W. Yoon, K. Chung, R.E. Dick, D.J. Lege, F. Pourboghrat, S.-H. Choi, and E. Chu. Plane stress yield function for aluminum alloy sheetspart 1: theory. *International Journal of Plasticity*, 19(9):1297–1319, 2003.
- [5] Pierre Baudoin, Takayuki Hama, and Hirohiko Takuda. Influence of critical resolved shear stress ratios on the response of a commercially pure titanium oligocrystal: crystal plasticity simulations and experiment. *International Journal of Plasticity*, 115:111–131, 2019.
- [6] E. Bayerschen, A. T. McBride, B. D. Reddy, and T. Böhlke. Review on slip transmission criteria in experiments and crystal plasticity models. *Journal of Materials Science*, 51(5): 2243–2258, 2016.
- [7] T. R. Bieler, P. Eisenlohr, F. Roters, D. Kumar, D. E. Mason, M. A. Crimp, and D. Raabe. The role of heterogeneous deformation on damage nucleation at grain boundaries in single phase metals. *International Journal of Plasticity*, 25(9):1655–1683, 2009.
- [8] T. R. Bieler, P. Eisenlohr, C. Zhang, H. Phukan, and M. A. Crimp. Grain boundaries and interfaces in slip transfer. *Current Opinion in Solid State and Materials Science*, 18:212–226, 2014.
- [9] T. R. Bieler, R. Alizadeh, M. Peña-Ortega, and J. LLorca. An analysis of (the lack of) slip transfer between near-cube oriented grains in pure Al. *International Journal of Plasticity*, 118:269–290, 2019.
- [10] Tom Bieler, R.L. Goetz, and S.L. Semiatin. Anisotropic plasticity and cavity growth during upset forging of Ti6Al4V. *Materials Science and Engineering: A*, 405(1):201–213, 2005.
- [11] Ruth Birch and Thomas Benjamin Britton. Effective structural unit analysis in hexagonal close packed alloys – reconstruction of prior beta microstructures & crystal orientation post processing analysis, 2021.

- [12] J.F.W. Bishop and R. Hill. Xlvi. a theory of the plastic distortion of a polycrystalline aggregate under combined stresses. *The London, Edinburgh, and Dublin Philosophical Magazine and Journal of Science*, 42(327):414–427, 1951.
- [13] C. J. Boehlert, Z. Chen, I. Gutiérrez-Urrutia, J. Llorca, and M. T. Pérez-Prado. In situ analysis of the tensile and tensile-creep deformation mechanisms in rolled AZ31. *Acta Materialia*, 60(4):1889–1904, 2012.
- [14] D. M. Bond and M. A. Zikry. A Predictive Framework for Dislocation-Density Pile-Ups in Crystalline Systems With Coincident Site Lattice and Random Grain Boundaries. *Journal of Engineering Materials and Technology*, 139(2), 2017.
- [15] T. E. Buchheit, J. D. Carroll, B. G. Clark, and B. L. Boyce. Evaluating Deformation-Induced Grain Orientation Change in a Polycrystal During In Situ Tensile Deformation using EBSD. *Microscopy and Microanalysis*, 21(4):969–984, 2015.
- [16] B. Budiansky and T.T. Wu. *Proc. 4th U.S. Nat. Congr. Appl. Mech.*, p.:1175, 1962.
- [17] W.G. Burgers. On the process of transition of the cubic-body-centered modification into the hexagonal-close-packed modification of zirconium. *Physica*, 1(7-12):561–586, 1934.
- [18] C. Cayron, B. Artaud, and L. Briottet. Reconstruction of parent grains from EBSD data. *Materials Characterization*, 57(4):386–401, 2006.
- [19] A. Chakraborty and P. Eisenlohr. Evaluation of an inverse methodology for estimating constitutive parameters in face-centered cubic materials from single crystal indentations. *European Journal of Mechanics / A Solids*, 66C:114–124, 2017.
- [20] A. Chakraborty and P. Eisenlohr. Consistent visualization and uniform sampling of crystallographic directions. Technical report, Michigan State University, 2017.
- [21] Aritra Chakraborty, Chen Zhang, Shanoob Balachandran, Thomas R. Bieler, and Philip Eisenlohr. Assessment of surface and bulk-dominated methodologies to measure critical resolved shear stresses in hexagonal materials. *Acta Materialia*, 184:241–253, 2020.
- [22] Y-W Chen and C-J Lin. *Combining SVMs with Various Feature Selection Strategies*, volume 207, pages 315–324. Springer Berlin Heidelberg, Berlin, Heidelberg, 2006.
- [23] W.A.T. Clark, R.H. Wagoner, Z.Y. Shen, T.C. Lee, I.M. Robertson, and H.K. Birnbaum. On the criteria for slip transmission across interfaces in polycrystals. *Scripta Metallurgica et Materialia*, 26(2):203–206, 1992.
- [24] Martin A. Crimp. Scanning electron microscopy imaging of dislocations in bulk materials,

- using electron channeling contrast. *Microscopy Research and Technique*, 69(5):374–381, 2006.
- [25] Zohra Dahou, Z. Mehdi Sbartaï, Arnaud Castel, and Fouad Ghomari. Artificial neural network model for steelconcrete bond prediction. *Engineering Structures*, 31(8):1724–1733, 2009.
- [26] M.R. Daymond, R.A. Holt, S. Cai, P. Mosbrucker, and S.C. Vogel. Texture inheritance and variant selection through an hcpbcchcp phase transformation. *Acta Materialia*, 58(11):4053–4066, 2010.
- [27] Victor Hugo C. de Albuquerque, Paulo C. Cortez, Auzuir R. de Alexandria, and João Manuel R.S. Tavares. A new solution for automatic microstructures analysis from images based on a backpropagation artificial neural network. *Nondestructive Testing and Evaluation*, 23(4):273–283, 2008.
- [28] F. Delaire, J. L. Raphanel, and C. Rey. Plastic heterogeneities of a copper multocrystal deformed in uniaxial tension: experimental study and finite element simulations. *Acta Materialia*, 48(5):1075–1087, 2000.
- [29] F. Di Gioacchino and J. Quinta da Fonseca. An experimental study of the polycrystalline plasticity of austenitic stainless steel. *International Journal of Plasticity*, 74:92–109, 2015.
- [30] I. Doghri, L. Adam, and N. Bilger. Mean-field homogenization of elasto-viscoplastic composites based on a general incrementally affine linearization method. *International Journal of Plasticity*, 26(2):219–238, 2010.
- [31] R. Eberhart and J. Kennedy. A new optimizer using particle swarm theory. In *Proceedings of the Sixth International Symposium on Micro Machine and Human Science*, pages 39–43, 1995.
- [32] Russel Eberhart and Yuhui Shi. Particle swarm optimization: developments, applications and resources. In *Proceedings of the 2001 Congress on Evolutionary Computation (IEEE Cat. No. 01TH8546)*, volume 1, pages 81–86, 2001.
- [33] Chelsea M. Edge. Analysis of slip transfer in TI-5Al-2.5Sn (wt. %) at two temperatures in comparison to pure aluminum. Master’s thesis, Michigan State University, East Lansing, Michigan, USA, 2020.
- [34] J.D. Eshelby, F.C. Frank, and F.R.N. Nabarro. Xli. the equilibrium of linear arrays of dislocations. *The London, Edinburgh, and Dublin Philosophical Magazine and Journal of Science*, 42(327):351–364, 1951.

- [35] A. Fallahi, D. E. Mason, D. Kumar, T. R. Bieler, and M. A. Crimp. The effect of grain boundary normal on predicting microcrack nucleation using fracture initiation parameters in duplex TiAl. *Materials Science and Engineering A*, 432(1-2):281–291, 2006.
- [36] A.A. Fedorov, M.Yu. Gutkin, and I.A. Ovidko. Transformations of grain boundary dislocation pile-ups in nano- and polycrystalline materials. *Acta Materialia*, 51(4):887–898, 2003.
- [37] S. Feng, H. Zhou, and H. Dong. Using deep neural network with small dataset to predict material defects. *Materials & Design*, 162:300–310, 2019.
- [38] T Furuhashi and T Maki. Variant selection in heterogeneous nucleation on defects in diffusional phase transformation and precipitation. *Materials Science and Engineering: A*, 312(1-2):145–154, aug 2001.
- [39] A.F. Gerday, M. Ben Bettaieb, L. Duchêne, N. Clement, H. Diarra, and A.M. Habraken. Material behavior of the hexagonal alpha phase of a titanium alloy identified from nanoindentation tests. *European Journal of Mechanics - A/Solids*, 30(3):248–255, 2011.
- [40] N. Gey and M. Humbert. Characterization of the variant selection occurring during the  $\alpha \rightarrow \beta \rightarrow \alpha$  phase transformations of a cold rolled titanium sheet. *Acta Materialia*, 50(2): 277–287, jan 2002.
- [41] N. Gey, E. Gautier, M. Humbert, A. Cerqueira, J.L. Bechade, and P. Archambault. Study of the  $\alpha/\beta$  phase transformation of Zy-4 in presence of applied stresses at heating: analysis of the inherited microstructures and textures. *Journal of Nuclear Materials*, 302(2-3):175–184, apr 2002.
- [42] M.G. Glavicic, P.A. Kobryn, T.R. Bieler, and S.L. Semiatin. A method to determine the orientation of the high-temperature beta phase from measured EBSD data for the low-temperature alpha phase in Ti-6Al-4V. *Materials Science and Engineering: A*, 346(1): 50–59, 2003.
- [43] J.W Glen and S.F Pugh. The effect of phase transformations on the orientation of zirconium crystals. *Acta Metallurgica*, 2(3):520–529, 1954.
- [44] Jicheng Gong, T. Benjamin Britton, Mitchell A. Cuddihy, Fionn P.E. Dunne, and Angus J. Wilkinson.  $\langle a \rangle$  Prismatic,  $\langle a \rangle$  basal, and  $\langle c+a \rangle$  slip strengths of commercially pure Zr by micro-cantilever tests. *Acta Materialia*, 96:249–257, 2015. ISSN 1359-6454.
- [45] D. Gonzalez, I. Simonovski, P. J. Withers, and J. Quinta da Fonseca. Modelling the effect of elastic and plastic anisotropies on stresses at grain boundaries. *International Journal of Plasticity*, 61:49–63, 2014.



- [46] A. Guery, F. Hild, F. Latourte, and S. Roux. Slip activities in polycrystals determined by coupling DIC measurements with crystal plasticity calculations. *International Journal of Plasticity*, 2016.
- [47] Y. Guo, T.B. Britton, and A.J. Wilkinson. Slip bandgrain boundary interactions in commercial-purity titanium. *Acta Materialia*, 76:1–12, 2014.
- [48] Z Guo and W Sha. Modelling the correlation between processing parameters and properties of maraging steels using artificial neural network. *Computational Materials Science*, 29(1): 12–28, 2004.
- [49] Shreyash Hadke, Manendra Singh Parihar, Satish Shekhawat, and Rajesh Kisni Khatirkar. A new method for automated reconstruction of pre-transformation microstructures. *Philosophical Magazine Letters*, 96(5):175–182, 2016.
- [50] E O Hall. The deformation and ageing of mild steel: III discussion of results. *Proceedings of the Physical Society. Section B*, 64(9):747–753, sep 1951.
- [51] Takayuki Hama, Akihiro Kobuki, and Hirohiko Takuda. Crystal-plasticity finite-element analysis of anisotropic deformation behavior in a commercially pure titanium grade 1 sheet. *International Journal of Plasticity*, 91:77–108, 2017.
- [52] Songyang Han, Philip Eisenlohr, and Martin A. Crimp. ECCI based characterization of dislocation shear in polycrystalline arrays during heterogeneous deformation of commercially pure titanium. *Materials Characterization*, 142:504–514, 2018.
- [53] S. Haouala, R. Alizadeh, T. R. Bieler, J. Segurado, and J. LLorca. Effect of slip transmission at grain boundaries in Al bicrystals. *International Journal of Plasticity*, 126:102600–, 2020.
- [54] S.V. Harren. The finite deformation of rate-dependent polycrystals—I. A self-consistent framework. *Journal of the Mechanics and Physics of Solids*, 39(3):345–360, 1991.
- [55] D. He, J.C. Zhu, S. Zaefferer, D. Raabe, Y. Liu, Z.L. Lai, and X.W. Yang. Influences of deformation strain, strain rate and cooling rate on the burgers orientation relationship and variants morphology during phase transformation in a near titanium alloy. *Materials Science and Engineering: A*, 549:20–29, 2012.
- [56] S. Hémerly, P. Nizou, and P. Villechaise. In situ SEM investigation of slip transfer in Ti-6Al-4V: Effect of applied stress. *Materials Science and Engineering: A*, 709:277–284, 2018.
- [57] R. Hill. A self-consistent mechanics of composite materials. *Journal of the Mechanics and Physics of Solids*, 13(4):213–222, 1965.

- [58] D. Hull and D. J. Bacon. *Introduction to Dislocations*. Butterworth-Heinemann, 5 edition, 2011.
- [59] M. Humbert, F. Wagner, H. Moustahfid, and C. Esling. Determination of the orientation of a parent  $\beta$  grain from the orientations of the inherited  $\alpha$  plates in the phase transformation from body-centred cubic to hexagonal close packed. *Journal of Applied Crystallography*, 28(5):571–576, Oct 1995.
- [60] J. W. Hutchinson. Elastic-plastic behaviour of polycrystalline metals and composites. *Proc. R. Soc. Lond.*, A(319):247–272, 1970.
- [61] S. Hémerly, A. Nait-Ali, and P. Villechaise. Combination of in-situ SEM tensile test and FFT-based crystal elasticity simulations of Ti-6Al-4V for an improved description of the onset of plastic slip. *Mechanics of Materials*, 109:1–10, 2017.
- [62] J. Kacher, B. P. Eftink, B. Cui, and I. M. Robertson. Dislocation interactions with grain boundaries. *Current Opinion in Solid State and Materials Science*, 18(4):227–243, 2014.
- [63] T. Karthikeyan, S. Saroja, and M. Vijayalakshmi. Evaluation of misorientation angle-axis set between variants during transformation of bcc to hcp phase obeying Burgers orientation relation. *Scripta Materialia*, 55(9):771–774, nov 2006.
- [64] J. Kennedy and R. Eberhart. Particle swarm optimization. In *Proceedings of IEEE International Conference on Neural Networks IV*, pages 1942–1948, 1995. doi: 10.1109/ICNN.1995.488968.
- [65] K.V. Mani Krishna, P. Tripathi, V.D. Hiwarkar, P. Pant, I. Samajdar, D. Srivastava, and G.K. Dey. Automated reconstruction of pre-transformation microstructures in zirconium. *Scripta Materialia*, 62(6):391–394, 2010.
- [66] E Kröner. Zur plastischen verformung des vielkristalls. *Acta Metallurgica*, 9(2):155–161, 1961.
- [67] C. Lall, S. Chin, and D.P. Pope. The orientation and temperature dependence of the yield stress of  $Ni_3$  (Al, Nb) single crystals. *Metall Mater Trans A*, 10:1323–1332, 1979.
- [68] Baptiste Larrouy, Patrick Villechaise, Jonathan Cormier, and Olivier Berteaux. Grain boundary slip bands interactions: Impact on the fatigue crack initiation in a polycrystalline forged Ni-based superalloy. *Acta Materialia*, 99:325–336, 2015.
- [69] R.A. Lebensohn and C.N. Tomé. A self-consistent anisotropic approach for the simulation of plastic deformation and texture development of polycrystals: Application to zirconium alloys. *Acta Metallurgica et Materialia*, 41(9):2611–2624, 1993.

- [70] Y. LeCun, Y. Bengio, and G. Hinton. Deep learning. *Nature*, 521(7553):436–444, 2015.
- [71] E. H. Lee. Elastic-plastic deformation at finite strains. *Journal of Applied Mechanics*, 36(1):1–6, 03 1969.
- [72] T. C. Lee, I. M. Robertson, and H. K. Birnbaum. Prediction of slip transfer mechanisms across grain boundaries. *Scripta Metallurgica*, 23(5):799–803, 1989.
- [73] T. C. Lee, I. M. Robertson, and H. K. Birnbaum. TEM in situ deformation study of the interaction of lattice dislocations with grain boundaries in metals. *Philosophical Magazine A*, 62(1):131–153, 1990.
- [74] H. Li, D.E. Mason, T.R. Bieler, C.J. Boehlert, and M.A. Crimp. Methodology for estimating the critical resolved shear stress ratios of  $\alpha$ -phase Ti using EBSD-based trace analysis. *Acta Materialia*, 61(20):7555–7567, 2013.
- [75] H. Li, D.E. Mason, Y. Yang, T.R. Bieler, M.A. Crimp, and C.J. Boehlert. Comparison of the deformation behaviour of commercially pure titanium and Ti5Al2.5Sn(wt.%) at 296 and 728 K. *Philosophical Magazine*, 93(21):2875–2895, 2013.
- [76] H. Lim, L. M. Hale, J. A. Zimmerman, C. C. Battaile, and C. R. Weinberger. A multi-scale model of dislocation plasticity in  $\alpha$ -Fe: Incorporating temperature, strain rate and non-Schmid effects. *International Journal of Plasticity*, 73:100–118, 2015.
- [77] H. Lim, R. Dingreville, L. A. Deibler, T. E. Buchheit, and C. C. Battaile. Investigation of grain-scale microstructural variability in tantalum using crystal plasticity-finite element simulations. *Computational Materials Science*, 117:437–444, 2016.
- [78] M. A. Linne, A. Venkataraman, M. D. Sangid, and S. Daly. Grain boundary sliding and slip transmission in high purity aluminum. *Experimental Mechanics*, 59(5):643–658, 2019.
- [79] Marissa A. Linne, Thomas R. Bieler, and Samantha Daly. The effect of microstructure on the relationship between grain boundary sliding and slip transmission in high purity aluminum. *International Journal of Plasticity*, 135:102818, 2020.
- [80] J.D Livingston and B Chalmers. Multiple slip in bicrystal deformation. *Acta Metallurgica*, 5(6):322–327, 1957.
- [81] I. Lonardelli, N. Gey, H.-R. Wenk, M. Humbert, S.C. Vogel, and L. Lutterotti. In situ observation of texture evolution during and phase transformations in titanium alloys investigated by neutron diffraction. *Acta Materialia*, 55(17):5718–5727, 2007.
- [82] J. Luster and J. M. Morris. Compatibility of deformation in two-phase Ti-Al alloys: Depen-

- dence on microstructure and orientation relationships. *Metallurgical and Materials Transactions A*, 26(7):1745–1756, 1995.
- [83] Gerd Lütjering and James C Williams. *Titanium*, chapter Fundamental Aspects, pages 15–52. Springer Berlin Heidelberg, Berlin, Heidelberg, 2007.
- [84] A. Ma, F. Roters, and D. Raabe. On the consideration of interactions between dislocations and grain boundaries in crystal plasticity finite element modeling – Theory, experiments, and simulations. *Acta Materialia*, 54(8):2181–2194, 2006.
- [85] N. V. Malyar, J. S. Micha, G. Dehm, and C. Kirchlechner. Size effect in bi-crystalline micropillars with a penetrable high angle grain boundary. *Acta Materialia*, 129:312–320, 2017.
- [86] H. Mansour, J. Guyon, M.A. Crimp, N. Gey, B. Beausir, and N. Maloufi. Accurate electron channeling contrast analysis of dislocations in fine grained bulk materials. *Scripta Materialia*, 84-85:11–14, 2014.
- [87] S. Mercier and A. Molinari. Homogenization of elastic-viscoplastic heterogeneous materials: Self-consistent and Mori-Tanaka schemes. *International Journal of Plasticity*, 25(6): 1024–1048, 2009.
- [88] S. Miyazaki, K. Otsuka, and C.M. Wayman. The shape memory mechanism associated with the martensitic transformation in TiNi alloys—I. Self-accommodation. *Acta Metallurgica*, 37(7):1873–1884, 1989.
- [89] T Mori and K Tanaka. Average stress in matrix and average elastic energy of materials with misfitting inclusions. *Acta Metallurgica*, 21(5):571–574, 1973.
- [90] P. Morin, M. Pitaval, D. Besnard, and G. Fontaine. Electronchannelling imaging in scanning electron microscopy. *Philosophical Magazine A*, 40(4):511–524, 1979.
- [91] J. A. Nelder and R. Mead. A simplex method for function minimization. *The Computer Journal*, 7(4):308–313, 01 1965.
- [92] S. Nemat-Nasser and M. Obata. Rate-dependent, finite elasto-plastic deformation of polycrystals. *Proc. R. Soc. Lond.*, A(407):343–375, 1986.
- [93] V. I. Nikolaichick and I. I. Khodos. A review of the determination of dislocation parameters using strong- and weak-beam electron microscopy. *Journal of Microscopy*, 155(2):123–167, 1989.
- [94] T. Nyyssönen, P. Peura, and VT. Kuokkala. Crystallography, morphology, and martensite

- transformation of prior austenite in intercritically annealed high-aluminum steel. *Metallurgical and Materials Transactions A*, 49:6426?6441, 2018.
- [95] G.C. Obasi, S. Biroasca, J. Quinta da Fonseca, and M. Preuss. Effect of  $\beta$  grain growth on variant selection and texture memory effect during  $\alpha \rightarrow \beta \rightarrow \alpha$  phase transformation in Ti-6Al-4V. *Acta Materialia*, 60(3):1048–1058, feb 2012.
- [96] W.C. Oliver and G.M Pharr. An improved technique for determining hardness and elastic modulus using load and displacement sensing indentation experiments. *Journal of Materials Research*, 7:1564–1583, 1992.
- [97] S. Pathak and S. R. Kalidindi. Spherical nanoindentation stress–strain curves. *Materials Science and Engineering: R: Reports*, 91:1–36, 2015.
- [98] D. Peirce, R.J. Asaro, and A. Needleman. Material rate dependence and localized deformation in crystalline solids. *Acta Metallurgica*, 31(12):1951–1976, 1983.
- [99] N. J. Petch. The cleavage strength of polycrystals. *J. Iron Steel Inst.*, 174:25–28, 1953.
- [100] Adam L. Pilchak and Thomas F. Broderick. Evidence of a Massive Transformation in a Ti-6Al-4V Solid-State Weld? *JOM*, 65(5):636–642, mar 2013.
- [101] E. Plancher, P. Tajdary, T. Auger, O. Castelnau, V. Favier, D. Loisonard, J-B Marijon, C. Maurice, V. Michel, O. Robach, and J. Stodolna. Validity of Crystal Plasticity Models Near Grain Boundaries: Contribution of Elastic Strain Measurements at Micron Scale. *JOM*, 71(10): 3543–3551, 2019.
- [102] M. Puri, A. Solanki, T. Padawer, S. M. Tipparaju, W. A. Moreno, and Y. Pathak. *Introduction to artificial neural network (ANN) as a predictive tool for drug design, discovery, delivery, and disposition*, pages 3–13. Elsevier, 2016.
- [103] Dierk Raabe, Zisu Zhao, and Franz Roters. A finite element method on the basis of texture components for fast predictions of anisotropic forming operations. *Steel Research*, 72(10): 421–426, 2001.
- [104] J. Romero, M. Preuss, and J. Quinta da Fonseca. Texture memory and variant selection during phase transformation of a zirconium alloy. *Acta Materialia*, 57(18):5501–5511, 2009.
- [105] F. Roters, P. Eisenlohr, L. Hantcherli, D. D. Tjahjanto, T. R. Bieler, and D. Raabe. Overview of constitutive laws, kinematics, homogenization, and multiscale methods in crystal plasticity finite element modeling: Theory, experiments, applications. *Acta Materialia*, 58: 1152–1211, 2010.

- [106] F. Roters, M. Diehl, P. Shanthraj, P. Eisenlohr, C. Reuber, S. L. Wong, T. Maiti, A. Ebrahimi, T. Hochrainer, H-O Fabritius, S. Nikolov, M. Friak, N. Fujita, N. Grilli, K. G. F. Janssens, N. Jia, P. J. J. Kok, D. Ma, F. Meier, E. Werner, M. Stricker, D. Weygand, and D. Raabe. DAMASK – The Düsseldorf Advanced Material Simulation Kit for Modelling Multi-Physics Crystal Plasticity, Damage, and Thermal Phenomena from the Single Crystal up to the Component Scale. *Computational Materials Science*, 158:420–478, 2019.
- [107] Franz Roters, Philip Eisenlohr, Thomas R. Bieler, and Dierk Raabe. *Crystal Plasticity Finite Element Methods in Materials Science and Engineering*. Wiley-VCH, 2010.
- [108] M. D. Sangid, H. J. Maier, and H. Sehitoglu. The role of grain boundaries on fatigue crack initiation – An energy approach. *International Journal of Plasticity*, 27(5):801–821, 2011.
- [109] J. Schmidhuber. Deep learning in neural networks: an overview. *Neural Netw*, 61:85–117, 2015.
- [110] J. R. Seal, M. A. Crimp, T. R. Bieler, and C. J. Boehlert. Analysis of slip transfer and deformation behavior across the  $\alpha/\beta$  interface in Ti–5Al–2.5Sn (wt.%) with an equiaxed microstructure. *Materials Science and Engineering A*, 552:61–68, 2012.
- [111] G.G.E. Seward, S. Celotto, D.J. Prior, J. Wheeler, and R.C. Pond. In situ SEM-EBSD observations of the hcp to bcc phase transformation in commercially pure titanium. *Acta Materialia*, 52(4):821–832, feb 2004.
- [112] Z. Shen, R.H. Wagoner, and W.A.T. Clark. Dislocation and grain boundary interactions in metals. *Acta Metallurgica*, 36(12):3231–3242, 1988.
- [113] B.A Simkin and M.A Crimp. An experimentally convenient configuration for electron channeling contrast imaging. *Ultramicroscopy*, 77(1):65–75, 1999.
- [114] J. C. H. Spencer, H. R. Kolar, G. Hembree, C. J. Humphreys, J. Barnard, R. Datta, C. Koch, F. M. Ross, and J. F. Justo. Imaging dislocation cores the way forward. *Philosophical Magazine*, 86(29-31):4781–4796, 2006.
- [115] J.C. Stinville, N. Vanderesse, F. Bridier, P. Bocher, and T.M. Pollock. High resolution mapping of strain localization near twin boundaries in a nickel-based superalloy. *Acta Materialia*, 98:29–42, 2015.
- [116] Y. Su, C. Zambaldi, D. Mercier, P. Eisenlohr, T.R. Bieler, and M.A. Crimp. Quantifying deformation processes near grain boundaries in titanium using nanoindentation and crystal plasticity modeling. *International Journal of Plasticity*, 86:170–186, 2016.
- [117] Yang Su, Songyang Han, Philip Eisenlohr, and Martin Crimp. Predicting shear transmission

- across grain boundaries with an iterative stress relief model. *Acta Materialia*, 215:116992, 2021.
- [118] R. Sánchez-Martín, M.T. Pérez-Prado, J. Segurado, J. Bohlen, I. Gutiérrez-Urrutia, J. Llorca, and J.M. Molina-Aldareguia. Measuring the critical resolved shear stresses in Mg alloys by instrumented nanoindentation. *Acta Materialia*, 71:283–292, 2014.
- [119] V. Tari, A. D. Rollett, and H. Beladi. Back calculation of parent austenite orientation using a clustering approach. *Journal of Applied Crystallography*, 46(1):210–215, Feb 2013.
- [120] M. A. Tschopp and D. L. McDowell. Asymmetric tilt grain boundary structure and energy in copper and aluminium. *Philosophical Magazine*, 87(25):3871–3892, 2007.
- [121] M.A. Tschopp and D.L. McDowell. Dislocation nucleation in 3 asymmetric tilt grain boundaries. *International Journal of Plasticity*, 24(2):191–217, 2008.
- [122] R. von Mises. Mechanik der festen körper im plastisch deformablen zustand. *Göttin. Nachr. Math. Phys.*, 1:582–592, 1913.
- [123] J.-Y. Wang, N. Li, R. Alizadeh, M.A. Monclús, Y.W. Cui, J.M. Molina-Aldareguía, and J. Llorca. Effect of solute content and temperature on the deformation mechanisms and critical resolved shear stress in Mg-Al and Mg-Zn alloys. *Acta Materialia*, 170:155–165, 2019.
- [124] L. Wang, Z. Zheng, H. Phukan, P. Kenesei, J.-S. Park, J. Lind, R.M. Suter, and T.R. Bieler. Direct measurement of critical resolved shear stress of prismatic and basal slip in polycrystalline Ti using high energy X-ray diffraction microscopy. *Acta Materialia*, 132:598–610, 2017.
- [125] Leyun Wang, Zhonghe Huang, Huamiao Wang, Alireza Maldar, Sangbong Yi, Jun-Sang Park, Peter Kenesei, Erica Lilleodden, and Xiaoqin Zeng. Study of slip activity in a Mg-Y alloy by in situ high energy X-ray diffraction microscopy and elastic viscoplastic self-consistent modeling. *Acta Materialia*, 155:138–152, 2018.
- [126] S.C. Wang, M. Aindow, and M.J. Starink. Effect of self-accommodation on  $\alpha/\alpha$  boundary populations in pure titanium. *Acta Materialia*, 51(9):2485–2503, may 2003.
- [127] Zigan Wei, Ping Yang, Xinfu Gu, Yusuke Onuki, and Shigeo Sato. Transformation textures in pure titanium: Texture memory vs surface effect. *Materials Characterization*, 164: 110359, 2020.
- [128] E. Werner and W. Prantl. Slip transfer across grain and phase boundaries. *Acta Metallurgica et Materialia*, 38(3):533–537, 1990.

- [129] Ewald Werner and Hein Peter Stüwe. Phase boundaries as obstacle to dislocations motion. *Materials Science and Engineering*, 68(2):175–182, 1985.
- [130] E.A. West and G.S. Was. Strain incompatibilities and their role in intergranular cracking of irradiated 316l stainless steel. *Journal of Nuclear Materials*, 441(1):623–632, 2013.
- [131] H. White. Learning in Artificial Neural Networks: A Statistical Perspective. *Neural Computation*, 1(4):425–464, 1989.
- [132] P Yang, Z G Wei, X F Gu, F E Cui, and W M Mao. Influences of cold rolling, recrystallization and surface effect on the transformation textures in a TA10 titanium alloy. *Journal of Physics: Conference Series*, 1270:012037, aug 2019.
- [133] Stefan Zaefferer and Nahid-Nora Elhami. Theory and application of electron channelling contrast imaging under controlled diffraction conditions. *Acta Materialia*, 75:20–50, 2014.
- [134] Alexander Zaitzeff, Adam Pilchak, Tracy Berman, John Allison, and Selim Esedoglu. A robust algorithm to calculate parent  $\beta$  grain shapes and orientations from  $\alpha$  phase electron backscatter diffraction data in  $\alpha/\beta$ -titanium alloys. *Scripta Materialia*, 191:191–195, 2021.
- [135] C. Zambaldi and D. Raabe. Plastic anisotropy of  $\gamma$ -TiAl revealed by axisymmetric indentation. *Acta Materialia*, 58(9):3516–3530, 2010.
- [136] C. Zambaldi, Y. Yang, T. R. Bieler, and D. Raabe. Orientation informed nanoindentation of  $\alpha$ -titanium: Indentation pileup in hexagonal metals deforming by prismatic slip. *Journal of Materials Research*, 27(1):356–367, 2012.
- [137] L. Zeng and T. R. Bieler. Effects of working, heat treatment, and aging on microstructural evolution and crystallographic texture of  $\alpha$ ,  $\alpha'$ ,  $\alpha''$  and  $\beta$  phases in Ti–6Al–4V wire. *Materials Science and Engineering: A*, 392(1-2):403–414, 2005.
- [138] C. Zhang, H. Li, P. Eisenlohr, W. Liu, C.J. Boehlert, M.A. Crimp, and T.R. Bieler. Effect of realistic 3D microstructure in crystal plasticity finite element analysis of polycrystalline Ti-5Al-2.5Sn. *International Journal of Plasticity*, 69:21–35, 2015.
- [139] Z.B. Zhao, Q.J. Wang, Q.M. Hu, J.R. Liu, B.B. Yu, and R. Yang. Effect of  $\beta$  (110) texture intensity on  $\alpha$ -variant selection and microstructure morphology during  $\beta \rightarrow \alpha$  phase transformation in near  $\alpha$  titanium alloy. *Acta Materialia*, 126:372–382, mar 2017.
- [140] Zhuowen Zhao, Thomas R. Bieler, Javier LLorca, and Philip Eisenlohr. Grain boundary slip transfer classification and metric selection with artificial neural networks. *Scripta Materialia*, 185:71–75, 2020.